

Finite element thermal analysis towards microstructure improvement in directed energy deposition of high speed steel

A thesis submitted in partial fulfillment of the requirements
for the degree of Doctor of Philosophy (PhD) in Engineering Science

by

Rúben António TOMÉ JARDIN



Supervisor: Anne Marie HABRAKEN

Co-supervisor: Anne MERTENS

Jury Members

Prof. Anne Marie Habraken(Supervisor)
Prof. Anne Mertens (Co-supervisor)
Prof. Laurent Duchêne
Prof. Romain Boman
Dr. Jérôme Tchuindjang

University of Liège, Belgium
University of Liège, Belgium
University of Liège, Belgium
University of Liège, Belgium
University of Liège, Belgium

Associate Prof. Víctor Tuninetti

Universidad de La Frontera;
Department of Mechanical Engineering
Candelaria 0271
Temuco, Araucania,
Chile
Tel +56 9 5302 3958
victor.tuninetti@ufrontera.cl

Prof. Muriel Carin

Université Bretagne Sud, France
Institut de Recherche Dupuy de Lôme - UMR
CNRS 6027
Centre de Recherche C. Huygens
Rue de Saint Maudé - BP 92116
F-56321 LORIENT Cedex
France
tél. +33 (0)2 97 87 45 51
muriel.carin@univ-ubs.fr

Abstract

This joint PhD thesis between MSM (Mechanics of Solids and Materials) and MMS (Metallic Materials Science) teams, presents an in-depth investigation into the Directed Energy Deposition process of High-Speed Steel M4. Through a blend of computational modeling (MSM) and experimental work (MMS), this research explores the complex interrelations between process parameters, thermal history, and the resultant microstructural and mechanical properties of DED parts fabricated in High Speed Steel HSS M4. This study was supported by a FNRS PDR Project “Lasercladding” and additional funding from an ULiege Faculty grant, alongside collaborative efforts with SIRRIS.

The thesis begins by establishing a foundational understanding of the DED process, exploring its potential defects, and underscoring the necessity of a modeling tool capable of optimizing parameters to mitigate these defects. Chapter 2 introduces a 2D thermal model, developed to comprehend the thermal dynamics within a 36-layer bulk deposit of HSS M4. This model, validated against measured thermal histories and melt pool sizes, presents out the basis for a study into thermal effects on microstructure.

Progressing to Chapter 3, the research transitions to a 3D thermomechanical model, confronting the challenges posed by deviations in measured thermophysical properties from those traditionally reported for cast or forged samples. A series of compression tests across various temperatures and strain rates further enriches the understanding of the stress-strain behavior of M4 HSS, laying the groundwork for subsequent analyses.

In Chapter 4, the research focuses on the optimization of the DED process, specifically through the implementation of a variable laser power strategy aimed at achieving uniform microstructures at different deposit depths. The relationship between melt pool size, remelting events, and microstructure is examined, employing the Newton-Raphson iterative method to fine-tune the laser power function for optimal melt pool dimensions. This approach is validated by real experiments, which demonstrate the possibility of obtaining homogeneity of the microstructure in the properties of materials throughout the depth of the sample.

The thesis concludes with an evaluation of the mechanical properties of the optimized samples, utilizing microhardness and nanoindentation tests. These assessments reveal significant improvements in homogeneity, attributable to the refined thermal management and microstructure optimization strategies developed through this research.

This work focuses on the DED process and its impact on HSS M4. It highlights the critical role of accurate thermal and mechanical modeling in advancing AM technologies. The insights and methodologies developed here offer support for ongoing work in both research teams, providing a foundation for further exploration and innovation in metal additive manufacturing.

Résumé

Cette thèse de doctorat conjointe entre les équipes MSM (Mécanique des Solides et Matériaux) et MMS (Sciences des Matériaux Métallique) présente une investigation approfondie du processus de Dépôt d'Énergie Dirigée sur l'Acier Rapide M4. À travers un mélange de modélisations computationnelles (MSM) et de travaux expérimentaux (MMS), cette recherche explore les interrelations complexes entre les paramètres de, l'histoire thermique, et les propriétés microstructurales et mécaniques résultantes de l'HSS M4 fabriqué par DED. Cette étude a été soutenue par le projet FNRS PDR Lasercladding et un financement supplémentaire d'une bourse de la Faculté de l'ULiège, en collaboration avec SIRRIIS.

La thèse commence par établir une compréhension fondamentale du processus DED, explorant ses défauts potentiels, et soulignant la nécessité d'un outil de modélisation capable d'optimiser les paramètres pour atténuer ces défauts. Le Chapitre 2 introduit un modèle thermique 2D, développé pour comprendre la dynamique thermique au sein d'un dépôt en bloc de 36 couches d'HSS M4. Ce modèle, validé contre des historiques thermiques mesurés et des tailles de bassin de fusion, présente les bases pour une étude des effets thermiques sur la microstructure.

Progressant vers le Chapitre 3, la recherche passe à un modèle thermomécanique 3D, confrontant les défis posés par les écarts dans les propriétés thermophysiques mesurées par rapport à celles traditionnellement rapportées pour les échantillons coulés ou forgés. Une série de tests de compression à différentes températures et vitesses de déformation enrichit davantage la compréhension du comportement contrainte-déformation de l'HSS M4, jetant les bases pour des analyses subséquentes.

Dans le Chapitre 4, la recherche se concentre sur l'optimisation du procédé DED, spécifiquement par la mise en œuvre d'une stratégie de puissance laser variable visant à atteindre des microstructures uniformes à différentes profondeurs de dépôt. La relation entre la taille du bain de fusion, les événements de refusion, et la microstructure est examinée, en employant la méthode itérative de Newton-Raphson pour affiner la puissance laser pour des dimensions optimales de bain de fusion. Cette approche est validée par des expériences réelles, démontrant le potentiel d'atteindre l'homogénéité de la microstructure dans les propriétés matérielles à travers la profondeur de l'échantillon.

La thèse se conclut par une évaluation des propriétés mécaniques des échantillons optimisés, en utilisant des tests de microdureté et de nanoindentation. Ces évaluations révèlent des améliorations significatives en homogénéité, attribuables aux stratégies raffinées de gestion thermique et d'optimisation de la microstructure développées à travers cette recherche.

Ce travail se concentre sur le procédé DED et son impact sur l'HSS M4. Il souligne le rôle critique de la modélisation thermique et mécanique précise dans l'avancement des technologies de Fabrication Additive Métallique. Les connaissances et méthodologies développés ici offrent un soutien pour le travail en cours dans les deux équipes de recherche, fournissant une base pour une exploration et une innovation plus poussées dans la fabrication additive de métaux.

Acknowledgements

Completing this PhD has been a profoundly enriching and challenging journey, and it would not have been possible without the support and encouragement of many people.

First and foremost, I extend my gratitude to my supervisor, Anne Marie Habraken, for her guidance, patience, and expertise. Her mentorship was invaluable in shaping both this research and my growth as a researcher. Similarly, I am thankful to my co-supervisor, Anne Mertens, for her insights, encouragement, and rigorous scrutiny of my work.

Special thanks to all my colleagues in the MSM (Mechanics of Solids and Materials) group, especially Laurent Duchêne; Hoang Son Tran, Gaëtan Gilles, and Carlos Guzmán, for their help. I'm also grateful to the MMS (Metallurgy & Material Science), in particular to Jérôme Tchoufang Tchoundjang, Neda Hashemi, Hakan Paydas, and Olivier Dedry. Finally, I would like to thank Raoul Carrus from SIRRIS for manufacturing the DED samples, Olivier Milis for the mechanical tests, and Víctor Tuninetti (Universidad de la Frontera) for the help in redaction and revision of the last articles.

I would also like to thank the friends I made during my time in Liège, in particular the "Pot au lait" crew for the great evenings, the after lunch coffee group for the nice moments, the CTPL (Clube dos Trabalhadores Portugueses de Liège) ASBL for the amazing dinners, and the gafanhões for being there for me during all this time.

I cannot thank enough my parents and siblings, for their love, understanding, and endless patience. Your belief in me and your constant solidarity kept me going during the toughest times.

Finally, my deepest thanks goes to lina, whose love, patience, and unwavering support gave me the strength to finalize this journey. And to Lukas who arrived into our world bringing immeasurable joy and a renewed sense of purpose. You both fill my life with love and happiness.

Contents

Abstract	iii
Résumé	iv
Acknowledgments	v
Introduction	1
Ph.D. Context	1
Contributions	2
Ph.D. Thesis Content	4
Chapter 1 – Introduction to DED	6
1.1 The process	6
1.2 Typical DED process defects	11
1.3 The models	13
1.4 High speed steel and DED FEA	23
1.5 Summary of Chapter 1	33
1.6 References of Chapter 1	34
Chapter 2 – Article 1	40
Thermal histories and microstructures in Direct Energy Deposition of a High Speed Steel thick deposit	
Chapter 3 – Article 2	47
Sensitivity analysis in the modelling of a high speed steel thin-wall produced by directed energy deposition	
Chapter 4 – Article 3	80
Optimizing laser power of directed energy deposition process for homogeneous AISI M4 steel microstructure	
Conclusions and Perspectives	102
Annex – Compression test report	105

Introduction

Ph.D. Context

The present research is situated mainly within the framework of the fundamental FNRS PDR Project Lasercladding (2015-2019). A ULiege Faculty grant provided funding for a few additional months. Then, in its final stage, the research was conducted in parallel to another work outside the university. It represents the initial incursion of the Materials and Solid Mechanics (MSM) group into the field of additive manufacturing (AM).

The experimental part of the project was subcontracted to SIRRIS and had the collaboration of its Engineer Raoul Carrus to produce the samples used to calibrate and validate the model.

There was also the contribution of Olivier Milis from the “Laboratoire de Mécanique des Matériaux et Structures” (M&S) to perform the hot compression tests.

Much data were generated within the Walloon Region project Recyclad (RW 11-1-7335) MMS team. Ph.D. student Neda Hashemi (now Dr. Eng.) measured the thermophysical properties and did metallurgical characterization and wear tests on the studied materials (M4 and 42CrMo4). She also worked on simulations but this task was not the main focus of her research.

Within the current Ph.D. and PDR project, Dr. Jérôme Tchuindjang performed quenching dilatometry tests and provided help for all the metallurgical result analyses. Finally, Olivier Dedry did the nanoindentation tests, optical microscopy, and scanning electron microscopy analysis as well as dilatometry tests.

Note also that in addition to my Ph.D. advisors, Víctor Tuninetti from Universidad de la Frontera assisted with the redacting and reviewing of the last two articles (see contribution articles 2 and 3 hereafter).

The Ph.D. objective was to establish a comprehensive numerical model with the finite element analysis (FEA) software LAGAMINE, capable of accurately predicting thermal fields according to experimental validation, with a specific focus on the estimation of the microstructure and residual stresses in the context of the laser direct energy deposition process (DED).

To achieve this project, certain adaptations had to be made to the LAGAMINE code to address the unique characteristics of AM, such as implementing an element birth technique (done in interaction with Tran Hoang Son, a Post Doc researcher of the MSM team) and improving Switch data generation to model the boundary conditions in addition to the model of material deposition. Integrating an optimization loop to calculate a variable laser power input to ensure the creation of a melt pool of constant size was one task handled autonomously.

Many collaborations were involved during the research and the coordination of all the entities was an important task within the Ph.D., yielding interesting results as confirmed by the following list of contributions.

Contributions

From the current work, there were 3 articles focused on M4 and DED published as first author, called hereafter article 1, 2 and 3:

- 1) **R. T. Jardin**, J. Tchoufang Tchoundjang, L. Duchêne, H.-S. Tran, N. Hashemi, R. Carrus, A. Mertens, A. M. Habraken, Thermal histories and microstructures in Direct Energy Deposition of a High Speed Steel thick deposit, *Materials Letters*, Volume 236, 2019, Pages 42-45, ISSN 0167-577X, <https://doi.org/10.1016/j.matlet.2018.09.157>.
- 2) **R. T. Jardin**, V. Tuninetti, J. T. Tchoundjang, N. Hashemi, R. Carrus, A. Mertens, L. Duchêne, H. S. Tran, A. M. Habraken. Sensitivity Analysis in the Modelling of a High Speed Steel Thin-Wall Produced by Directed Energy Deposition. *Metals* 2020, 10, 1554. <https://doi.org/10.3390/met10111554>.
- 3) **R. T. Jardin**, V. Tuninetti, J. Tchoufang Tchoundjang, L. Duchêne, N. Hashemi, H. S. Tran, R. Carrus, A. Mertens, A. M. Habraken, Optimizing laser power of directed energy deposition process for homogeneous AISI M4 steel microstructure, *Optics & Laser Technology*, Volume 163, 2023, 109426, ISSN 0030-3992, <https://doi.org/10.1016/j.optlastec.2023.109426>.

And the following ones dealing with other materials as co-author:

- a) H.-S. Tran, J.T. Tchoundjang, H. Paydas, A. Mertens, **R. T. Jardin**, L. Duchêne, R. Carrus, J. Lecomte-Beckers, A. M. Habraken, 3D thermal finite element analysis of laser cladding processed Ti-6Al-4V part with microstructural correlations, *Materials & Design*, Volume 128, 2017, Pages 130-142, ISSN 0264-1275, <https://doi.org/10.1016/j.matdes.2017.04.092>.
- b) S. Fetni, T. Maurizi Enrici, T. Niccolini, S. H. Tran, O. Dedry, **R. T. Jardin**, L. Duchêne, A. Mertens, A. M. Habraken, 2D thermal finite element analysis of laser cladding of 316L+WC Composite coatings, *Procedia Manufacturing*, Volume 50, 2020, Pages 86-92, ISSN 2351-9789, <https://doi.org/10.1016/j.promfg.2020.08.016>.

Numerous conferences have demonstrated the continuous progress of the work and the applications of the developed numerical methodologies within MSM team on different materials such as Ti6Al4V, AlSi10Mg, AISI M4 materials:

Hashemi, S. N., Gilles, G., **Jardin, R. T.**, Tran, H. S., Mertens, A., Carrus, R., Lecomte-Beckers, J., & Habraken, A. (23 October 2015). *2D Thermal model of powder injection laser cladding of high speed steels (HSS)*. Paper presented at European Mechanics Society (EUROMECH). <https://hdl.handle.net/2268/196737>

Tran, H. S., Brusten, R., Paydas, H., Duchene, L., **Jardin, R. T.**, Lecomte-Beckers, J., & Habraken, A. (20 May 2016). *3-D finite element analysis of laser cladding process. Application to Ti-6Al-4V*. Paper presented at International Conference on Computational Methods in Manufacturing Processes (ICOMP'2016), Liege, Belgium. <https://hdl.handle.net/2268/200396>

Jardin, R. T., Tran, H. S., Hashemi, S. N., Lecomte-Beckers, J., Carrus, R., & Habraken, A. (05 July 2016). *A 2D and 3D thermal model of powder injection laser cladding*. Paper presented at NUMIFORM, Troyes, France. <https://hdl.handle.net/2268/214684>

Jardin, R. T., Tchuindjang, J. T., Paydas, H., Carrus, R., Mertens, A., Lecomte-Beckers, J., Habraken, A., & Tran, H. S. (28 June 2017). *Thermal history modeling to understand microstructures observed in repair technology of Ti-6Al-4V*. Paper presented at Workshop on metal additive manufacturing, Louvain-la-Neuve, Belgium. <https://hdl.handle.net/2268/213346>

Tran, H. S., Tchuindjang, J. T., Hakan, P., **Jardin, R. T.**, Carrus, R., Lecomte-Beckers, J., & Habraken, A. (2017). Thermal history modeling to understand microstructures observed in repair technology of Ti-6Al-4V. In *Extended Abstract book of 14th Conf. on Computer Methods in Materials Technology KomPlasTech 2017*. <https://hdl.handle.net/2268/206822>

Mertens, A., Hashemi, S. N., Tchuindjang, J. T., Dedry, O., Montrieux, H.-M., **Jardin, R. T.**, Tran, H. S., Carrus, R., & Habraken, A. (04 January 2018). *Laser Clad High Speed Steel thick deposits: Correlations between the local thermal history, the microstructures, and the wear mechanisms*. Paper presented at International Conference on Plasticity, Damage and Fracture 2018, San Juan, Puerto Rico. <https://hdl.handle.net/2268/217748>

Mertens, A., Hashemi, S. N., Tchuindjang, J. T., Dedry, O., Montrieux, H.-M., **Jardin, R. T.**, Tran, H. S., Carrus, R., & Habraken, A. (28 March 2018). *Influence of the local thermal history and microstructure on the wear behavior of laser clad high speed steel thick coatings*. Paper presented at 16th European Mechanics of Materials Conference, Nantes, France. <https://hdl.handle.net/2268/221718>

Tran, H. S., Tchuindjang, J. T., Paydas, H., **Jardin, R. T.**, Carrus, R., Mertens, A., & Habraken, A. (28 March 2018). *Predicted microstructure in repair technology of Ti-6Al-4V*. Paper presented at 16th edition of the European Mechanics of Material Conference, Nantes, France. <https://hdl.handle.net/2268/223074>

Jardin, R. T., Tran, H. S., Hashemi, S. N., Tchuindjang, J. T., Carrus, R., Duchene, L., Mertens, A., & Habraken, A. (25 April 2018). *2D FE Simulations of High Speed Steel Laser Cladding Process*. Paper presented at ESAFORM, Palermo, Italy. <https://hdl.handle.net/2268/226577>

Jardin, R. T., Hashemi, S. N., Tran, H. S., Mertens, A., & Habraken, A. (28 May 2018). *Sensitivity analysis of melt pool - Finite Element prediction in laser cladding process of HSS material*. Paper presented at 3rd Workshop on Metal AM, Liège, Belgium. <https://hdl.handle.net/2268/226267>

Jardin, R. T., Tran, H. S., Hashemi, S. N., Tchuindjang, J. T., Carrus, R., Mertens, A., & Habraken, A. (12 July 2018). *Modeling the Laser Cladding Process of M4 High Speed Steel*. Paper presented at International Conference on PROCESSING & MANUFACTURING OF ADVANCED MATERIALS Processing, Fabrication, Properties, Applications, Paris, France. <https://hdl.handle.net/2268/226652>

Jardin, R. T., Tchuindjang, J. T., Duchene, L., Carrus, R., Pesci, R., Mertens, A., Habraken, A., & Tran, H. S. (27 May 2019). *Thermo-Mechanical laser cladding simulations of M4 High Speed Steel*. Paper presented at 4th workshop of Metal Additive Manufacturing, Leuven, Belgium. <https://hdl.handle.net/2268/237637>

Jardin, R. T., Tchuindjang, J. T., Duchene, L., Carrus, R., Mertens, A., Habraken, A., & Tran, H. S. (2019). Numerical analysis of thermal stress in laser cladding technology of M4 High Speed Steel. In Y. Korkolis, B. Kinsey, M. Knezevic, ... Padhye, *Proceedings of NUMIFORM 2019: The 13th International Conference on Numerical Methods in Industrial Forming Processes*. <https://hdl.handle.net/2268/238397>

Habraken, A., Mertens, A., Duchene, L., Tchuindjang, J. T., Tran, H. S., **Jardin, R. T.**, Delahaye, J., Dedry, O., Paydas, H., & Carrus, R. (06 December 2019). *Microstructure prediction in additive manufacturing (TA6V, AlSi10Mg, AISI M4 materials)*. Paper presented at Séminaire mensuel Integrative Systems+Design Division, Ann Arbor, United States - Michigan. <https://hdl.handle.net/2268/243952>

Tchuindjang, J. T., Dedry, O., Paydas, H., **Jardin, R. T.**, Carrus, R., Habraken, A., & Mertens, A. (2021). *Micromechanical assessment and thermophysical characterization of HSS M4 deposits processed by LaserMetal Deposition, - a prerequisite to the validation of a thermomechanical model*. Paper presented at Thermec 2021 <https://hdl.handle.net/2268/261841>

Please note that the ongoing PhD of T.Q.D. Pham and C. Gallo developing the coupling of Finite Element approaches with other models such as Deep Learning and Proper orthogonal decomposition are still partly relying on some M4 experiments performed during this initial FNRS PDR Project Lasercladding (2015-2019).

Ph.D. Thesis content

The initial section of this doctoral thesis (Chapter 1) provides an introduction to DED and the development of FEA models specifically tailored for DED processes. Additionally, it delves into the unique characteristics and properties of the M4 high speed steel (HSS). The next section encompasses the articles generated as part of this PhD thesis. They investigate various aspects related to DED and FEA modeling.

This doctoral thesis is structured into different chapters, each aimed at equipping the reader with the necessary knowledge and skills to comprehend the methodology for developing an FEA model capable of accurately calculating thermal fields. The thermal fields serve as the foundation for predicting microstructure (article 1 – Chapter 2) and residual stresses (article 2 - Chapter 3). Additionally, a novel method is introduced for generating a variable laser

power function, enabling the production of constant-height melt pool for each layer using DED (article 3 – Chapter 4). The effectiveness of this FE approach has been validated through experimental investigations.

Finally, the concluding Chapter 5 summarizes the findings, offers conclusions, and presents prospects for future research in the field.

Chapter 1- Introduction to DED

1.1 The process

Additive Manufacturing (AM), also known as 3D printing, has revolutionized the manufacturing industry by enabling the production of complex and customized parts with unprecedented design freedom. The technologies and methods of AM currently continue to expand in terms of applications and market share, driven by sectors such as automotive, medical, aerospace, and space. As expected by Gausemeier, 2011, it has been extended to other sectors such as defense, jewelry, sports, textiles, and tooling. Both industry and numerous academic institutions have significantly contributed to the development of these technologies, with a total of 3,500 patents filed between 1971 and 2011 (Weber 2013). In 2018, the AM market (including machine sales, materials, software, and associated services) was valued at \$9.3 billion according to the annual report by SmarTech Analysis (SmarTech 2020).

In terms of processed materials, polymers initially dominated the market, accounting for nearly 60%. However, the metal AM market is also growing. In recent years, there has been a trend towards using metal AM for the production of structural components, particularly in fields such as aerospace and automotive sports, which can benefit from significant weight savings (Mahamood 2014) while minimizing the buy-to-fly ratio. For example, the entire heat exchanger assembly of the Boeing 777x GE9X engine, which used to consist of 300 parts, has been reduced to a single component that is 40% lighter and 25% cheaper (Blakey-Milner 2021). NASA will soon replace the main engine of the space shuttle with AM parts to reduce their production time and weight (Gradl, 2020). The medical sector is also making use of AM, with the successful printing of various titanium surgical implants (Jamróz 2018).

Through a collaboration between the American Society for Testing and Materials (ASTM) and the International Organization for Standardization (ISO), the standard 52900:2015 (ISO 52900:2015) was developed, dividing metal additive manufacturing (AM) into two main families: Directed Energy Deposition (DED) processes and Powder Bed Fusion (PBF) processes (Figure 1). DED technologies involve a continuous flow of feedstock material and a concentrated energy source (Dutta 2022), typically in the presence of an inert protective gas. The input energy density enables the fusion of the material, leading to the formation of a molten pool (Armstrong 2022). There are several DED processes (Gibson 2015), varying based on the form of the feedstock material (powder or wire) and the type of energy source (thermal - fusion or kinetic). Fusion sources can include laser beams, electron beams, laser plasma, or electric arcs. In the case of the ColdSpray process, particles are projected onto a substrate at ultrasonic speeds, and the kinetic energy is converted into thermal energy upon impact, allowing the particles to adhere to the substrate and form a coating (Moridi 2014). Thus, each DED process relies on a combination of the material form and the type of energy source: wire/electric arc (CMT or WAAM, TIG/plasma), wire/laser (DED-LW), wire/electron beam

(EBAM), and powder/laser (DED). PBF processes differ from powder-based DED processes as the particles are first deposited as a powder bed, upon which a laser source (formerly known as SLM, now called LPBF according to the current standard) or an electron beam (EBM) moves and selectively fuses the material.

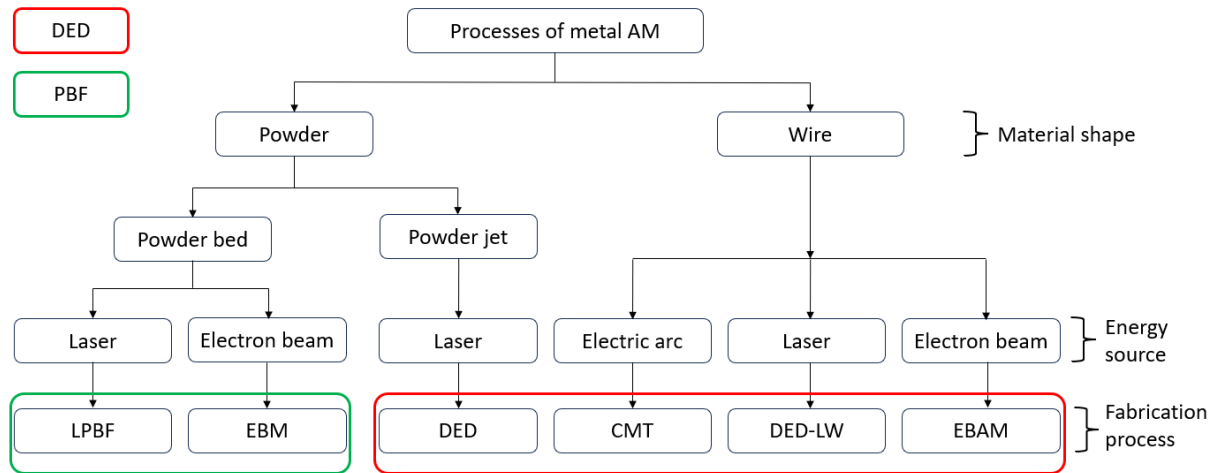


Figure 1 – Different metal additive manufacturing processes (SLM now called LPBF), adapted from (Leroy-Dubief 2023).

Among the various AM processes, Laser Directed Energy Deposition (DED), also known as Laser Cladding, is the process of interest for this research. It has emerged as a versatile technique for manufacturing fully dense parts through the progressive welding of a wire or metal powder onto a substrate material. DED offers advantages (Griffth 1999) such as high controllability, a high potential in cladding uneven substrates, achieving high cooling rates, and generating fine microstructures. Once optimized, the process can minimize distortion and produce high-quality deposits. This technique is widely used for manufacturing new parts, adding features to existing parts, as well as for cost-effective repair applications. It is also suitable for the production of functional prototypes and small series (Pinkerton 2008, Gibson 2015, Hascoët 2018). Another advantage of DED over other additive manufacturing processes like Selective Laser Sintering (SLS) or Fused Deposition Modeling (FDM) is the ability to deposit multiple materials simultaneously or sequentially. This capability allows for the creation of multi-material gradients, and the incorporation of functional elements within a single part. Additionally, DED processes offer a high deposition rate, thus allowing for rapid manufacturing applications. However, certain challenges still need to be overcome, such as microstructure monitoring, geometry accuracy, and crack formation at the substrate-deposit interface or within the clad itself (Griffth 1999). Achieving accurate predictions of thermal history, microstructure evolution, and residual stresses is thus a key to controlling the quality and performance of the manufactured parts.

The DED process begins with a CAD model of the desired part, which is then sliced into layers for the deposition process. A high-powered laser is used to melt a wire or powder feedstock material projected onto the substrate, or previous layers creating a molten pool. The laser

beam and the powder feeding scan the surface of the substrate, melting the added powder material and allowing it to fuse with the previous layers, forming a solid part. During the deposition, the laser power, scanning speed, and material feed rate are carefully controlled to maintain optimal conditions for bonding and minimize defects. The process is performed in a controlled environment, typically with the use of shielding gases to prevent oxidation or contamination (Figure 2). After the completion of the deposition, the part might undergo post-processing steps such as heat treatment, machining, and surface finishing to achieve the desired final characteristics.

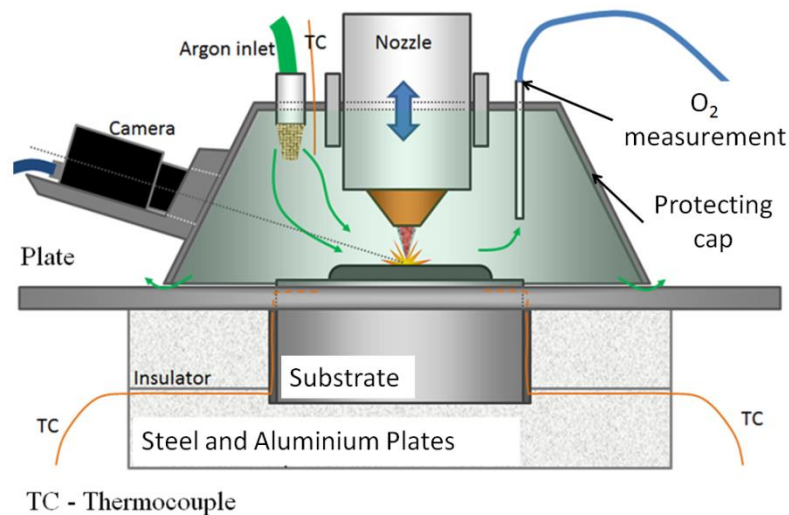


Figure 2 - Scheme of Sirris laser cladding equipment used for manufacturing thin wall and bulk specimens. (Hashemi 2017).

The powder delivery system plays a crucial role in maintaining the consistency of powder focus with the laser beam focus in DED processes. Several parameters of the powder delivery system, including powder feed rate, delivery gas flow rate, nozzle size, shape, location, and powder impingement, influence this consistency. Various configurations of nozzles for DED exist, as depicted in Figure 3 (Milewski 2017). The simplest configuration involves a single wire or powder feeding nozzle (Figure 3 a and b), where the relationship between the powder focus, laser beam, and melt pool is predetermined. This relationship includes the positioning of the powder focus, the distance between the melt pool and the feeder, and the angle of incidence of the powder focus. Any change in the focal position can affect the energy penetration depth, leading to variations in the dilution of the base material due to the deposition of the build material.

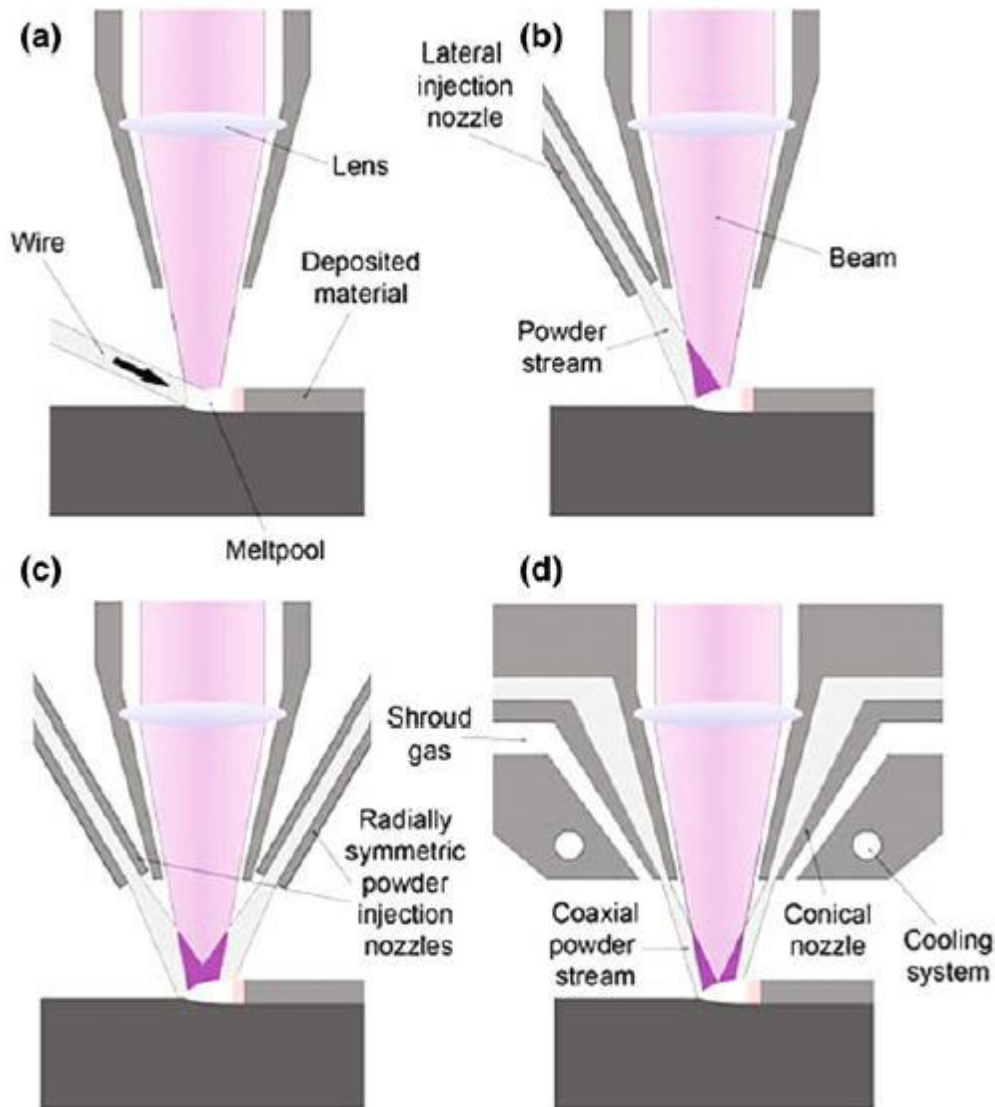


Figure 3 - DED Nozzle Configuration (Milewski 2017).

In DED processes, the laser is commonly operated in continuous mode, and the energy distribution can be Gaussian or Top-Hat depending on the machine settings or operator's preference. When the powder is in flight, a portion of the laser energy is absorbed by the powder particles, while another portion is absorbed by the substrate, resulting in the formation of a melt pool (Marion 2016). The remaining laser energy is reflected from the powder particles and substrate. The amount of laser energy absorbed by the powder particles during their flight, known as laser attenuation, is influenced by various process parameters such as powder density, in-flight duration, and gas velocity (Manvatkar 2014). Figure 4 reminds all the phenomena present in the DED process.

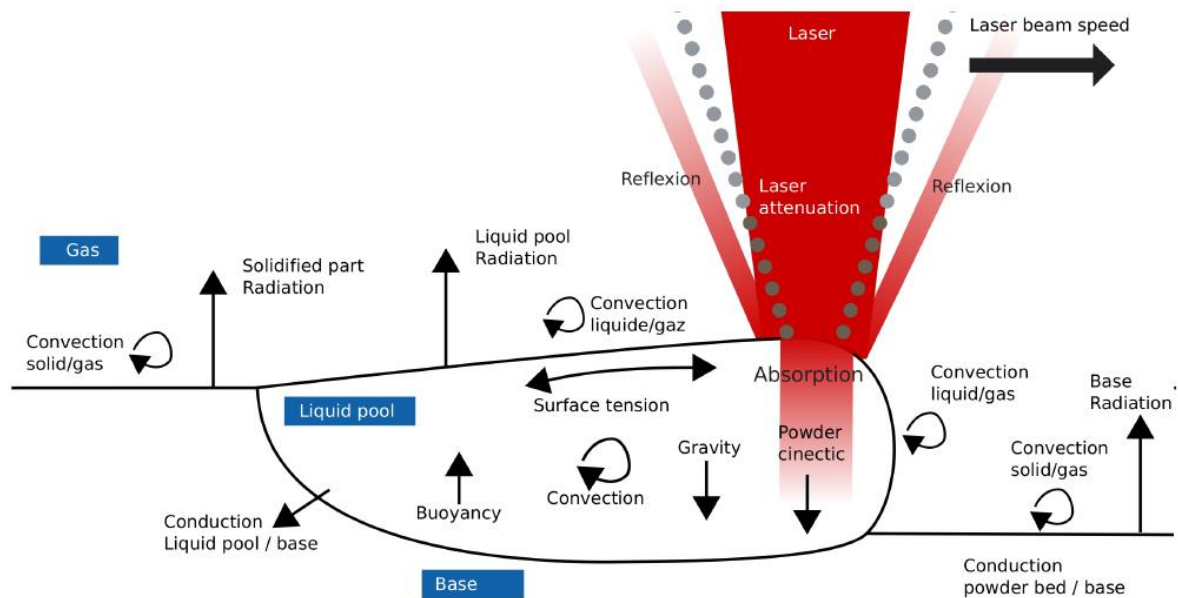


Figure 4 - Physical phenomenon during laser material interaction in DED (Marion 2016).

In the context of setting up a numerical model for the analysis of the final microstructure and distortion of a DED part, it is crucial to determine the exact outputs. Figure 5 (Nain, 2022), illustrates the main phenomena and their coupling in DED. If indeed plastic dissipation has a poor effect, the weak coupling assumed in this figure for metallurgical transformation and mechanical stress could be discussed depending on the material and the process parameters.

The laser-material interaction generates a melt-pool due to the high laser energy input. The resulting melt-pool temperatures, exceeding the fusion temperature, lead to thermal expansion. Subsequently, as the laser heat source moves away, the cooling down phenomenon induces thermal contraction. These thermal expansion and shrinkage phenomena generate significant stresses and strains, which can cause cracks and distortions in the workpiece. Additionally, if metallurgical transformations occur, they affect the deformation and mechanical properties of the workpiece, particularly due to different material properties between phases, such as in the case of high speed steel (HSS) (see below, section 4 in this chapter). Furthermore, during the DED process, phenomena like annealing can result in stress relaxation and reduced distortion. Therefore, the final thermal expansion and shrinkage are strongly influenced by the amount of laser energy absorbed and the conduction heat transfer in the workpiece, emphasizing the critical role of temperature as the driving force for the mechanical analysis in DED. Consequently, to develop an accurate numerical model, it is essential to accurately capture the temperature field through heat transfer analysis to obtain the correct distortion field through mechanical analysis. This will be discussed in more detail in section 3 devoted to models.

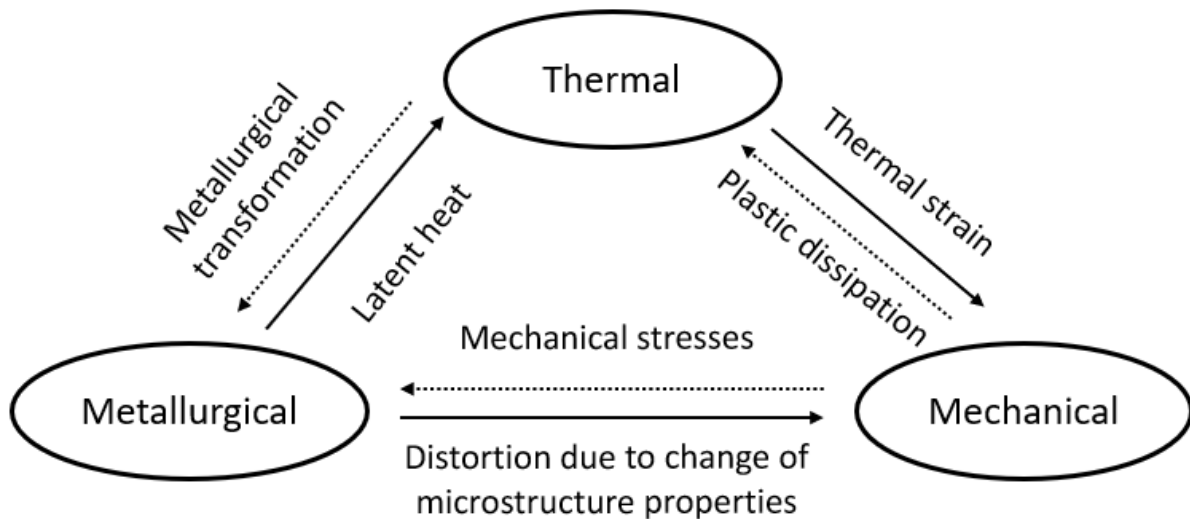


Figure 5 - Different physical phenomena happening in DED. Dotted line represents weak coupling and full line representing strong coupling. (Nain 2022).

1.2 Typical DED process defects

Defects in DED can arise due to various factors, which must be thoroughly understood and mitigated to achieve high-quality and reliable parts. A full description of defects in DED can be found in (Tematio 2022). One such defect is warping, characterized by the undulation of the upper surface caused by excessive laser energy input without effective heat dissipation, resulting in a deeper fusion pool (Figure 6). Another common defect is border defects, which occur due to material deposition discontinuity and improper nozzle paths, leading to significant deviations between the levels of the edges and the average surface level (Figure 7). These defects are frequently observed at the beginning and end of the material deposition path or during abrupt changes in the direction of the nozzle path. Additionally, surface satellites (Figure 8), appearing as more localized spherical protrusions compared to border defects, can be observed at overlapping points between the starting and ending points of metal deposition. These surface satellites originate from the splattering of unfused powder and its accumulation at specific points on the surface of the component. Moreover, the shrinkage of material layers during the cooling process can cause the inclination of the lateral surfaces of the constructing component. Warping, which leads to detachment from the substrate, is primarily caused by weak adhesion between the material layer and the substrate, compromising the ability of the component/substrate contact area to withstand residual stresses generated during the process (Figure 9 and Figure 10). This weak adhesion is typically associated with low laser power or high transversal speed, resulting in a fusion pool that lacks sufficient width and depth for proper component-substrate adhesion. Therefore, a comprehensive understanding and effective mitigation strategies for these defects are essential in optimizing the quality and reliability of parts produced through DED processes.

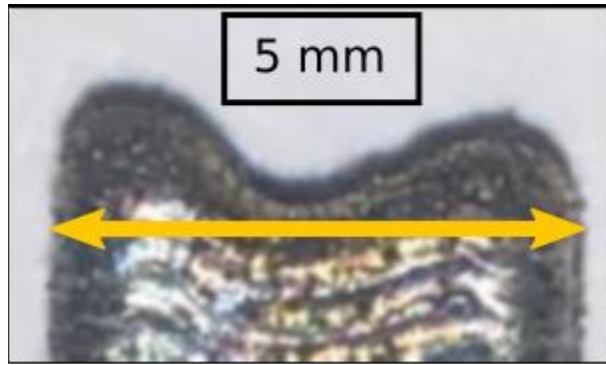


Figure 6 - Warpage of the top surface of a DED part (Liu 2020).



Figure 7 - Edge defects of a DED part (Miedzinski 2017).

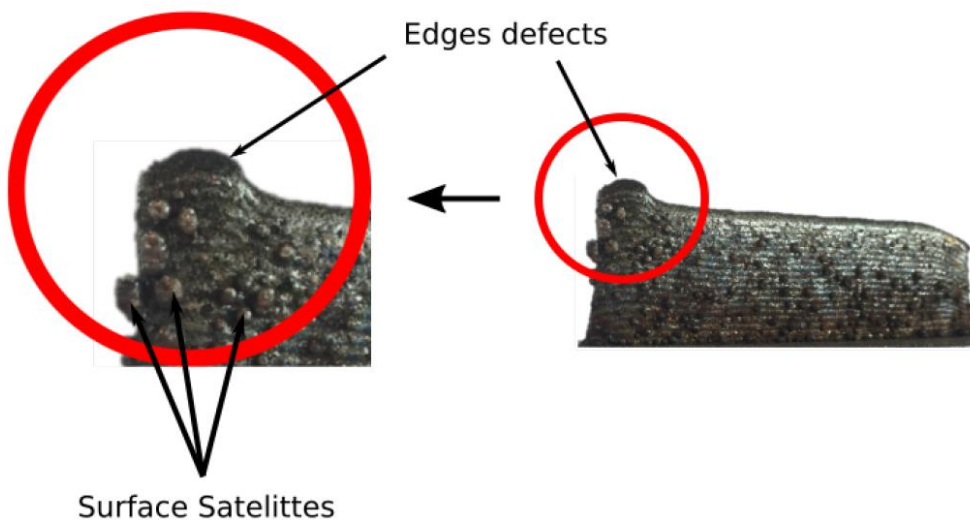


Figure 8 - Surface satellites on a DED part (Miedzinski 2017).



Figure 9 - Warpage of an DED part leading to its detachment from the substrate (Miedzinski 2017).



Figure 10 - Warping leading to build-part's detachment from the substrate/base-plate (Nain 2022).

1.3 The models

Directed Energy Deposition (DED) is a prominent additive manufacturing (AM) technique that holds substantial promises in fabricating intricate structures with improved efficiency and reduced material wastage. The optimization of DED processes heavily relies on accurate modeling and simulation. This text compiles state-of-the-art knowledge, discussing the role of simulation techniques and the challenges associated with DED.

Simulation techniques, including finite element analysis (FEA) and computational fluid dynamics (CFD), have been pivotal in understanding and optimizing DED processes. These simulations enable predictive analyses of heat transfer, fluid flow, and material behavior, which aid in comprehending the complex phenomena occurring during deposition (Pinkerton 2008). Researchers have focused on scrutinizing the effects of various process parameters, such as laser power, scanning speed, powder feed rate, and gas shielding, on the geometrical accuracy, surface roughness, and mechanical properties of DED-fabricated components (Wang 2008). This knowledge has, in turn, allowed other researchers to optimize process parameters

to achieve desirable outcomes, including minimizing distortion, controlling thermal gradients, and optimizing material properties (Jardin 2019, Tran 2017).

Furthermore, simulation techniques, such as solid finite element analysis (FEA) and computational fluid dynamics (CFD), have been employed to model DED processes for many years. For instance, Alimardani et al. (Alimardani 2007a) presented a 3D thermomechanical solid FE model capable of predicting the geometrical and thermal properties of a four-layer thin wall of AISI 4340 Steel manufactured by laser and powder. In 2011, Lundbäck and Lindgren (Lundbäck 2011) described walls manufacturing of 40 passes based on their former work developed for multi-pass welding (Lindgren 2001), also utilizing 3D solid FEA. Keyhole evolution within welding was already studied by CFD in 2002 by Ki et al. (Ki 2002). Subsequently, DED has naturally been simulated (Qi 2006), taking into account heat transfer, phase changes, and fluid flow in the molten pool within a controlled-volume finite difference method where temperature and fluid velocity were solved in a coupled manner.

One of the critical parameters in laser cladding is the melt pool size, which plays a significant role in determining the optimal process conditions for achieving the desired microstructures and properties (Lewis 2000). Researchers have extensively studied the influence of process parameters on the melt pool size, using advanced 3D FEA models to achieve a steady melt pool size and temperature distribution during deposition (Wang 2008). Understanding the melt pool size is crucial, and FEA is commonly used for its prediction (Yang 2010, Fetni 2021).

Thermo-physical Properties of Materials

Thermo-physical properties of the deposited material, such as thermal conductivity, specific heat capacity, and density, significantly influence the heat transfer and solidification behavior during DED. The accuracy of DED simulations depends on the precision of input material parameters. Researchers have found that relying on properties measured on samples produced by the studied process is crucial for achieving accurate results. The significance of thermo-physical properties has been demonstrated through experiments and measurements (Heigel 2015, Fetni 2021). Obtaining data is challenging, as material properties can vary with temperature, powder characteristics, and post-processing treatments. To improve the accuracy of material property data for DED, advanced characterization techniques, including differential scanning calorimetry (DSC), differential thermal analysis (DTA), and laser flash diffusivity (LFA), have been used to measure thermal properties, such as thermal diffusivity and conductivity, as well as specific heat capacity. Microstructural analysis methods like optical microscopy, scanning electron microscopy (SEM), and X-ray diffraction (XRD) have been employed to study microstructure evolution and mechanical properties (Gockel 2014).

The accurate representation of material mechanical properties at high temperatures, such as visco-plastic behavior, is also crucial for reliable simulations. However, most material data utilized in thermo-mechanical models are derived from samples not specifically manufactured by DED. Generic material databases developed for other manufacturing processes, such as casting or forging, are often insufficient for accurate simulations in additive manufacturing. Sensitivity analyses have highlighted the significant impact of mechanical properties, such as

the thermal expansion coefficient and elastic limit, on the distortion and residual stresses, emphasizing the need for accurate material data specific to DED processes and materials.

The significance of thermophysical properties on simulation accuracy is further explored in Chapter 3, particularly in the context of M4 and substrate materials.

Understanding Microscale and Macroscale Phenomena

At the microscale, fluid-based methodologies like CFD have played a crucial role in understanding phenomena like the balling effect, pore formation, and flaw mechanisms in specific materials (Wang 2020). These approaches, while useful, face limitations when simulating whole parts due to computational time constraints. For understanding segregation behavior and phase generation, lower-scale models like Phase Field approaches could be necessary. However, as exemplified by (Jardin 2019), FEA can explain how the precipitation of carbides within M4 cladding leads to a heterogeneous distribution of carbide shape, size, and nature along the depth of a cladded sample. To study diffusion phenomena, phase field methods have been employed in ULiege (Delahaye 2019) to investigate the diffusion between Si inclusions and an Al matrix in AlSi10Mg, and determine the rupture location in LPBF AlSi10Mg. However, due to the complexity of carbide precipitation present in HSS material such method is currently not yet applicable for this type of material. At the macroscale, inherent-strain-based methods have been used to analyze complex parts, often requiring experimental calibration (Setien 2018). Detailed FEA offer a comprehensive understanding of the thermal history, microstructure evolution, and resulting residual stresses, impacting the quality and performance of manufactured parts.

Simulating DED processes involves choosing various modeling scales, but the thermal field is consistently a driving factor. Meso-scale simulations in CFD provide details about fluid movements within the melt pool, crucial for simulating phenomena such as porosity formation and the distribution of precipitates. Figure 11 provides an overview of modeling strategies for DED at meso and part scales (Bayat 2021). At the macro-scale, FEA simulations predict part distortions and residual stress fields but often oversimplify phenomena within the melt pool. These simplifications limit predictions regarding solidification states and microstructure features like grain growth and morphology. On the other hand, they limit the CPU time and allow modeling the whole process.

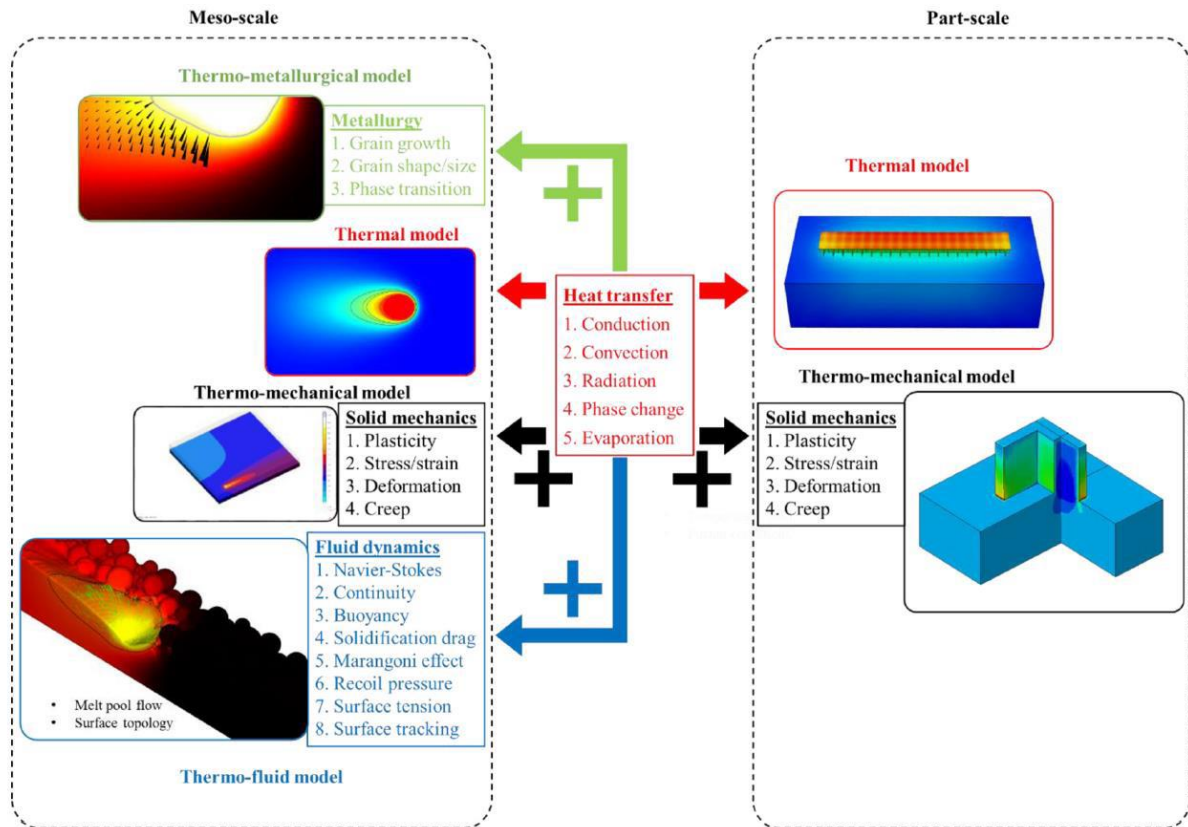


Figure 11 - Modeling strategies for DED at meso & part scale (Bayat 2021).

Advanced Metallurgic Models

Advanced metallurgic models such as Phase Field or Cellular Automata approaches can model solidification, grain nucleation and growth, texture formation and phase transformation. A large number of commercial software packages, including Thermocalc, DICTRA, JMatPro, and MICRESS have been developed to predict the microstructure evolution based on thermodynamic knowledge (found for instance in CALPHAD data base). Phenomenologic laws such as Johnson-Mehl-Avrami-Kolmogorov (JMAK) equations or Koistinen Marburger (KM) can also provide interesting information about solid transformations. For instance, Crespo's model (Crespo 2010) relying on JMAK and KM has been applied on Ti6Al4V DED deposition within Esteva Master thesis predicting Ti6Al4V phases (Esteva 2018) for experiments performed by Sirris [Paydas 2015].

FEA simulation

As the present thesis aims the part scale, this introduction will discuss hereafter the different choices of a thermal FEA approach: the heat source model, the morphology of the layer and the coupling with deep learning.

About the thermo-mechanical models able to predict the part distortions and residual stress field, most models work in a staggered way, first the thermal field is computed then the mechanical stress and strain are updated using the temperature field as loading.

AM simulations are very consuming from the CPU time point of view, due to the long laser path and the refined mesh closed to the heat source. Many techniques are used to speed up the processes. Only a few of them will be presented.

Heat Source Models and Methodologies to Reduce Simulation Time

To accurately simulate DED processes, heat source models are critical. Various surface and volumetric heat sources have been applied by researchers, such as Goldak's double ellipsoid heat source (Goldak 1984). Researchers are continuously refining these models to better account for phenomena like heat transfer by convection (Marangoni flow) (Wei 2015). Some authors define initial hot temperatures of new nodes in the birth element technique, instead of using heat sources they prefer simplicity to a better control of energy input. For laser DED simulations, Table 1 from V. Nain's PhD thesis [Nain, 2022] summarizes in a synthetic way the diversity of surface and volumetric heat sources that are currently applied by modelers.

In thermal simulations, simplified analytical solutions for moving point heat sources, such as the Rosenthal equation or Eagar–Tsai model, often serve as initial approximations for LPBF. However, in DED process, where energy levels are higher and melt pool sizes substantially differ, the application of these models is limited. Wang (Wang 2008) introduced a compelling reduced-order multivariable model for DED. This model parameterizes the material transfer rate as a function of process parameters, offering improved predictions of steady-state melt-pool geometry compared to existing lumped-parameter analytical models. The accuracy and validity of Wang's predictions were validated using experimental data obtained from TA6V deposition on a Laser Engineering Net Shaping (LENS) AM process, complemented by finite element analysis.

For DED, Nain's methodology (Nain 2022) relies on a classical FEA thermal model to analyze thermal fields in 316L thin walls across various process parameters. Nain's innovation involves defining a thermal mean source over larger time increments and spatial domains, enabling the use of larger time steps to expedite the thermal process. Although this approach yields efficient results, a notable drawback is the dependence on a correction factor that can modify energy input.

Table 1 - Different type of numerical heat sources used in the literature for DED (Nain 2022)

Name & Type	Expression	References
Gaussian: Surface	$Q = \frac{AP}{\pi r_o^2} \exp\left(\frac{-2r^2}{r_o^2}\right)$	(Alimardani et al., 2007a, 2007b; Fallah et al., 2011; Johnson et al., 2018; Labudovic et al., 2003; Madireddy et al., 2019; Manvatkar et al., 2011; Neela and De, 2009; Wang and Felicelli, 2006)
Top-Hat: Surface	$Q = \begin{cases} \frac{AP}{\pi r_o^2}, & -r_o \leq r \leq r_o \\ 0, & r > r_o \end{cases}$	(Peyre et al., 2017)
Conico-Gaussian: Volumetric	$Q = \frac{2AP}{\pi r_o^2 H} \left(1 - \frac{z}{H}\right) \exp\left(1 - \frac{r^2}{r_o^2}\right)$	(Biegler et al., 2020, 2018b, 2018a; Mukherjee et al., 2017; Liang Wang et al., 2008; L. Wang et al., 2008)
Cylindrical: Volumetric	$Q = \begin{cases} \frac{AP}{\pi r_o^2 H}, & -r_o \leq r \leq r_o \\ 0, & r > r_o \end{cases}$	(Lu et al., 2018a; Piscopo et al., 2019)
Goldak: Volumetric	$Q = \frac{6\sqrt{3}APf_{f,r}}{a_{f,r}bc\pi\sqrt{\pi}} \exp\left(-\frac{3x^2}{a_{f,r}^2} - \frac{3y^2}{b^2} - \frac{3z^2}{c^2}\right)$	(Anca et al., 2011; Erik R Denlinger et al., 2015; Denlinger and Michaleris, 2016; Goldak et al., 1984; Heigel et al., 2015; Michaleris, 2014; Xie et al., 2019, 2020a; Yang et al., 2016)

As we transition from thermal to thermo-mechanical simulations, the inherent strain method emerges as a valuable tool. This method simplifies standard models, offering a relatively direct approximation for calculating residual distortions and stresses after the AM process. It operates by solving a limited number of mechanical equilibrium problems using the inherent strain as the loading field, a technique initially developed by Ueda et al. (Ueda 1975) for welding processes. Over the past decades, the inherent strain method has been extended to AM processes, including LPBF and DED. Tematio (Tematio 2022) compared it to traditional FEA and achieved good stress prediction (Figure 12).

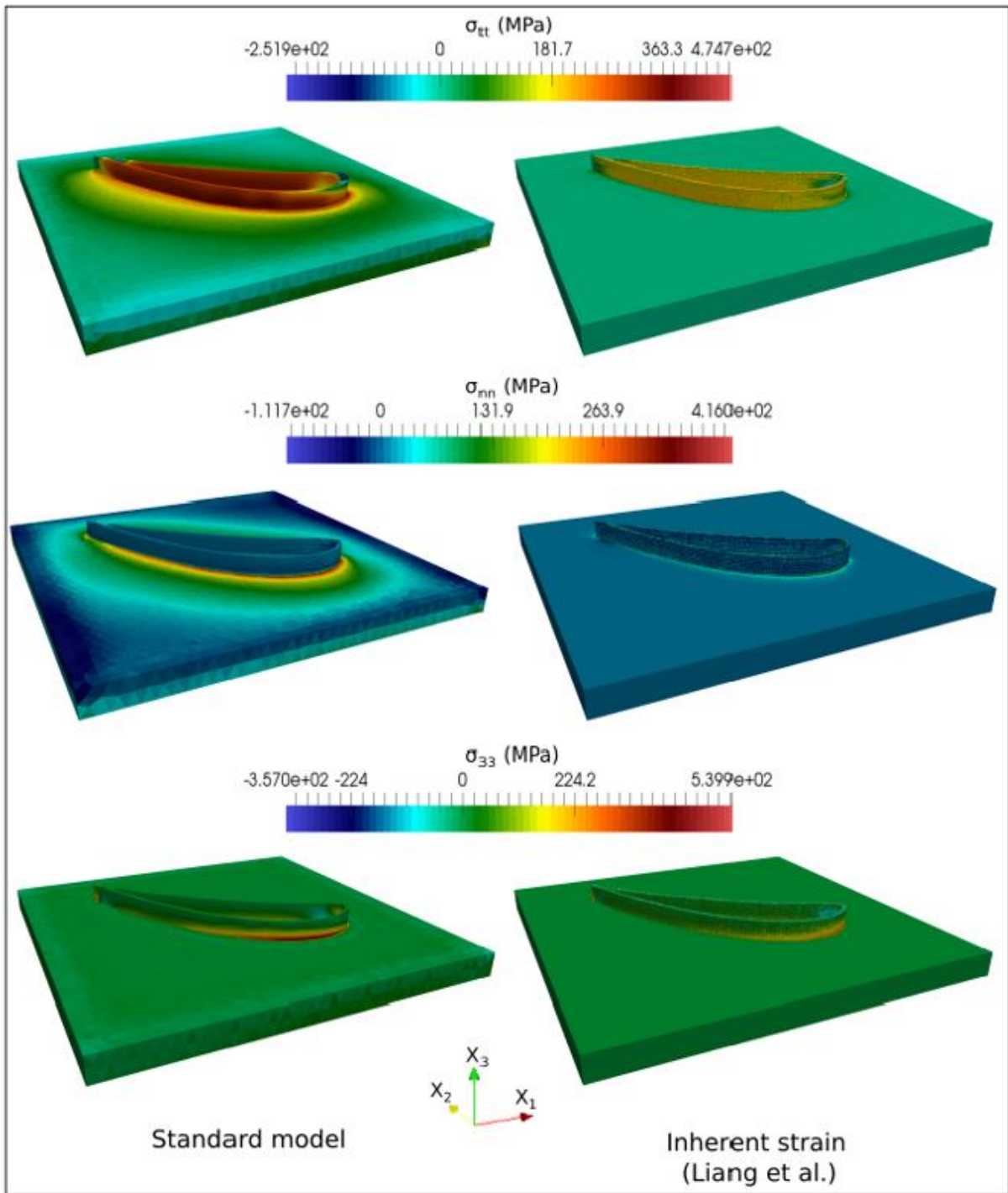


Figure 12 – Validation test for the inherent strain method. Residual stress field after building an eight layer blade. On the left, the results from FEA and on the right the results from the inherent method strain (Tematio 2022).

The inherent strain method, although less accurate, is frequently used to predict residual distortions and stresses (Tematio 2022). Several variants of this method exist, they vary by the steps and the critical aspect of computing the inherent strain field. This field can be derived from previous FE simulations or extensive industrial experiments. While this method may not be applied in this specific PhD thesis, it remains a pivotal tool for industrial applications due to its ability to address residual stress, although with some limitations in accuracy compared to distortion fields.

To reduce simulation time, various techniques have been employed. Dynamic remeshing and the use of a thermal mean source with larger time increments help speed up FEA calculations (Nain 2022).

Denlinger et al. (Denlinger 2016), for example, employ dynamic remeshing to estimate thermal fields and residual stresses in LPBF. This approach reduces the number of degrees of freedom during incremental calculations. Another noteworthy approach, presented by (Leroy-Dubief 2023), involves coupling a finite element model with a proper orthogonal decomposition (POD) method. This strategy leverages the cyclic thermal behavior inherent in the repetitive nature of the AM process. However, it's crucial to recognize that while a single equation can offer valuable insights, its applicability is inherently limited.

Deep Learning (DL) Applications

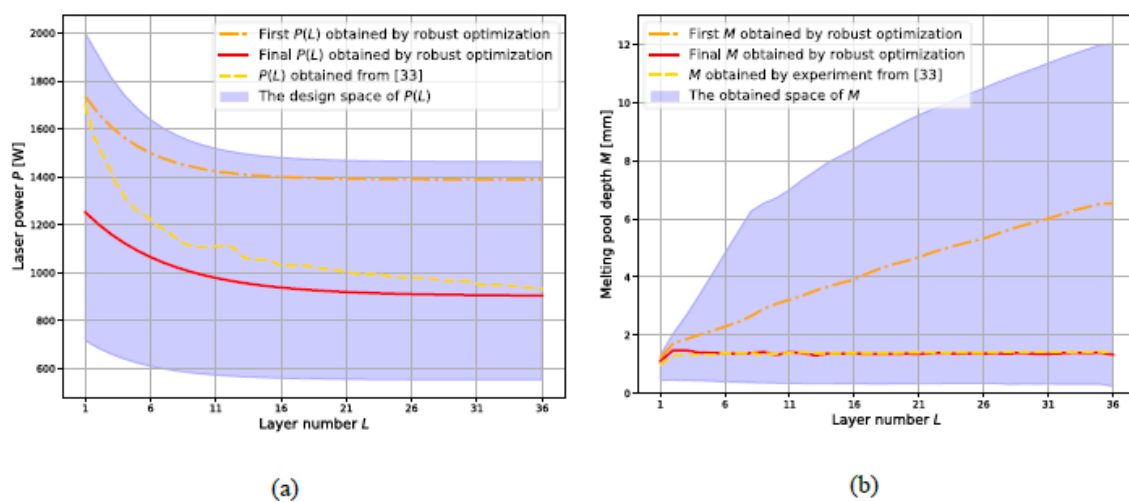


Figure 13 - $P(L)$ and M are the laser power function and melt pool depth respectively used by T.Q.D. Pham in his DL approach in the M4 bulk sample studied in chapter 4 of the current thesis. a) comparison of $P(L)$ identified by classical FE optimisation or DL for the same target of melt pool size, b) comparison of M evolution versus the different layers computed by both method associated to $P(L)$ and verified by experiments.

Deep Learning (DL) has also entered the field of simulating AM processes, saving significant computation time. Surrogate models, such as feedforward neural networks (FFNN), provide rapid and accurate predictions of temperature evolutions and melt pool sizes (Pham 2022a). The application of DL to DED helps analyze uncertainty propagation and optimize laser power functions for a constant melt pool size (Pham 2023). Note that the current thesis defined the basic validated FE simulations that allowed the PhD student T.Q.D. Pham to apply these techniques to define the surrogate model FFNN in a metal bulk sample (36 horizontal layers) manufactured by the DED process (Pham 2022a). The speed of this surrogate model allowed to analyze the uncertainty propagation in the studied DED process (Pham 2022b). Finally in (Pham 2023), this surrogate model allowed to overcome the computational challenge of the robust optimization under uncertainty. As confirmed by Figure 13, DL can recover the optimum laser power function able to generate a constant melt pool size during the DED bulk part manufacturing found by a classical FEA approach in chapter 4.

In essence, the integration of DL techniques into AM simulation not only enhances computational efficiency but also paves the way for robust optimization within intricate manufacturing processes.

The Morphology of the Layer

Traditionally, many thermal and thermo-mechanical FE simulations in AM treat layer morphology—specifically, height and width—as constant input data based on experimental knowledge. However, for thin walls generated by DED, alternative approaches have emerged. Alimardani and co-authors (Alimardani 2007b), drawing inspiration from earlier work by Toyserkani (Toyserkani 2005), established a relationship between material deposit layer height and various process parameters. Building on this foundation, C. Dubief-Leroy's recent PhD research (Leroy-Dubief 2023) (Figure 14) introduced a predictive model for layer height in DED thin walls. This model is applied for constant laser power and powder feed rate however it allows for variation in the distance between laser-clad, which, in turn, affects the layer's height.

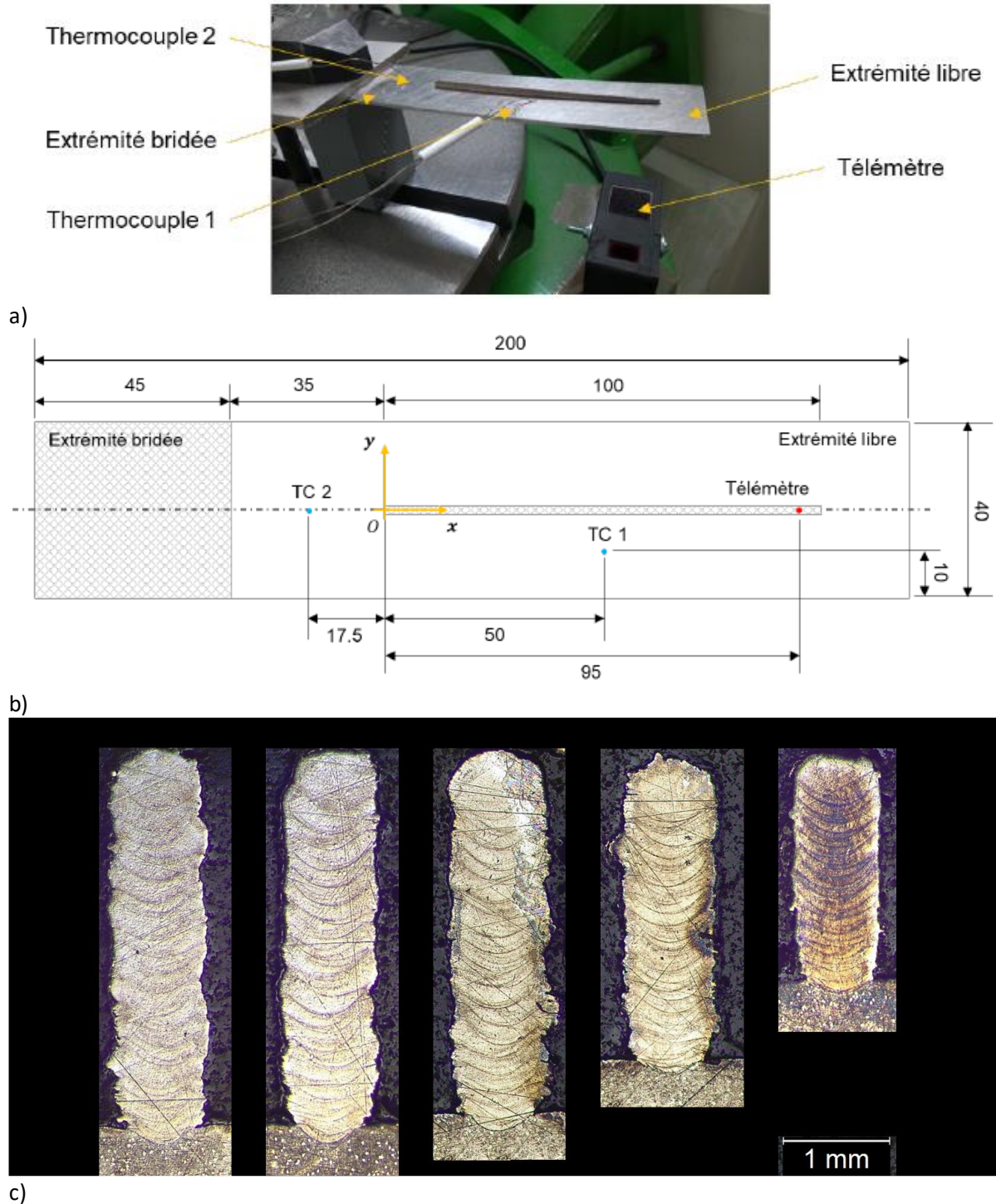


Figure 14 – a) Experiment design, b) Sample geometry and location of measurements, c) Cut in a thin wall in 316L of 20 layers manufactured by DED with the experimental design described in a- and b) (Dubief-Leroy 2023).

Dubief-Leroy's work revealed that the layer height is influenced by two key parameters: the working distance between the laser and the clad and the laser increment displacement per layer, which varies due to bending induced by thermal load. However, to comprehensively understand and anticipate critical defects in part production or material health, a thermal approach must complement this geometric model.

For bulk samples, Saracibar's approach (Saracibar 2014), drawing from earlier welding simulations by Lindgren (Lindgren 2001), minimizes an objective function to identify the deposited material volume and shape. This function considered factors such as boundary smoothness, element distortion, and the volume of added material (Figure 15a). It's important to note that the final validation of this approach didn't solely rely on these criteria (Figure 15b).

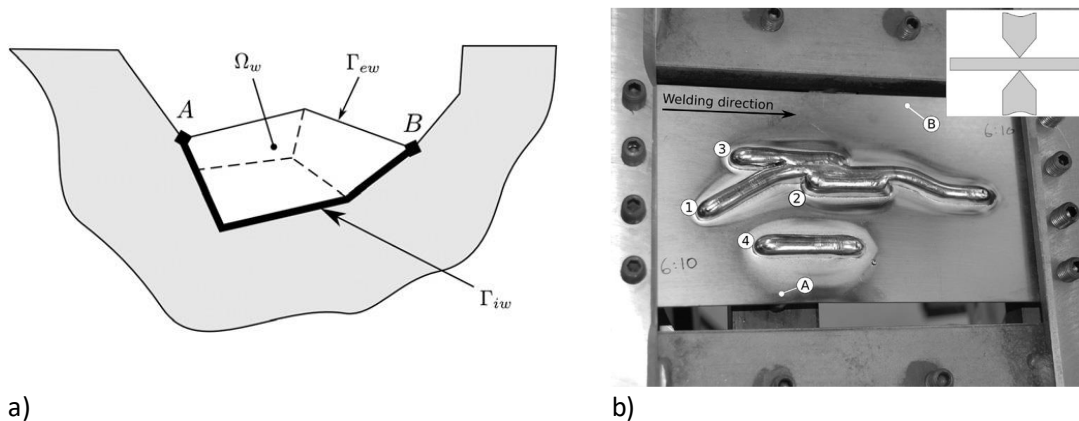


Figure 15 - a) Notation used for definition of weld geometry according to (Lindgren 2001); b) Validation part of (Saracibar 2014), complex thin wall of 10 layers.

The current thesis and Saracibar work, apply the birth element technique. This technique can lead to complications if the non-activated element shape in the initial mesh doesn't match the actual geometry formed by previous layers. While the current thesis resolved this issue given its relatively simple geometry, Tematio's PhD work (Tematio 2022) offers an elegant solution. Tematio addressed this problem through a theoretical approach involving large deformations within the DED process, utilizing a configuration linked to the Computer-Aided Optimization (CAO) geometry and an Eulerian frame linked to the laser location. This approach effectively managed both the activated and non-activated domains, implementing features of incompressibility and a penalty factor to mitigate distortion.

It's also important to note the Particle Finite Element Method (PFEM) as an alternative solution. PFEM offers a unified framework for handling both the shape of added material and the challenges posed by distorted elements through continuous mesh adaptation, making it highly relevant to Additive Manufacturing, as showcased in B. Bobach's PhD work (Bobach 2023).

1.4 High speed steel and DED FEA

Tool steels are essential for a wide range of material shaping operations, encompassing machining, cold and hot forming, molding, spinning, and extruding (Lévêque, 2013). These steels exhibit carbon content ranging from 0.1% to more than 1.6% and are typically alloyed with elements such as Mo, Cr, and V (Bayer, 1989). They are categorized into four classes based

on their future use: non-alloyed and alloyed tool steels for cold working, alloyed tool steels for hot working, and high-speed steels (HSS).

During shaping operations, tools endure complex stresses, necessitating specific properties in HSS. These include high hardness to withstand surface deformations, wear and scratch resistance to minimize adhesion and micro separation, toughness against mechanical shocks, resistance to thermal shocks in hot rolling mills with sudden temperature changes, and high hardenability to ensure a homogeneous structure after quenching heat treatment (Bayer, 1989; L  v  que, 2013). Achieving this set of characteristics involves incorporating various alloying elements into the steel like Carbon, Vanadium, Chromium, Tungsten, Molybdenum, and also Silicon and Manganese (Bayer 1989, L  v  que 2013, Boccalini 2001, Okane 2001, Pan 2004, Tchuindjang 2015).

These alloys exhibit high hardness (60-70 HRC) at room temperature thanks to the combination of a (tempered) martensitic or bainitic matrix with very hard alloyed carbides, generally located at the grain boundaries (Boccalini 2001, Okane 2001, Pan 2004, Tchuindjang 2011, Wang 2023). In comparison to conventional manufacturing processes such as conventional casting (with or without ESR) or spin casting, the very fast cooling and solidification rates of additive manufacturing techniques and particularly of DED process were found to lead to a strong microstructure refinement together with changes in the carbides morphologies and distribution (Hashemi 2017, Wang 2023). In the following paragraphs, experimental results from the Ph.D. work of Neda Hashemi (Hashemi 2017) and the research project Recyclad regarding the microstructure of DED HSS are summarized to set the background of the present Ph.D. thesis.

Starting with a general overview of DED HSS deposits, observations of the melt pool and heat-affected zone (HAZ) under light microscope reveal successive clad layers, with the last layer exhibiting a greater height compared to the lower layers. This height difference can be attributed to the remelting process that occurs during the production below the top layer. The laser power employed in the deposition process remelts the previous layers, resulting in a deep remelted zone. Figure 16a, shows the last layer melt pool and apparent melt pool height for previous layers. The thickness of the last layer provides a visual representation of this phenomenon. Additionally, lateral sagging and curvature of the edges or upper ends of the deposit are observed, which are consequences of the packing of the layers (Figure 16 a & b).

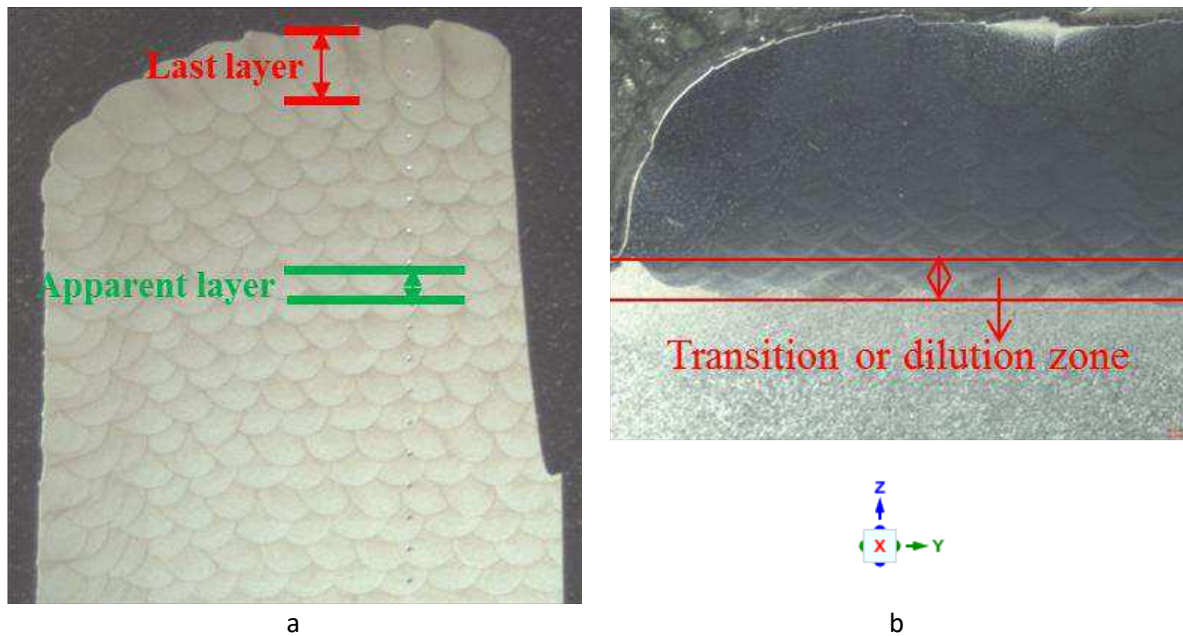


Figure 16 – a) deposit observed by binocular, b) deposit observed by optical microscope, showing the remelting effect of the substrate (transition or dilution zone) (Hashemi 2017).

In Figure 16 b, a remelted zone is observed above the arcaded lower border of the deposit, indicating the extent of remelting in the substrate. Within this zone, a mixture of substrate and deposit composition is observed, resulting in varying contrast levels ranging from clear (indicating almost pure substrate) to dark grey (representing pure deposit). This region is commonly referred to as the transition or dilution zone. Notably, a contrast difference is also observed between the lower contour and the core of each droplet (Figure 17). The lower contour corresponds to the Heat Affected Zone (HAZ), representing the preexisting material that has been affected by the heat flux without complete remelting. The HAZ is located beneath the completely remelted zone, and each droplet generates a corresponding HAZ along its U-shaped contour. Furthermore, the overlapping of droplets is observed both laterally in each apparent layer of the deposit and vertically between successive layers. This overlapping is a consequence of the chosen laser path to generate sound layers, without any voids and assuring a good cohesion between tracks and layers. For the bulk samples studied in this thesis, upon completing one layer, the laser does not return to the starting position but instead moves a certain distance along the Z direction (equivalent to the theoretical height of a single layer) and starts the next layer with a shift in the X direction, resulting in staggered droplets that lead to a quincunx-like arrangement for consecutive layers. (Figure 16 a).

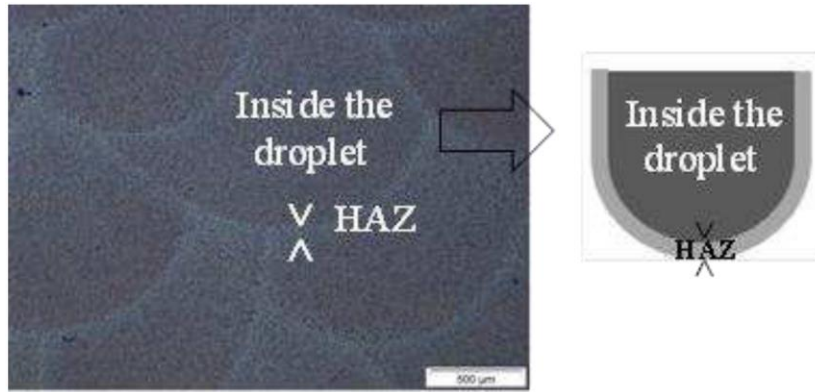


Figure 17 - Zoom on the microstructure observed by binocular, showing the HAZ (Hashemi 2017).

In (Hashemi 2017), two deposits were created on a cylindrical substrate of 42CrMo4 of 50 mm height and 100 mm diameter with the references LC B I300 and LC B S250. For LC B I300, the substrate was preheated to 300 °C in an oven and wrapped in an insulator and for LC B S250, the substrate was directly placed on a steel plate without any insulator, after a preheating of 250 °C within an oven. Figure 18 shows the manufactured deposits.



Figure 18 - Overview of DED deposits (Hashemi 2017).

In this section, we present a detailed examination of the microstructure of LC B S250 and LC B I300 deposits with a total height of 26 mm. The analysis is conducted on specimens in their as-built state and at three distinct depths. To facilitate the comparison, the left-hand images (Figure 19 a, c, and e) depict the microstructure of the LC B S250 deposit (sample P57) constructed with a steel plate, while the right-hand images (Figure 19 b, d, and f) illustrate the microstructure of the LC B I300 deposit (sample P58) constructed with an insulator.

At each depth, the microstructure primarily comprises lamellar eutectic M_2C carbides. These M_2C carbides exhibit a distinctive white contrast in BSE (backscattered electrons) images, indicative of the presence of heavy elements such as Mo and W (Lecomte-Beckers, 2005; Tchuindjang, 2011a). Notably, they form a quasi-continuous network along the grain boundaries (Lecomte-Beckers 2005, Luan 2010, Molinari 2002, Tchuindjang 2011, Tchuindjang 2011a). In proximity to the substrate, the eutectic M_2C carbides tend to appear grey due to the dilution of the HSS M4 powder with the 42CrMo4 substrate, resulting in a lower concentration of heavy alloying elements.

Furthermore, the M_2C carbides are found in association with V-rich MC carbides, which can adopt varying morphologies depending on the depth. At a depth of 0.5 mm from the free surface, primary MC carbides with angular and clover-shaped features are predominantly present. However, rod-like eutectic MC carbides are also observed in limited quantities at this depth (Figure 19 a and b). At mid-height, the LC B deposits predominantly exhibit angular primary MC carbides (Figure 19 c and d). In contrast, coral-shaped and rod-like eutectic MC carbides are primarily found at depths of 4.5 mm, 6.5 mm, and 8.5 mm from the free surface (Figure 20). Coexistence of primary and eutectic MC carbides is observed, with areas where eutectic MC carbides dominate (Figure 20 a). It is noteworthy that the coral-shaped and rod-like eutectic MC carbides exhibit a lighter appearance compared to the primary MC carbides, indicating a lower V content and formation at lower temperatures. This variation is attributed to differences in melt superheating conditions, where some areas allow the development of Vanadium carbides before δ ferrite formation, while others do not. In the latter case, the microstructure primarily comprises eutectic M_2C carbides, as well as coral-shaped and rod-like eutectic MC carbides (Figure 20 b). Additionally, the EBSD phase map of Figure 21 illustrates the distribution of Mo and W-rich M_2C carbides (yellow), V-rich MC carbides (violet), and the martensitic matrix (green) within deposit LC S300 (sample P76) (similar procedure to LC S250 but with a preheating of 300 °C).

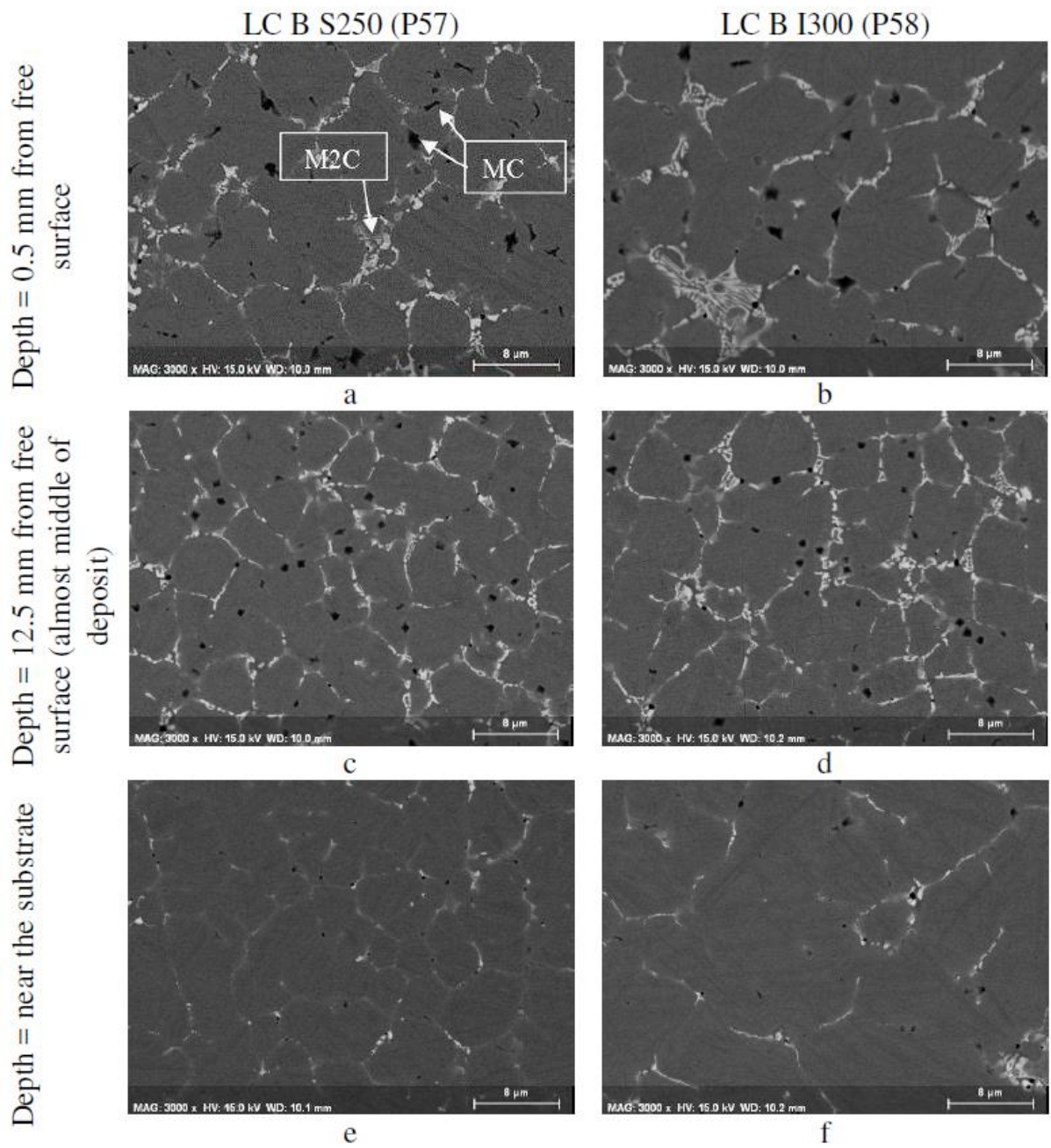
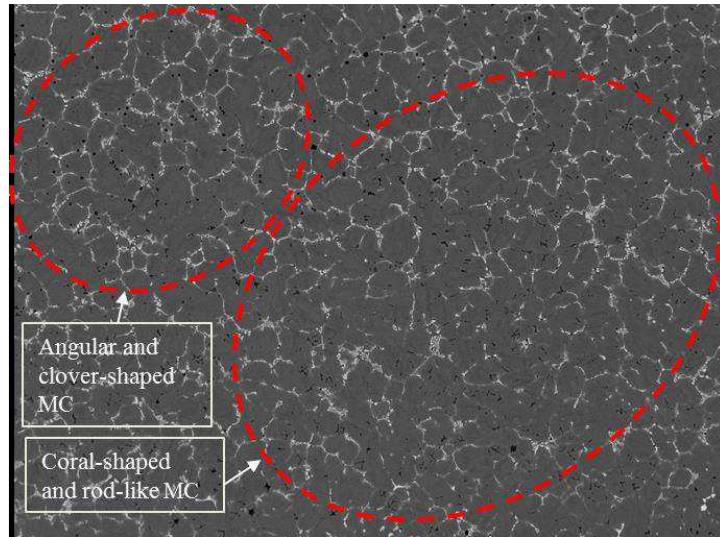
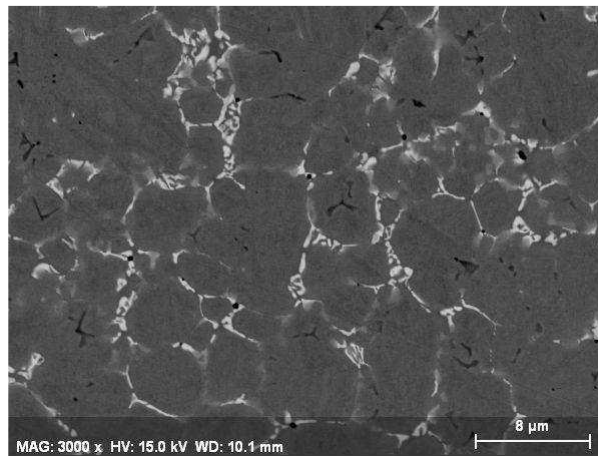


Figure 19 - SEM micrographs (BSE) showing the ultrafine microstructure of 2 LC B S250 (P57) and LC B I300 (P58) deposits, observed in 3 depths and in as-built state (Hashemi 2017).

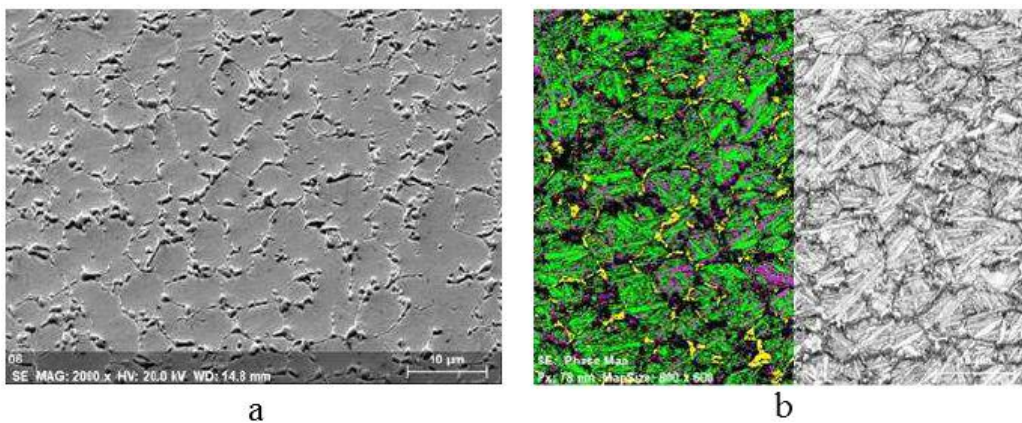


a



b

Figure 20 - SEM micrographs (BSE) showing the presence of coral-shaped and rod-like eutectic MC in the microstructure of LC B S250, a) 6.5 mm from the free surface, b) 4.5 mm from free surface (Hashemi 2017).



a

b

Figure 21 - a) Microstructure of LC B S300 deposit (sample P76), b) EBSD phase map of LC B S300 deposit in as-built state, showing distribution of Mo and W-rich M_2C (yellow), V-rich MC (violet) and martensitic matrix (green) (Hashemi 2017).

It is also worth noting that the morphology of the carbides is strongly affected by the melt superheating. The superheating is ascribed to the positive difference between the liquidus (beginning of the solidification) and the actual temperature reached by the melt. Indeed,

within the context of high melt superheating conditions, found thanks to thermal simulations of the DED process achieved within Article 1 in Chapter 2, the angular morphology of MC carbides is maintained throughout their development, owing to the continued presence of the surrounding liquid phase. Notably, it is observed that, at this depth, the proportion of carbides is comparatively higher than at the surface of the deposit. However, these carbides exhibit a finer, predominantly eutectic character.

Carbide types, morphology and volume fraction determines in turn the tribological behavior of the deposits. Indeed, Hashemi delved into a detailed comparison of three distinct DED materials, shedding light on the role the different carbide types in shaping the stability of the protective oxide tribo-layer, hence influencing their wear behaviors. When subjected to a low load of 10 N, the various carbides exhibited resilience against cracking even as sliding speeds escalated to 50 cm/s. Notably, angular primary MC carbides (Figure 22a), renowned for their exceptional hardness, remained anchored to the surface at the slower sliding speed due to geometric considerations. However, this changed at higher sliding speeds, as these angular carbides, along with oxides, were dislodged from the surface. The clover-shaped MC carbides (Figure 22b) demonstrated better resistance due to their superior anchoring properties. Similarly, the M_2C carbides (Figure 22 c and d), that are tightly integrated into the matrix and forming a continuous network, remained embedded even at 50 cm/s sliding speed.

Interestingly, the remarkably robust angular V-rich MC carbides (Figure 22e) showed a superior wear resistance compared with M_2C carbides (Figure 22 f and g) at lower sliding speeds (10 cm/s), possibly by protecting the samples from direct contact with the counterbody. However, this advantage waned at higher sliding speeds, suggesting a complex interplay between carbide properties and sliding conditions. Finally, variations in the wear behavior as a function of the height within the deposits were correlated with local variations of the exact type, morphology, and distribution of carbides present.

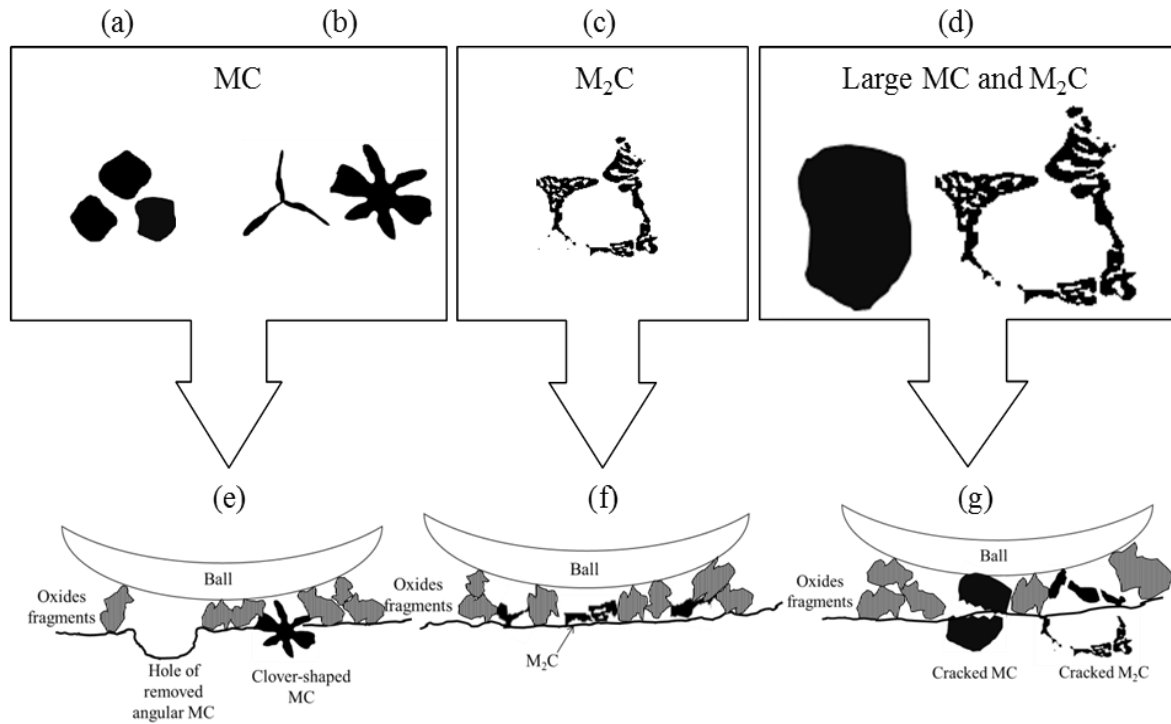


Figure 22 - Schematics of carbides and their behavior during wear tests at a sliding speed of 50 cm/s; a) angular black primary vanadium carbides; b) clover shape black primary V-rich carbides; c) W-rich eutectic M_2C carbides; d) large MC and M_2C carbides; e) oxides fragments act as a third body and angular MC carbides are disembedded from the track surface; f) oxides fragments act as a third body, and M_2C carbides remain embedded in the matrix and/or tribolayer, g) oxides fragments and cracked large MC and M_2C carbides act as a third body. (Hashemi 2017).

The major effect of local variation of microstructure as a function of the height within the deposit on the properties of DED HSS is further confirmed by considering hardness profiles. Hashemi did an assessment of the as-built state hardness profiles of two DED deposits, one with a steel plate underneath the substrate (LC B S250 – P57) and another with an insulator underneath (LC B I300 – P58), as depicted in Figure 23. The study reveals that the LC B deposit S250 with the steel plate exhibits higher hardness than the one with an insulator (LC B I300). This difference is attributed to the grain size, where finer grains in the LC B S250 lead to increased hardness. The hardness profile of the LC B S250 demonstrates a gradient, starting at around 700 HV at the upper part and increasing to about 800 HV near the substrate. In contrast, the LC B with an insulator shows a relatively flat hardness profile, starting at 700 HV, dropping to 600 HV, and then rising again above 700 HV closer to the substrate. Additionally, a specific point in the hardness curve, probably in the Heat-Affected Zone (HAZ) linked to the last deposited layer, reaches 800 HV. An observation which might be due to the presence of larger carbides rich in alloying elements in this zone. A general trend observed in both types of LC B deposits is an increase in hardness near the substrate, which is linked to the formation of martensite in the dilution zone.

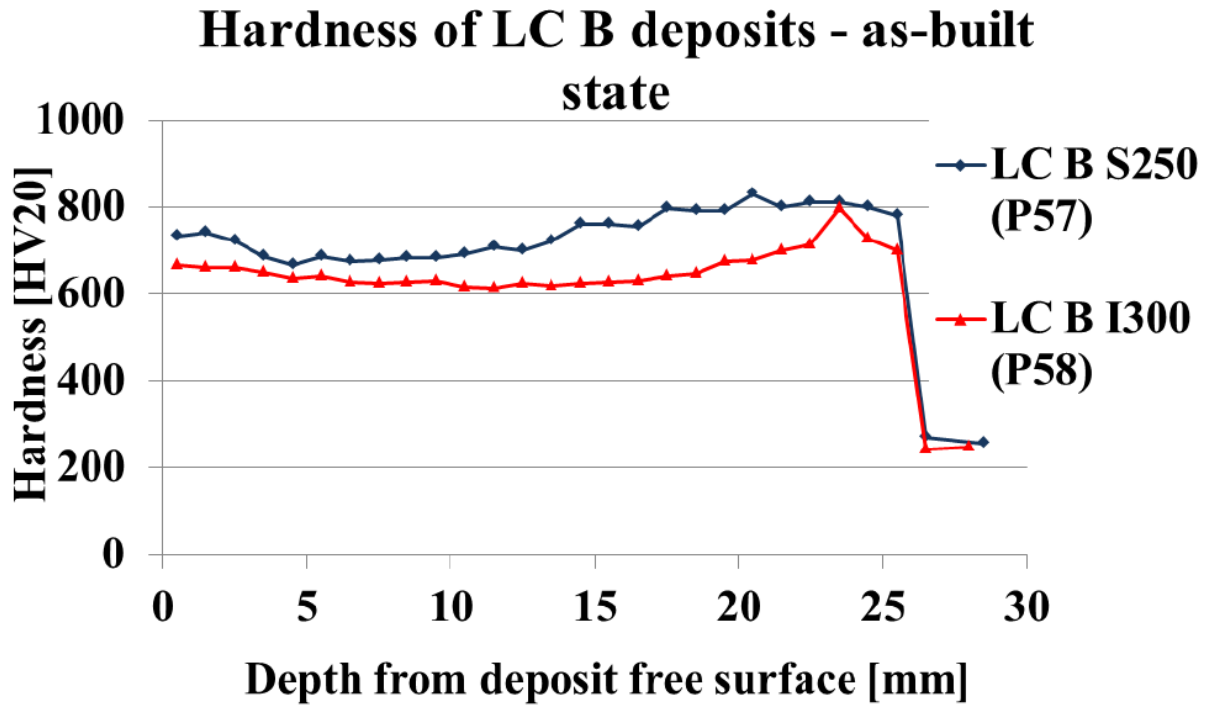


Figure 23 - Hardness of LC B S250 (P57) and LC B I300 (P58) deposits in as-built state. (Hashemi 2017).

1.5 Summary of Chapter 1

In the current PhD thesis, AM process is examined with an emphasis on the DED technique and the associated physical phenomena. This exploration includes an enumeration of potential defects inherent in the process, highlighting the necessity for a modeling tool designed to optimize parameters and mitigate these defects. A comprehensive review of various modeling techniques is presented, detailing the critical decisions required to effectively predict temperature fields, stresses, and microstructure. Additionally, the importance of selecting an appropriate simulation scale is underscored.

The state of the art also explores the complexity of the microstructure in HSS M4 samples produced via DED and its local variation as a consequence of local change in thermal history during fabrication. Moreover, this examination links the microstructural characteristics to the hardness and wear properties of the material, offering insights into the material's performance attributes.

A significant focus is placed on the development and refinement of a FEA model. This model is meticulously designed to accurately monitor the temperature field, thereby facilitating predictions about the microstructure. Detailed in Chapter 2, this model forms the foundation for subsequent optimizations, as presented in Chapter 4, aiming to achieve uniform hardness throughout the depth of the material.

1.6 References of Chapter 1

- Alimardani, M., Toyserkani, E., Huissoon, J.P., 2007a. A 3D dynamic numerical approach for temperature and thermal stress distributions in multilayer laser solid freeform fabrication process. *Opt. Lasers Eng.* 45, 1115–1130. <https://doi.org/10.1016/j.optlaseng.2007.06.010>
- Alimardani, M., Toyserkani, E., Huissoon, J.P., 2007b. Three-dimensional numerical approach for geometrical prediction of multilayer laser solid freeform fabrication process. *J. Laser Appl.* 19, 14–25. <https://doi.org/10.2351/1.2402518>
- Anca, A., Fachinotti, V.D., Escobar-Palafox, G., Cardona, A., 2011. Computational modelling of shaped metal deposition. *Int. J. Numer. Methods Eng.* 85, 84–106. <https://doi.org/10.1002/nme.2959>
- Armstrong, M., Mehrabi, H., and Naveed, N., An overview of modern metal additive manufacturing technology. *Journal of Manufacturing Processes*, 84 :1001–1029, Dec. 2022.
- Bayat, M., Dong, W., Thorborg, J., To, A.C., Hattel, J.H., 2021. A review of multi-scale and multi-physics simulations of metal additive manufacturing processes with focus on modeling strategies. *Addit. Manuf.* 47, 102278. <https://doi.org/10.1016/j.addma.2021.102278>
- Bayer, A.M., Becherer, B.A, Vasco, T., High-Speed Tool Steels, *ASM Handbook*, ASM International, 16 (1989) 51–59
- Biegler, M., Graf, B., Rethmeier, M., 2018a. In-situ distortions in LMD additive manufacturing walls can be measured with digital image correlation and predicted using numerical simulations. *Addit. Manuf.* 20, 101–110. <https://doi.org/10.1016/j.addma.2017.12.007>
- Biegler, M., Marko, A., Graf, B., Rethmeier, M., 2018b. Finite element analysis of in-situ distortion and bulging for an arbitrarily curved additive manufacturing directed energy deposition geometry. *Addit. Manuf.* 24, 264–272. <https://doi.org/10.1016/j.addma.2018.10.006>
- Biegler, M., Elsner, B.A.M., Graf, B., Rethmeier, M., 2020. Geometric distortion-compensation via transient numerical simulation for directed energy deposition additive manufacturing. *Sci. Technol. Weld. Join.* 25, 468–475. <https://doi.org/10.1080/13621718.2020.1743927>
- Blakey-Milner, B., Gradl, P., Snedden, G., Brooks, M., Pitot, J., Lopez, E., Leary, M., Berto, F., du Plessis, A.. Metal additive manufacturing in aerospace : A review. *Materials & Design*, 209 :110008, Nov. 2021
- Boccalini, M., Goldenstein, H., Solidification of high speed steels, *Int. Mater. Rev.* 46 (2001) 92–115
- Bobach, B.J. 2023 Towards unified formulation for the simulation of thermos-fluid-solid problems with phase change, Uliege PhD advisor J.P. Ponthot and V. Terrapon
- Crespo, A., Vilar, R., 2010, Finite element analysis of the rapid manufacturing of Ti – 6Al – 4V parts by laser powder deposition,” vol. 63, pp. 140–143
- Delahaye, J. ; Tchuindjang, J. Tchoufang ; Lecomte-Beckers, J. ; Rigo, O. ; Habraken, A.M. ; Mertens, A. Influence of Si precipitates on fracture mechanisms of AlSi10Mg parts processed by Selective Laser Melting *Acta Materialia*, 2019, 175, 160-170

- Denlinger, Erik R., Heigel, J.C., Michaleris, P., Palmer, T.A., 2015. Effect of inter-layer dwell time on distortion and residual stress in additive manufacturing of titanium and nickel alloys. *J. Mater. Process. Technol.* 215, 123–131. <https://doi.org/10.1016/j.jmatprotec.2014.07.030>
- Denlinger, E.R., Michaleris, P., 2016. Effect of stress relaxation on distortion in additive manufacturing process modeling. *Addit. Manuf.* 12, 51–59. <https://doi.org/10.1016/j.addma.2016.06.011>
- Dutta. B. Directed Energy Deposition (DED) Technology. In F. G. Caballero, *Encyclopedia of Materials : Metals and Alloys*, pages 66–84. Elsevier, Oxford, Jan. 2022.
- Esteva, E, Microstructure prediction of Ti6Al4V processed by Laser Cladding, Master thesis, Uliège 2018
- Fallah, V., Alimardani, M., Corbin, S.F., Khajepour, A., 2011. Temporal development of melt-pool morphology and clad geometry in laser powder deposition. *Comput. Mater. Sci.* 50, 2124–2134. <https://doi.org/10.1016/j.commatsci.2011.02.018>
- Fetni et al., Thermal model for the directed energy deposition of composite coatings of 316L stainless steel enriched with tungsten carbides, *Mater. Des.* (2021), 204:109661
- Gausemeier, N., Echterhoff, J., Kokoschka, M., Wall, M.. *Thinking ahead the Future of Additive Manufacturing – Analysis of Promising Industries*. University of Paderborn, Paderborn, Germany, heinz nixdorf institute ed. edition, 2011.
- Gibson, I., Rosen, D., Stucker, B.. *Directed Energy Deposition Processes*. In *Additive Manufacturing Technologies*, pages 245–268. Springer New York, New York, NY, 2015a.
- Gibson, I., Rosen, D., Stucker, B. (2015b) *Additive Manufacturing Technologies*, Springer New York, Heidelberg, Dordrecht London.
- Gockel J; Beuth J., Taminger K., Integrated control of solidification microstructure and melt pool dimensions electron beam wire feed additive manufacturing of Ti-6Al-4V, *Additive Manufacturing* 1–4 (2014) 119–126
- Goldak, J., Chakravarti, A., Bibby, M., 1984. A new finite element model for welding heat sources. *Metall. Trans. B* 15, 299–305. <https://doi.org/10.1007/BF02667333>
- Gradl P. R. and Protz C. S.. Technology advancements for channel wall nozzle manufacturing in liquid rocket engines. *Acta Astronautica*, 174 :148–158, Sept. 2020.
- Griffith, M.L., Schlienger, M.E., Harwell, L.D., Oliver, M.S., Baldwin, M.D., Ensz, M.T., Essien, M., Brooks, J., Robino, C.V., Smugeresky, J.E., Hofmeister, W.H., Wert, M.J., Nelson, D.V., 1999. Understanding thermal behavior in the LENS process, *Mater. Des.* 20, 107-113.
- Hashemi, N., 2017. Study of High Speed Steel deposits produced by Laser Cladding: Microstructure – Wear – Thermal Model (Ph.D. Thesis). University of Liège, advisors Anne Mertens, Anne Marie Habraken
- International Organization for Standardization. ISO/ASTM 52900 :2015.
- Hascoët, J.Y., Touzé, S., Rauch, M.. Automated identification of defect geometry for metallic part repair by an additive manufacturing process, *Welding in the world*, 62 (2018),62, 229-241

- Heigel, J.C., Michaleris, P., Reutzel, E.W., 2015. Thermo-mechanical model development and validation of directed energy deposition additive manufacturing of Ti-6Al-4V. *Addit. Manuf.* 5, 9–19. <https://doi.org/10.1016/j.addma.2014.10.003>
- Jamróz, W., Szafraniec, J., Kurek, M., and Jachowicz, R.. 3D Printing in Pharmaceutical and Medical Applications – Recent Achievements and Challenges. *Pharmaceutical Research*, 35(9):176, July 2018.
- Jardin, R.; Tchoundjang, J.; Duchene, L.; Tran, H. S.; Hashemi, N.; Carrus, R.; Mertens, A.; Habraken, A.. Thermal histories, and microstructures in Direct Energy Deposition of a High Speed Steel thick deposit. *Materials Letters*, 236, 42-45., (2019).
- Johnson, K.L., Rodgers, T.M., Underwood, O.D., Madison, J.D., Ford, K.R., Whetten, S.R., Dagel, D.J., Bishop, J.E., 2018. Simulation and experimental comparison of the thermo-mechanical history and 3D microstructure evolution of 304L stainless steel tubes manufactured using LENS. *Comput. Mech.* 61, 559–574. <https://doi.org/10.1007/s00466-017-1516-y>
- Ki H, Mohanty PS, Mazumder J. 2002, Multiple reflection and its influence on keyhole evolution, *Journal of Laser Applications*. 14: 39-45. DOI: 10.2351/1.1449885
- Labudovic, M., Hu, D., Kovacevic, R., 2003. A three dimensional model for direct laser metal powder deposition and rapid prototyping. *J. Mater. Sci.* 38, 35–49. <https://doi.org/10.1023/A:1021153513925>
- Lecomte-Beckers, J., Tchoufang Tchoundjang, J., Use of microscopy for identification of complex MC, M2C, M7C3, M6C and M23C6 carbides in high-speed steels, (2005) 3–4.
- Lévêque, R. *Aciers à outils - Composition chimique et structure*, Tech. l'Ingénieur, 33 (2013) 1–13.
- Leroy Dubief C. Contributions à la définition de règles de fabrication pour le procédé DED-LP par une approche thermique et géométrique, PhD thesis, UNIVERSITÉ DE BORDEAUX, advisor Pierre Joyot et Fabien Poulhaon 14 /04/2023
- Lewis, G.K., Schlienger, E., 2000, Practical considerations and capabilities for laser assisted direct metal deposition. *Mater. Des.*, 21,. 417–423.
- Lindgren, L.-E., Hedblom, E., 2001, Modelling of addition of filler material in large deformation analysis of multipass welding, *Communications in Numerical Methods in Engineering* 17, 647–657
- Liu, M.; Kuttolamadom, M., 2020. Nano-scale hardness and abrasion resistance of directed energy deposited co-cr-mo biomedical alloy. In *International Manufacturing Science and Engineering Conference*, volume 84256, page V001T05A022. American Society of Mechanical Engineers.
- Lu, X., Lin, X., Chiumenti, M., Cervera, M., Li, J., Ma, L., Wei, L., Hu, Y., Huang, W., 2018a. Finite element analysis and experimental validation of the thermomechanical behavior in laser solid forming of Ti-6Al-4V. *Addit. Manuf.* 21, 30–40. <https://doi.org/10.1016/j.addma.2018.02.003>
- Luan, Y., Song, N., Bai, Y., Kang, X., Li, D., Effect of solidification rate on the morphology and distribution of eutectic carbides in centrifugal casting high speed steel rolls, *J. Mater. Process. Technol.* 210 (2010) 536–541
- Lundbäck, A., Lindgren, L-E. 2011, Modelling of metal deposition, *Finite elements in analysis and design*, Vol.47 (10), p.1169-1177

- Madireddy, G., Li, C., Liu, J., Sealy, M.P., 2019. Modeling thermal and mechanical cancellation of residual stress from hybrid additive manufacturing by laser peening. *Nanotechnol. Precis. Eng.* 2, 49–60. <https://doi.org/10.1016/j.npe.2019.07.001>
- Mahamood, R. M., Shukla, M., Pityana, S.. Laser additive manufacturing in surface modification of metals. IGI Global, 2014.
- Manvatkar, V.D., Gokhale, A.A., Jagan Reddy, G., Venkataramana, A., De, A., 2011. Estimation of Melt Pool Dimensions, Thermal Cycle, and Hardness Distribution in the Laser-Engineered Net Shaping Process of Austenitic Stainless Steel. *Metall. Mater. Trans. A* 42, 4080–4087. <https://doi.org/10.1007/s11661-011-0787-8>
- Manvatkar, V., De, A., DebRoy, T., 2014. Heat transfer and material flow during laser assisted multi-layer additive manufacturing. *J. Appl. Phys.* 116, 124905. <https://doi.org/10.1063/1.4896751>
- Marion, G., 2016. Modélisation de procédés de fabrication additive de pièces aéronautiques et spatiales en Ti-6Al-4V par dépôt et fusion sélective d'un lit de poudre par laser : Approche thermique, métallurgique et mécanique (PhD thesis). Université Paris sciences et lettres, advisors Georges Cailletaud, Christophe Colin, Matthieu Mazière
- Michaleris, P., 2014. Modeling metal deposition in heat transfer analyses of additive manufacturing processes. *Finite Elem. Anal. Des.* 86, 51–60. <https://doi.org/10.1016/j.finel.2014.04.003>
- Miedzinski, M., 2017. Materials for additive manufacturing by direct energy deposition. Master's thesis, CHALMERS UNIVERSITY OF TECHNOLOGY Gothenburg, Sweden 2017
- Milewski, J.O., 2017. Additive Manufacturing of Metals: From Fundamental Technology to Rocket Nozzles, Medical Implants, and Custom Jewelry, Springer Series in Materials Science. Springer International Publishing. <https://doi.org/10.1007/978-3-319-58205-4>
- Molinari, A, Pellizzari, M., Biggi, A., Corbo, G., Tremea, A., Primary carbides in spincast HSS for Hot Rolls and their effect on the Oxidation Behaviour, in: J. Bergström Ed., Proc. 6th Int. Tool. Conf., Karlstad Universitet, Karlstad, 2002, pp. 365–377.
- Moridi A., Hassani-Gangaraj, S. M., Guagliano, M., Dao, M.. Cold spray coating: review of material systems and future perspectives. *Surface Engineering*, 30(6):369–395, 2014. Publisher: Taylor & Francis.
- Mukherjee, T., Zhang, W., DebRoy, T., 2017. An improved prediction of residual stresses and distortion in additive manufacturing. *Comput. Mater. Sci.* 126, 360–372. <https://doi.org/10.1016/j.commatsci.2016.10.003>
- Nain, V., 2022. Efficient thermomechanical modeling of large parts fabricated by Directed Energy Deposition Additive Manufacturing processes (PhD thesis). Université Bretagne Sud, advisor Muriel Carin and Thierry Engel.
- Neela, V., De, A., 2009. Three-dimensional heat transfer analysis of LENSTM process using finite element method. *Int. J. Adv. Manuf. Technol.* 45, 935–943. doi:10.1007/s00170-009-2024-9
- Okane, T., Umeda, T., Interface temperature measurement of M2C and M6C eutectic carbides in the Fe - Mo - C system, *Sci. Technol. Adv. Mater.* 2 (2001) 247–251
- Pan, F., Hirohashi, M., Lu, Y., Ding, P., Tang, A., Edmonds, D. V., Carbides in highspeed steels containing silicon, *Metall. Mater. Trans. A.* 35A (2004) 2757–2766

- Paydas, H., Mertens, A. Carrus, R., Lecomte-Beckers, J., Tchoufang Tchuindjang, J., 2015, Laser cladding as repair technology for Ti-6Al-4V alloy: Influence of building strategy on microstructure and hardness, *Mater. Des.*, vol. 85, pp. 497– 510
- Peyre, P., Dal, M., POUZET, Sebastien, Castelnau, O., 2017. Simplified numerical model for the laser metal deposition additive manufacturing process. *J. Laser Appl.* 29, Article number 022304. <https://doi.org/10.2351/1.4983251>
- Pham, T.Q.D., Hoang, T. V., Van Tran, X., Tuan Pham, Q., Fetni, S., Duchene, L., Tran, H. S., & Habraken, A. (2022 a). Fast and accurate prediction of temperature evolutions in additive manufacturing process using deep learning. *Journal of Intelligent Manufacturing*. doi:10.1007/s10845-021-01896-8
- Pham, T. Q. D., Hoang, T. V., Tran, X. V., Fetni, S., Duchene, L., Tran, H. S., Habraken, A. (2022 b). Characterization, propagation, and sensitivity analysis of uncertainties in the directed energy deposition process using a deep learning-based surrogate model. *Probabilistic Engineering Mechanics*, 69, 103297. doi:10.1016/j.probenmech.2022.103297 <https://hdl.handle.net/2268/293435>
- Pham T.Q.D., Hoang T.V., Tran X.V., Fetni S., Duchêne L., Tran H.S., Habraken A.M. (2023) A framework for the robust optimization under uncertainty in additive manufacturing, *Journal of Manufacturing Processes* DOI:10.1016/j.jmapro.2023.08.009
- Pinkerton, A.J., Wang, W., Li, L. Component repair using laser direct metal deposition. *Proceeding of the Institution of Mechanical Engineers Part B Journal of Engineering Manufacture*, 2008, 827-836
- Piscopo, G., Atzeni, E., Salmi, A., 2019. A Hybrid Modeling of the Physics-Driven Evolution of Material Addition and Track Generation in Laser Powder Directed Energy Deposition. *Materials* 12, 2819. <https://doi.org/10.3390/ma12172819>
- Qi, H., Mazumder, J., Ki, H.; Numerical simulation of heat transfer and fluid flow in coaxial laser cladding process for direct metal deposition. *J. Appl. Phys.* 15 July 2006; 100 (2): 024903. <https://doi.org/10.1063/1.2209807>
- Saracibar, C., Lundbäck, A., Chiumenti, M., Cervera, M., (2014). Shaped Metal Deposition Processes. https://doi.org/10.1007/978-94-007-2739-7_808
- Setien, Iñaki; Chiumenti, Michele; van Der Veen, Sjoerd; San Sebastian, Maria; Garciandía, Fermín; Echeverría, Alberto Empirical methodology to determine inherent strains in additive manufacturing *Computers and Mathematics with Applications* in Press June 2018.
- SmarTech. SmarTech Analysis Annual Additive Manufacturing Market Summary Report Says AM Market Grew to Over \$10B Worldwide in 2019, Aug. 2020.
- Tchuindjang, J., Lecomte-Beckers, J., Study of the origin of the unexpected pearlite during the cooling stage of two cast high-speed steels, *Solid State Phenomena* 172-174 (2011a) 803–808.
- Tchuindjang, J., Sinnaeve, M., Lecomte-Beckers, J., Influence of high temperature heat treatment on in-situ transformation of Mo-rich eutectic carbides in HSS and semi-HSS grades; in: J. Lecomte-Beckers, J. T. Tchuindjang (Eds.), *Proceedings of Abrasion 2011b*, Liège, 2011a, pp. 61–75.
- Tchuindjang J., Torres, I., Flores, P., Habraken, A. M., Lecomte-Beckers, J., Phase transformations and crack initiation in a high-chromium cast steel under hot compression tests, *J. Mater. Eng. Perform.* 24 (2015) 2025–2041.

Tematio, J., 2022. Simulation numérique du procédé de fabrication additive DED : résolution thermomécanique incrémentale complète et modèles réduits de type "inherent strain" (PhD Thesis). PSL University, advisors Michel Bellet, Yancheng Zhang

Toyserkani, E.; Khajepour, A.; Corbin, S.F. Laser Cladding; CRC Press: Boca Raton, FL, USA, 2004.

Tran, H., Tchuindjang, J.T., Paydas, H., Mertens, A., Jardin, R.T., Duchêne, L., Carrus, R., Lecomte-Beckers, J., Habraken, A.M., 2017. 3D thermal finite element analysis of laser cladding processed Ti-6Al-4V part with microstructural correlations. *Mater. Des.* 128, 130–142. doi:10.1016/j.matdes.2017.04.092

Yukio Ueda, Keiji Fukuda, Keiji Nakacho, and Setsuo Endo. A new measuring method of residual stresses with the aid of finite element method and reliability of estimated values. *Journal of the Society of Naval Architects of Japan*, 1975(138) :499–507, 1975.

Wang, Jintao & Liu, Shouping & Fang, Yunpeng & He, Zhongrui. (2020). A short review on selective laser melting of H13 steel. *The International Journal of Advanced Manufacturing Technology*. 108. 10.1007/s00170-020-05584-4.

Wang, L., Felicelli, S., 2006. Analysis of thermal phenomena in LENSTM deposition. *Mater. Sci. Eng. A* 435–436, 625–631. <https://doi.org/10.1016/j.msea.2006.07.087>

Wang, L., Felicelli, S., Gooroochurn, Y., Wang, P.T., Horstemeyer, M.F., 2008. Optimization of the LENS[®] process for steady molten pool size. *Mater. Sci. Eng. A* 474, 148–156. doi:10.1016/j.msea.2007.04.119

Wang, Yujie, Mao, Bo, Chu, Shuangjie, Chen, Sai, Xing, Hui, Zhao, Haiyan, Wang, Shuyang, Wang, Yuqian, Zhang, Jiao, Sun, Baode. (2023). Advanced manufacturing of high-speed steels: A critical review of the process design, microstructural evolution, and engineering performance. *Journal of Materials Research and Technology*. 24, 8198-8240, doi:10.1016/j.jmrt.2023.04.269

Weber, C. Pena, V., Micali, M., Yglesias, E., Rood, S., Scott, J., Lal, B.. The Role of the National Science Foundation in the Origin and Evolution of Additive Manufacturing in the United States, Nov. 2013

Wei, H.L., Mazumder, J., DebRoy, T., 2015. Evolution of solidification texture during additive manufacturing. *Sci. Rep.* 5, 16446. <https://doi.org/10.1038/srep16446>

Xie, R., Chen, G., Zhao, Y., Zhang, S., Yan, W., Lin, X., Shi, Q., 2019. In-situ observation and numerical simulation on the transient strain and distortion prediction during additive manufacturing. *J. Manuf. Process.* 38, 494–501. <https://doi.org/10.1016/j.jmapro.2019.01.049>

Xie, R., Shi, Q., Chen, G., 2020a. Improved distortion prediction in additive manufacturing using an experimental-based stress relaxation model. *J. Mater. Sci. Technol.* 59, 83–91. <https://doi.org/10.1016/j.jmst.2020.04.056>

Yang, J., Sun, S., Brandt, M., Yan W., *J. Mater. Process. Technol.* 210-15 (2010) 2215

Yang, Q., Zhang, P., Cheng, L., Min, Z., Chyu, M., To, A.C., 2016. Finite element modeling and validation of thermomechanical behavior of Ti-6Al-4V in directed energy deposition additive manufacturing. *Addit. Manuf., Special Issue on Modeling & Simulation for Additive Manufacturing* 12, 169–177. <https://doi.org/10.1016/j.addma.2016.06.012>

Chapter 2

This article¹ represents the MSM group's initial venture into modeling the metal additive manufacturing process. We constructed a 2D model to simulate a 36-layer bulk deposit of M4 HSS (sample P76). To build this model, we relied on specific properties like thermal conductivity, density, and heat capacity, all of which were measured from the deposit and substrate under variable temperature conditions.

In order to ensure the accuracy of our thermal model, we strategically placed thermocouples in the substrate at 4 locations. The complementary information of these measurements helped us to increase the accuracy of the target thermal experimental curve. However only those temperature histories cannot yield a single set of parameters. The measured melt pool size of the last layer is also needed to confirm the identified set of parameters. This point was better quantified and demonstrated by C. Galo for the sample P76 (Gallo 2024)², but the issue was already observed in our work. The predictions generated by our model closely aligned with the actual thermal histories and melt pool size observed in experiments.

To achieve this level of accuracy, we had to determine the coefficients for emissivity and convection. Interestingly, we found that the emissivity coefficient was 1, though its physical significance remained somewhat unclear. This might be attributed to the simplification of our model through a 2D approach. Nevertheless, studying the thermal histories provided valuable insights into the non-uniform microstructure observed at varying depths within the sample.

Reference samples were processed to validate both the models and the microstructure at macro, micro, and nano scales, while successfully predicting thermal histories, a pivotal step detailed in Chapter 3, enabled progress toward the development of a more detailed 3D thermomechanical model and the optimization of microstructures as elaborated in Chapter 4.

¹ Published in Materials Letters, Volume 236, 2019, pp.42-45

² Impact of boundary parameters accuracy on modeling of directed energy deposition thermal field, Calogero Gallo, Laurent Duchene, Thinh Quy Duc Pham, Ruben Jardin, Victor Tuninetti, Anne-Marie Habraken, Metals 2024

Thermal histories and microstructures in Direct Energy Deposition of a High Speed Steel thick deposit

R. T. Jardin², J. Tchoufang Tchouindjang¹, L. Duchêne¹, H.-S. Tran¹, N. Hashemi¹, R. Carrus², A. Mertens¹, A.M. Habraken^{1*}

¹University of Liège, Quartier Polytech 1, Allée de la Découverte 9 (B52), B4000 Liège, Belgium

²Sirris Research Centre (Liège), Rue Bois St-Jean, 12, B 4102 Seraing, Belgium

Abstract

The results of 2D Finite Element thermal simulations of Direct Energy Deposition of a High Speed Steel thick deposit explain the observed microstructural heterogeneities over the whole height of a 36-layer deposit. The Finite Element model is validated by the recorded substrate temperature and the melt pool depth of the last clad layer experimentally measured. The correlation between the computed thermal fields and the microstructures of three points of interest located at different depths within the deposit is carried out. The effect of both the melt superheating temperature and the thermal cyclic history on the carbides' type, shape, and size is discussed.

Keywords: Finite element analysis, Laser deposition, Powder processing, Solidification microstructure, Carbide

Introduction

High Speed Steels (HSS) are widely used in various applications including cutting operations, high speed machining, hot stamping, molding, and hot strip mills. They withstand severe mechanical and physico-chemical stresses in service, thanks to their alloy design and to their carefully tailored microstructure. These alloys belong to the complex Fe-Cr-C-X system, where X is a strong carbide-forming element such as V, Nb, Mo, or W [1].

DED (Direct Energy Deposition) is an additive manufacturing technique where a powder is projected on the substrate and melted while passing through a laser beam. Very high cooling rates ranging from 10^3 to 10^7 °C/s are achieved and yield ultrafine microstructures. Advantages such as the reduction of thermal distortions, porosity, cost and machining time as well as the possibility of manufacturing material gradients through powder of different chemical compositions are the specificities of DED [2].

High temperature gradients are generated during DED leading to directional microstructures. To understand their genesis, the thermal fields predicted by Finite Element (FE) analyses often complement experiments. Yang et al. [3] studied the heat affected zone while Wang et al. [4] analyzed the melt pool. Kong et al. [5] investigated the effect of different processing parameters on the deposit height while Tran et al. [6] focused on the evolution of the

* Corresponding author,
E-mail address: anne.habraken@uliege.be (A.M. Habraken)

microstructure in the deposit. However, works focusing on the solidification of thick HSS deposits processed by DED are innovative. Heat tends to accumulate in such thick deposits due to the laser power of 1 to 2 kW, leading to microstructural heterogeneities within the deposit height [7].

Materials and Method

The DED equipment of Sirris Research Centre (5-axis Irepa Laser Cladding & Nd-YAG laser operating continuously, maximum power 2kW) was used to manufacture the sample (40 x 40 x 27.5 mm³). The raw material consisted of the commercial HSS M4 powder with a chemical composition of (in wt%) 1.35 C, 4.30 Cr, 4.64 Mo, 4.10 V, 5.60 W, 0.34 Mn, 0.9 Ni, 0.33 Si, and balance Fe. The particle size ranged from 50 to 150 μm. The laser power, nozzle scanning speed, powder feed rate, and the pre-heating temperature of the 42CrMo4 substrate (40mm height, 100mm diameter) were fixed at 1100W, 6.87 mm/s, 76mg/s, 300°C, respectively. Four thermocouples were located at the four cardinal points within the substrate, 5 mm below the surface, and at 20 mm from the edge.

Using conduction-convection-radiation exchanges, the thermal field was computed by the FE code Lagamine from the University of Liège. The details of these simulations applied to DED can be found in [6]. In the present case of 36 layers, 2D simulations were preferred to save computational time. A planar mesh with an element height of 0.764 mm within the deposit and coarser elements within the substrate was designed. It simulates a vertical cut in the middle of the deposit, parallel to the laser displacement. Within the deposit, the element width of 0.75 mm corresponds to half of the laser spot diameter. Based on the experimental laser beam velocity, the element birth technique models the heat source movement and the addition of material. The ambient temperature is assumed constant at 298 K.

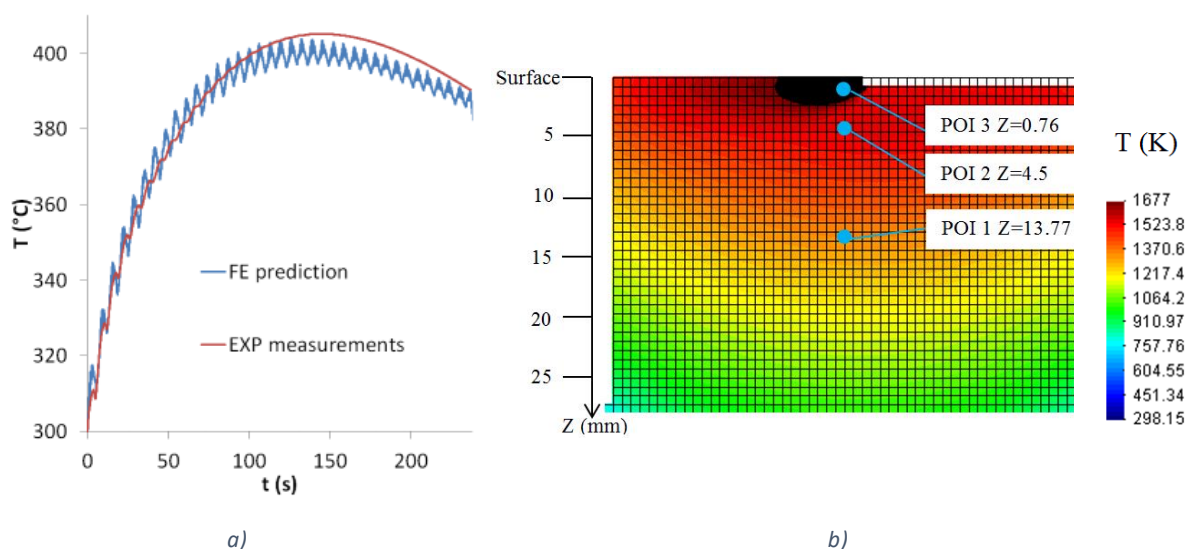


Fig. 1 a) Computed and experimental curves of temperature versus time at one thermocouple; b) FE thermal field during the last layer deposition (temperature higher than liquidus in black color) and location of points of interest (POI) within the thick deposit.

The thermal conductivity, the density, and the specific heat capacity were measured for samples extracted from the deposit and the substrate [8]. The radiation emissivity factor was set to 1 and a convection coefficient of $230\text{W/m}^2\text{K}$ was applied. The liquidus and solidus temperatures used in the model, 1677K , and 1503K respectively, were obtained from thermodynamical simulation. Laser heat flux was fitted in the 2D model to obtain the range of substrate temperature experimentally measured. This inverse approach provides reliable results as already shown by [9].

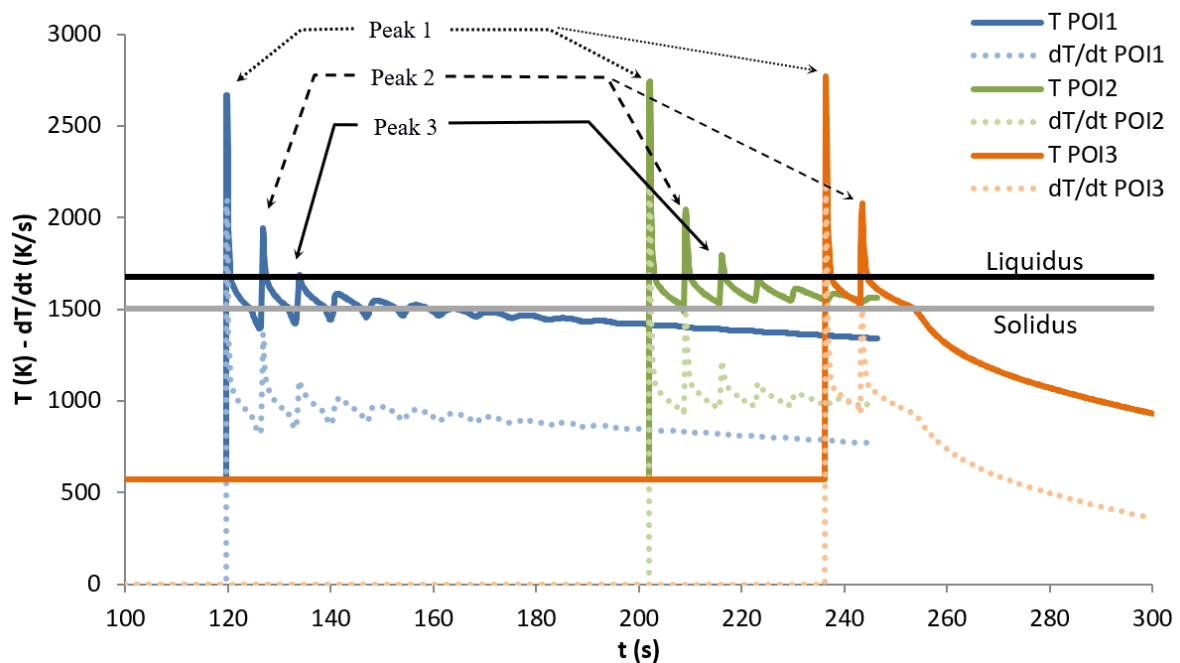


Fig. 2: Predicted curves showing the thermal histories (full lines) and temperature rate (dashed lines) within the three POIs.

Result and discussion

Fig. 1a compares the measured and predicted temperature histories in the substrate, at one thermocouple. In addition, the 2D FE simulation (Fig. 1b) predicted the melt pool depth of the last clad layer: 2.3 mm , similar to the experimental one (2.4 mm). As discussed on a DED Ti-based alloy [6], due to high heating rates, an upward shift of the solidus was observed, toward the liquidus. Fig. 2 gathers the predicted temperature histories for the three points of interest POI1, POI2, and POI3, which are located in the central part of the clad at different depths from the free surface (Fig. 1b). Key results for POIs are provided in Table 1. The cooling rate achieved during solidification (column 4) seems to be similar for all the POIs, regardless of the initial superheating temperature. Therefore assuming a similar initial cell size for all the POIs is reasonable. However, due to the occurrence of partial melting especially for POI1 and POI2, their related cell size is reduced as explained hereafter.

Table 1: Key predicted temperatures associated with the different depths.

Depth from top surface (mm)	Peak number	Average cooling rate between peak max and min temperature (K/s)	Cooling rate between liquidus and solidus (K/s)	Max. predicted super heating temperature T of the melt pool (K)
13.77 POI1	2nd	1148	1025	1941
	3rd	1019	1019	1687*
4.5 POI2	3rd	1096	1045	1794*
	4th	1035	–	1668
0.76 POI3	1st	1563	1026	2768
	2nd	1216	1022	2075*

* last melting of the POI

As shown in Fig. 3, the microstructure is made of cells (martensite with few retained austenite) surrounded by a quasi-continuous network of intercellular carbides [10].

Based on Fig. 2, it can be assumed that both POI1 and POI2 are fully melted three times prior to the last solidification, whereas POI3 is melted twice. Each complete melting step corresponds to reheating above the liquidus (1677 K). In addition, subsequent partial melting steps also occur for both POI1 and POI2, because of the numerous peaks having their maximum ranging between the solidus and the liquidus. This maximum temperature within solidification range follows a decreasing trend (Fig. 2). For POI1, the partial melting steps start around the middle of the solidification range before quickly decreasing below the solidus. For POI2, the partial melting steps are more pronounced over time and present a higher average temperature compared to POI1. Such a partial melting step of the cells is related to the dendritic fragmentation phenomenon [11]. Amin-Ahmadi's work [13] already linked this phenomenon to DED when fragmentation of dendrites appears due to applied stress created by melt flow which decreases the melting point of dendrite.

For POI1, it can be assumed that only M_2C eutectics are melted while keeping the intercellular MC unmelted or only partially melted, due to their high melting point [14]. For POI2, the more pronounced melting phenomenon generates smaller cells containing intracellular coral-shaped MC carbides. This observation can be related to back diffusion of carbides forming element within the unmelted cells in the semi-solid regime (Fig. 3b). It explains why very few intercellular MC are present in POI2, whereas intracellular MC precipitated together with the first solid under a coupled growth process. POI3 exhibits a microstructure similar to POI1. However, the size of both cells and intercellular MC carbides is higher in POI3 than in POI1 (Fig. 3a and c), confirming the refining process achieved with partial melting steps (Fig. 2).

The relative chemical composition could be obtained from BSE mode. The darkest MC carbides found within intercellular zones on both POI1 and POI3 are close to "pure" VC whereas the brightest ones present in POI2 contain other transition elements heavier than V, such as W,

Mo, Nb (Fig. 3). This result is in good agreement with the previous assumption of a longer residence time within the semi-solid state for POI2. This period allows a near partition equilibrium for many elements including V which diffuse back into the unmelted cells after being dissolved from the MC. The M_2C intercellular carbides present in each POI appear white as they contain heavy elements such as Mo and W.

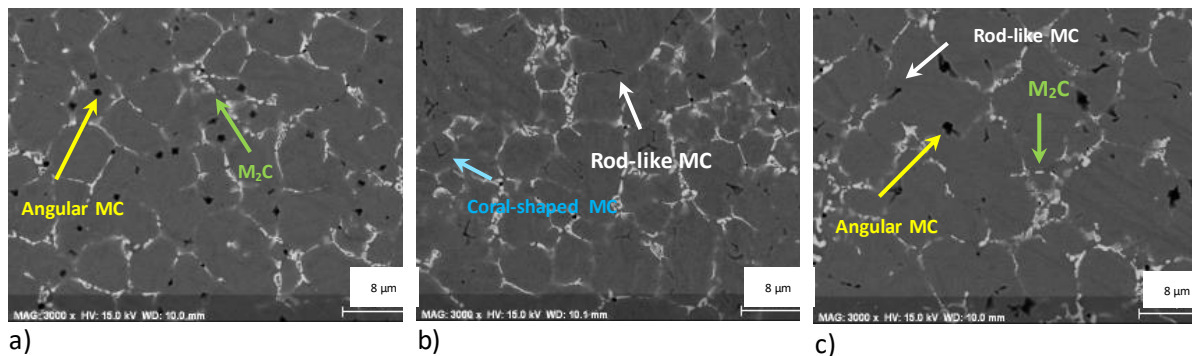


Fig. 3: SEM-BSE micrographs of a) POI1 with star-like MC and lamellar eutectic M_2C intercellular carbides; b) POI2 with coral-shaped intracellular MC, intercellular eutectic M_2C , and refined cells due to multiple melting; c) POI3 with coarse angular MC and eutectic M_2C within intercellular zones.

Conclusions

The FE thermal field computed for DED of HSS M4 thick deposit explains the microstructure genesis. The scientific novelties are summed up as follows:

- Close to the deposit free surface, as well as at mid-height, the angular-like MC carbides precipitated in intercellular zones just after the primary cells under high superheating temperature of the melt pool. The increased superheating within the melt pool at mid-height of the deposit promotes the coarsening of the solidification phases including cells and intercellular carbides.
- At intermediate depth from the deposit free surface, a lower superheating temperature and a higher number of re-melting of the material points promote the precipitation of coral-like MC carbides inside cells. They are formed together with the first solid (matrix) under a coupled growth process.
- For all the locations within the thick deposit, the end of the solidification is similar, leading to the precipitation of eutectic M_2C carbides.

Acknowledgments

This work was supported by Walloon Region [RW 11-1-7335 Recyclad], FNRS F.R.S. [PDR T.0039.14 and position of AM Habraken], FEDER [IAWATHA], CAREM ULiège.

References

- [1] M. Boccalini, H. Goldenstein, *Int. Mater. Rev.* 46 (2001) 92.
- [2] E. Toyserkani, A. Khajepour, S. Corbin, *Laser Cladding*, CRC Press LLC, Boca Raton, 2005.
- [3] J. Yang, S. Sun, M. Brandt, W. Yan, *J. Mater. Process. Technol.* 210-15 (2010) 2215.

- [4] L. Wang, S. Felicelli, Y. Gooroochurn, P.T. Wang, M.F. Horstemeyer, *Mater. Sci. Eng. A*, 474-1 (2008).
- [5] F. Kong, R. Kovacevic, *Metall. Mater. Trans. B*, 41 (2010) 1310.
- [6] H. Tran, J.T. Tchuindjang, H. Paydas, A. Mertens, R.T. Jardin, L. Duchêne, R. Carrus, A.M. Habraken, *Mater. Des.* 128 (2017) 130.
- [7] G.P. Dinda, A.K. Dasgupta, J. Mazumder, *Surf. Coat. Technol.* 206 (2012) 2152.
- [8] N. Hashemi, PhD thesis ULiège, 2017 <https://orbi.uliege.be/handle/2268/214330>
- [9] H. Yin, S.D. Felicelli, L. Wang, *J. Heat Transfer*, 130-10 (2008) 102101.
- [10] N. Hashemi, A. Mertens, H. Montrieux, J.T. Tchuindjang, O. Dedry, R. Carrus, J. Lecomte-Beckers, *Surf. Coat. Technol.* 315 (2017) 519.
- [11] P. Grgac, M. Liptak, M. Behulova, L. Caplovic, H. G. Lindenkreuz, W. Löser *Mater. Sci. Eng.*, 449 (2007) 658.
- [12] J. Valloton, D. M. Herlach, H. Henein, D. Sediako *Metall. Mater. Trans. A*, 48(10), (2017) 4735.
- [13] Amin-Ahmadi, B., & Aashuri, H. J. *Mater. Process. Technol.*, 210-12 (2010) 1632.
- [14] Aisman, D., Rubesova, K., & Masek, B. *IOP Conf. Series Mater. Sci. Eng.*118-1 (2016)

Chapter 3

This article³ builds upon the insights gained from the previously developed thermal model (Chapter 2). Here, we explore the intricacies of manufacturing a 10-layer thin-wall sample of HSS M4 (sample P42C). During the manufacturing process, one end of the substrate was clamped while the other end was left partially free (horizontal dilatation allowed but not vertical one), allowing us to monitor the sample's vertical displacement at its middle. To capture the thermal history accurately, we strategically placed thermocouples in the substrate at key positions. Subsequently, we conducted a thorough analysis of the sample, employing scanning electron microscopy and optical microscopy for detailed metallographic observations.

A comprehensive 3D thermomechanical model was developed for this study relying on measured properties from a bulk sample made with DED (sample P137). Notably, the measured properties exhibited significant deviations from existing literature values generally measured on cast or forged samples. Additionally, we performed rapid quenching at a cooling rate of 200 °C/s to determine a coefficient of thermal expansion closer to the process one (even if still far from real process cooling rate). The test result demonstrated notable differences compared to measurements obtained under slower cooling conditions.

To identify the material's behavior during the process, we conducted a series of compression tests on samples extracted from a bulk DED sample at various temperatures, including room temperature, 300 °C, 500 °C, and 950 °C. We also explored different strain rates, although within the analyzed range, the strain rate did not appear to significantly impact the stress-strain behavior (see Annex – Compression test report).

The thermal model validity was successfully confirmed through comparisons with thermal histories recorded by the thermocouples, and correlations with the observed microstructure. The difficulties we have had to validate the simulation results within the pre heating stage have been solved, enhancing again the differences in thermophysical properties associated to a microstructure. The substrate properties in the simulations first relied on previous tests performed on 42CrMo4 grade in Bainitic-Martensitic state for the substrate used for bulk samples of previous chapter. However a closer look at the material certificate identified a pearlitic state of the 42CrMo4 grade used as substrate in the studied thin walls. This was confirmed by measurements on our substrate, used to validate our thermal predictions within the pre heating stage (see Numiform proceeding article Jardin 2019). This modification was a key point to be able by simulations to recover thermal fields measured in multiple points during substrate pre-heating, showing the high sensitivity to thermo-physical properties. To enhance our understanding of the predicted thermal fields, we conducted a sensitivity analysis, exploring the effects of various thermophysical parameters on the thermal history in the article presented hereafter.

Furthermore, the deformation prediction accuracy was investigated by comparisons between the model result with the measured vertical displacement at the center of the sample, during

³ Published in Metals, volume 10, 2020, 1554

both manufacturing and cooling phases. These validation steps posed notable challenges, underscoring the importance of precise measurements of the coefficient of thermal expansion under the specific thermal gradients studied. Additionally, a sensitivity analysis was conducted for the Young modulus and the yield stress to further explore the capabilities of the model. The discrepancies between the simulation and the experiment could not be decreased due to too multiple uncertainties. The current PhD was at its end when a deep learning approach has been initiated in addition to complementary material characterizations to improve the FE model with new colleagues, however it did not succeed due to lack of funding.

Sensitivity analysis in the modelling of a high speed steel thin-wall produced by directed energy deposition

Rúben Tome Jardin ¹, Víctor Tuninetti ^{2,*}, Jérôme Tchuindjang ³, Neda Hashemi ³, Raoul Carrus ⁴, Anne Mertens ³, Laurent Duchêne ¹, Hoang Son Tran ¹, Anne Marie Habraken ^{1,5,*}

¹ Department ArGENCo-MSM, University of Liège, Quartier Polytech 1, allée de la Découverte 9, 4000 Liège, Belgium; ra.tjardin@ulg.ac.be

² Department of Mechanical Engineering, Universidad de La Frontera, Francisco Salazar 01145, 4780000 Temuco, Chile; victor.tuninetti@ufrontera.cl

³ Department A&M–MMS, University of Liège, Quartier Polytech 1, allée de la Découverte 9, 4000 Liège, Belgium; anne.mertens@uliege.be

⁴ Sirris Research Centre (Liège), Rue Bois St-Jean 12, 4102 Seraing, Belgium; raoul.Carrus@sirris.be

⁵ Fonds de la Recherche Scientifique – F.R.S. - F.N.R.S., 1000 Brussels, Belgium; anne.habraken@uliege.be

* Correspondence: victor.tuninetti@ufrontera.cl; Tel.: + 56452325984 (V.T.), anne.habraken@uliege.be, Tel. : +32496607945 (A.M.H.)

Received: date; Accepted: date; Published: date

Abstract: This paper reports the sensitivity of the thermal and the displacement histories predicted by a finite element analysis to material properties and boundary conditions of a directed energy deposition of a M4 high speed steel thin wall part additively manufactured on a 42CrMo4 steel substrate. The model accuracy is assessed by comparing the simulation results with the experimental measurements such as evolving local temperatures and distortion of the substrate. The numerical results of thermal history are successfully correlated with the solidified microstructures measured by scanning electron microscope technique, explaining the non-uniform cellular type grains depending on the deposit layers. Laser power, thermal conductivity and thermal capacity of deposit and substrate are considered in the sensitivity analysis in order to quantify the effect of their variations on the local thermal history, while Young's modulus and yield stress variation effects are evaluated on the distortion response of the sample. The laser power showed the highest impact on the thermal history, then comes the thermal capacity, then the conductivity. Considering distortion, variations of the Young's modulus have a higher impact than the yield stress.

Keywords: DED additive process; thin wall deposit experiment; distortion; thermal history; finite element simulation; thermomechanical model; M4 steel

1. Introduction

Within the additive manufacturing (AM) processes, Directed Energy Deposition (DED) is a generic name for layered manufacturing of fully dense parts based on progressive welding of a wire or metal powder (Figure 1) on a substrate. The energy sources required for melting the feed metal in DED processes can be provided by electron beam (EB), laser (L), plasma or electric arc. The most known DED processes are Laser cladding (LC) or Laser metal deposition

(LMD) such as wire-based laser metal deposition (LMD-W) or powder-based laser metal deposition (LMD-P); electron beam melting (EBM) powder or wire-based; plasma transferred arc (PTA) deposition; and wire arc additive manufacturing (WAAM) processes such as gas tungsten arc welding (GTAW) or gas metal arc welding (GMAW).

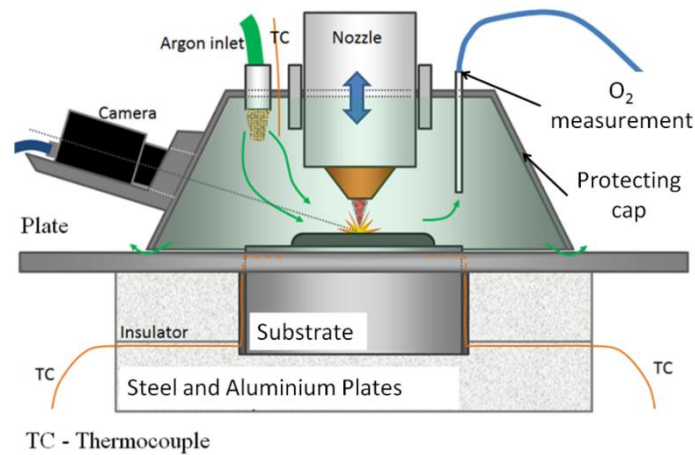


Figure 1. Scheme of laser metal powder directed energy deposition (LMPDED) equipment used for manufacturing thin wall specimens.

The main advantages of DED processes compared to Powder Bed Fusion (PBF) processes (Laser L-PBF or Electron Beam EB-PBF) are their high versatility and controllability. They can be used for manufacturing new parts, including directional solidification or single crystal cases, for adding features to existing parts and for functionally graded parts [1]. DED is often used to provide an effective and minimally invasive approach, preventing the replacement of price-sensitive products [2]. Its use in repair operations receives increasing interest in industry [3-5]. Production of functional prototypes is another market, alongside with production of small series. The variation of powder composition and the process parameter windows allow a tight control of chemical composition, melt pool size, thermal gradients and solidification rates to control the generated microstructures [6]. Predicting and adapting the temperature distribution in parts produced by additive manufacturing processes is the basis for preventing distortion, residual stresses and microstructural phenomena. To this end, Graf et al. [7] performed numerical analysis to determine the influence of wire feed rate and weld path orientation on the temperature evolution of multi-layered steel and magnesium alloy walls manufactured by cold metal transfer (CMT) technology, a new form of gas-metal arc-welding process. Kiran et al. [8] focused on developing an adapted weld model for DED simulations of parts size between centimeters and one-meter with a cost-efficient computational time. According to their results, the so called thermal cycle heat input reduces the computational time considerably but some limitations with transient heat input model are still required. Manufacturing defects such as low forming precision, coarse grains, and pores caused by local heat accumulation can be mitigated with vortex online-cooling [9]. Aldalur et al. [10] reported the use of oscillatory strategy for building a wall geometry with Gas Metal Arc Welding, resulting in an improved flatness and quasi-symmetrical geometry with a more homogenous microstructure than the overlap strategy. Despite these improvements, many issues are still to be mastered such as geometry accuracy, and microstructure monitoring and control. Crack

events during the manufacturing process or during cooling stage either at substrate-deposit interface or in the clad can also be an issue.

In order to be cost efficient and avoid expensive experimental work, different models can be applied. Pinkerton's review paper [11] lists two types of model trends: the empirical-statistical models and the physical models devoted to powder flow, melt pool, microstructure, stress, distortion or geometry. This article confirms that finite element (FE) analyses can be used to predict the thermal history and the distortions during the process, as well as the residual stresses or the microstructure at any material point. This quite extensive review [11] presents the current low level of knowledge about the DED models related to high speed steel with their complex microstructure, while titanium alloys or superalloys have been extensively studied. It reminds also that non-equilibrium material state present in DED process prevents easy use of classical continuous cooling transformation diagrams.

The simulation targets usually define the model scale. For instance, to prevent balling effect and understand pore formation, detailed melt pool modelling and fluid simulations cannot be avoided. Note that with such a fluid methodology, in DED, Khairallah et al. [12] explains the flaw mechanism for both stainless steel 316L and nickel-based superalloy IN738LC, while Heeling et al. [13] presents the optimization of the process parameters for stainless steel. However, the micro scale of these models prevents them to address the simulations of whole parts, while even lower scale and other type of models, for instance Phase Field approach [14,15] would be required to analyze the segregation behavior and the generation of phases. As explained by Jardin et al. [16], the precipitation of the carbides within M4 cladding results in a heterogeneous distribution of the carbide shape, size and nature along the depth of a clad sample. A phase field model is a further step for ULiège team. Another example of the interest of low scale method is the study of the diffusion between Si inclusions and Al matrix for AlSi10Mg determining the rupture location [17].

At the macroscopic scale, more adapted to industrial parts, the inherent-strain-based method [18] is often used. It assumes incompatible strains from different sources and decouples stress components. However, the accuracy of this method for complex parts is not guaranteed and a careful calibration is always required either based on direct experiments or based on a detailed validated simulation. Detailed FE simulations close to the physical phenomena is this paper scope. It provides a deeper understanding of the material history within the process and helps to identify its control parameters. However, those simulations still present CPU issues, which limits them to simple parts. As demonstrated hereafter, the mechanical result accuracy is not guaranteed for complex material as M4 steel deposited on 42CrMo4 substrate.

As the thermal field is the key factor, numerous 2D and 3D FE simulations at the macroscopic scale have been developed for academic samples providing the thermal history of deposits. For instance, special focus on the heat affected zone is chosen by Yang et al. [19] while the effect of the laser scanning speed on the thermal evolution and on the melt pool size is studied by Patil and Yadava [20], of laser power by Yin et al. [21] and of preheating temperature by Chiumenti et al. [22]. However, those previous works do not discuss the impact of the accuracy of the input material parameter data on their predictions. Often by lack of knowledge, strong simplifications are done. A common simple assumption is to neglect

the variations of the thermo-physical properties with the temperature [23] or adopting constant heat convection coefficient for the boundary conditions [24], while the variation of this coefficient with the geometry and the temperature was demonstrated by [25]. The shape of the heat input developed by Goldak work [26] intended to model the laser beam heat source could be used, however, a constant local value of heat input or a simplified shape is often adopted [27,28].

Another cut off from the complex physics concerns the geometry of the added material at each track within a new layer of added material. By convenience, it is often a cuboid volume related to mean size of the track height and the track width. Within thermo-mechanical solid FE simulations, only some models like the one of Lindgren et al. [29] compute the added volume shape based on physical assumptions. Another way is chosen by Caiazzo et al. [30] which defines it by regression formulas based on an extensive experimental campaign.

Key material information such as visco-plastic behavior within the mechanical model is usually based on experimental measurements from samples not manufactured by DED [29]. However as pointed by Lu and his co-workers [31], this approach is not reliable to generate accurate predictions as mechanical and thermo-physical properties strongly depend on microstructures which are different in casting or forging or Additive Manufacturing processes. The sensitivity analysis of Lu et al. [31] about the effect of mechanical properties of Ti-6Al-4V alloy shows that the distortion and residual stresses strongly depend on the values of the thermal expansion coefficient and the elastic limit, while slightly on the Young's modulus.

The present research is focused on a thin wall sample of ten layers of M4 material on a substrate in 42CrMo4 steel. Thermo-mechanical finite element simulations compute thermal history of the clad material as well as distortion and local temperature of substrate. As shown next, the access to accurate material data for this specific high speed steel (HSS) grade is more problematic than CPU issues. A thorough validation of the model results is conducted using the predicted displacement and temperature curves of different points in the material, which are compared with their corresponding measured values throughout the process, including substrate preheating, deposition and cooling. Final microstructure is measured by optical and scanning electron microscopy performed at the middle cross-section of the thin wall and substrate for further correlation analysis with the thermal history. Note that M4 material was selected because of its enhanced performances in wear and hardness when manufactured by DED [32,33]. However high amount of carbon in the material composition combined with thermal and/or phase-transformation stresses generates a high susceptibility to crack formation [34,35]. This feature explains why DED of tool steels remains very challenging. In addition to the usual process parameters such as laser power, scanning speed, powder flow rate and scanning strategy (laser path, idle time, track inter-distance), the identification of the pre-heating temperature level is a mandatory step.

The cracks easily appear due to the tensile stress generated in the clad bottom or at the clad-substrate interface during the cladding process. The preheating temperature of the substrate decreases the space thermal gradient, the cooling rate and minimizes the thermal distortions and stresses during the process. As shown by Leunda et al. [36] for CPM 10V and Vanadis 4 extra tool steel powders, the crack appearances can be avoided by a preheating temperature below the maximum tempering temperature. For M4 powder, Shim et al. [32]

specifically analyses the effects of the substrate preheating on the metallurgical and mechanical characteristics of the manufactured parts. The results enhance the effect of the preheating on the cooling history and solidification rates. Specimens without preheating mainly include equiaxial fine grains whereas the induction-heated specimens generate columnar grains. However, no significant hardness differences were measured, which could be explained by secondary hardening mechanism caused by hard and stable carbides. As pointed by Jardin et al. [16], for a preheating of 300 °C and a 36 layer clad of 40 x 40 x 27.5 mm³ (a bulk sample compared to the thin wall geometry studied here) a strong heterogeneity appears within the clad deposit due to different thermal histories. Close to the deposit free surface and at mid-height, the angular-like MC carbides precipitated in intercellular zones just after the primary cells. The high superheating temperature within the melt pool at mid-height of the deposit promotes the coarsening of the solidification phases including cells and intercellular carbides. At intermediate depth of 4.5mm from the deposit free surface, a lower superheating temperature and a higher number of re-melting of the material points promote the precipitation of coral-like MC carbides inside cells.

The present article aims to quantify the variation of the numerical predictions due to different material properties such as stress-strain relationship, thermo-physical variables or boundary conditions such as convection and radiation flow. The prediction of distortion currently achieved lacks precision when compared with experimental results, however, forthcoming work on improving predictions, reducing residual stress and increasing microstructure homogeneity will be based on numerical optimization. The complexity of the multi-phase materials of both the clad and the substrate demonstrates that the model sensitivity analysis presented in this work is a required stage for obtaining reliable results.

The paper describes the thin wall experiment in Section 2.1, the metallographic observations in Section 2.2, and the FE model in Section 2.3. The results of the material data measurements are provided in Sections 3.1 and 3.2. The validation of the model is performed through a comparison between thermal history predictions of the substrate with experimental results in Sections 4.1. In Section 4.2., the observed microstructure by Optical Microscopy (OM) and Scanning Electron Microscopy (EM) are explained based on the predicted thermal history of the clad. The thermal and thermomechanical sensitivity analysis and discussions are given in Sections 4.3 and 4.4, respectively. Finally, Section 5 provides the summary of the key results and the perspectives for ongoing research.

2. Materials and Methods

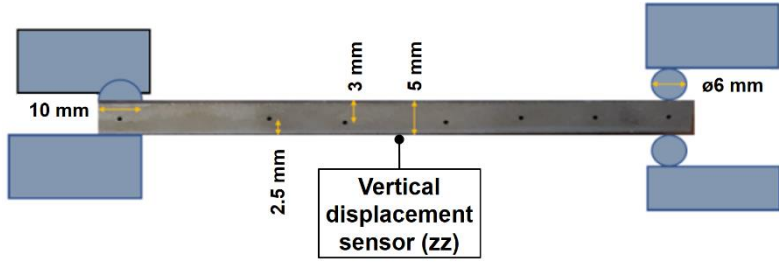
2.1. Thin wall experiments

The composition of the HSS M4 commercial powder with its particle size ranging from 50 µm to 150 µm is provided in Table 1. The 5-axis Irepa Laser Cladding system with a Nd-YAG laser of maximum power capacity of 2000 W from Sirris Research Centre is schematically described in Figure 1. The laser has a wavelength of 1064 µm and operates continuously. The metal powder is injected with an angle of 45 degrees. The laser has a top-hat energy distribution with a mean diameter of 1500 µm (1400 µm at the top and 1600 µm at the bottom). The substrate consists in a small rectangular bar of 8 mm height, 10 mm width and 120 mm length of 42CrMo4 steel (Figure 2b). The bar supports are shown in Figure 2b while the thermocouple (TCs) positions are given in Figure 2c. The preheating to prevent the crack

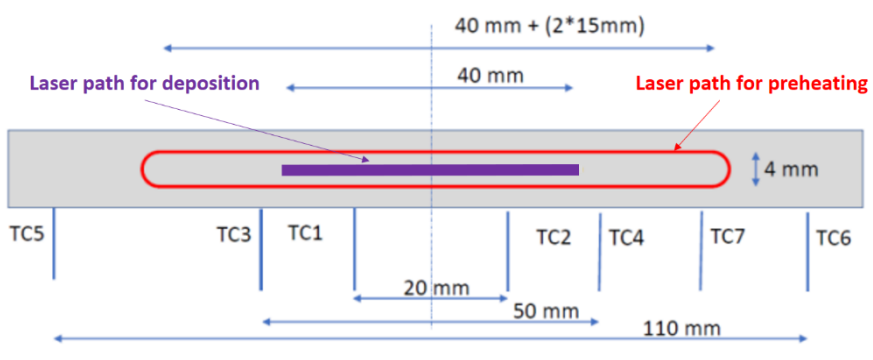
appearance in the deposit is performed by preliminary laser passes (red line in Figure 2c). Pre-heating temperature values from 217 °C to 400 °C were generated. For the lowest pre-heating temperature, cracks appear during the deposition of the fifth layer at the extremities of the substrate-clad interface (Figure 2a), but when manufactured with a pre-heating of 400 °C sound samples were achieved (Figure 2d). Table 2 gives the process parameters of the simulated manufacturing cases. The final manufactured thin walls of 40x4x1.5 mm³ are centred on the substrate top surface.



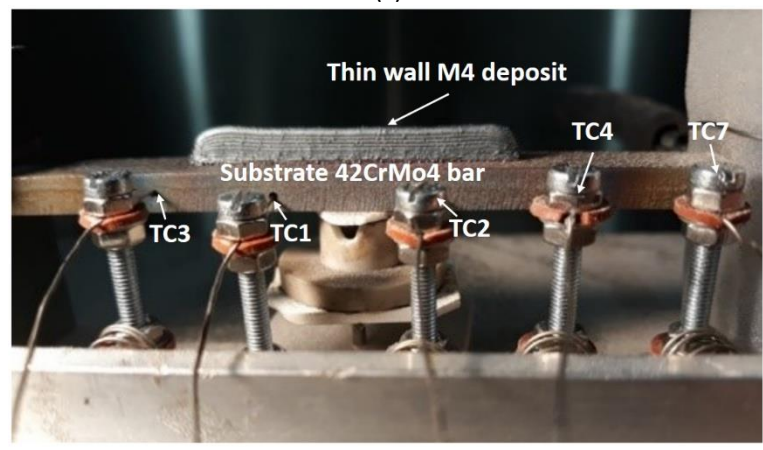
(a)



(b)



(c)



(d)

Figure 2. (a) Crack at the fifth layer of the sample; (b) and (c) show geometry, boundary conditions and position of the thermocouples (TCs); in (c) both the laser path for preheating and deposition stages; (d) global view of the set-up after deposit.

Table 1. Chemical composition of HSS M4 (wt. %).

C	Mn	Cr	Mo	V	W	Ni	Si	Fe
1.35	0.34	4.30	4.64	4.10	5.60	0.9	0.33	Balance

Table 2. Process parameters and TC2 thermocouple values.

	Laser pass length for pre-heating and cladding (mm)	Laser beam speed (mm/s)	Laser power (W)	Temperature at TC2 at the end of pre-heating and at beginning of cladding (°C)	Number of laser passes
Substrate pre-heating 1	40	41.7	260	217	20
Clad deposition 1	40	8.3	500	134	10
Substrate pre-heating 2	70	41.7	260	400	20
Clad deposition 2	40	8.3	600-400 ₁	310	10

¹ The power decreases linearly with the number of layers from 600 W for the first layer to 400 W at the end of the clad.

2.2. SEM and OM metallographic observations

The samples were mirror polished with OPS finish, followed by etching with Vilella's reagent. Figure 3 shows the cross-section observations of the sample obtained by optical microscopy (OM) and scanning electron microscopy (SEM). OM images show a dark region of the deposit in the lower layers, except for the junction area, and a lighter region at the top, specifically in the last two layers. The fine precipitates in the dark areas are not present in the light areas as observed in the SEM images. Both zones show a cellular type microstructure with eutectic carbides in the cell junctions, as already demonstrated in bulk deposits after manufacturing [16], or after tempering [33]. The matrix is of the martensitic type with eventual zones of residual unprocessed austenite, as already observed in a similar alloy [37].

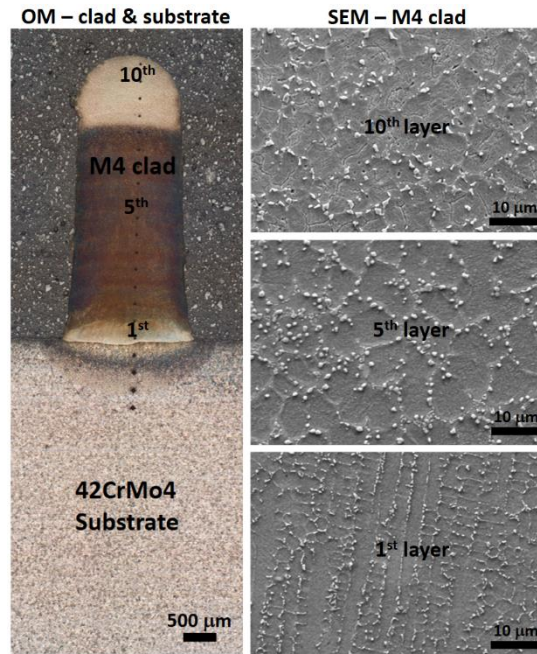


Figure 3. Vertical cross-section observations of the thin wall sample obtained by OM and SEM.

2.3. Finite Element model

The coupled thermomechanical simulations are performed using *LAGAMINE* code, a finite element software developed at the University of Liège since 1985. It has already been applied on many material forming processes. The FE results of Pascon et al. [38] predicted the crack events in a continuous casting process. Neira Torres et al. [39] studied the manufacturing of bimetallic rolling mill rolls and computed residual stress state validated by X-ray diffraction. Guzmán et al. [40] simulated incremental sheet forming and focused on the geometry and force predictions with comparison with test measurements.

In Tran et al. [28], a 3D thermal simulations of DED of Ti6Al4V alloy with microstructure predictions validated by a measured hardness distribution map and microscopic observations was presented. In the present work, an extension of this model to mechanical analysis is used where temperature and displacement fields are simultaneously computed within an implicit strategy. Note that other thermo-mechanical FE models like the ones of Mukherjee et al. [41] or Chew et al. [42] apply sequential analyses where the thermal field is assessed in a first stage and applied as static load during the mechanical analysis defining the second step of the model. As the final goal is to reach a complete thermo-mechanical-metallurgical model, this staggered solution was not selected to prepare the future steps where all the couplings will be taken into account as the phase transformation key temperature can be strongly impacted by mechanical stresses.

However, currently only thermo-mechanical simulations are performed. The lack of material data prevents the activation of the coupled thermo-mechanical-metallurgical module able to predict kinetic of solid phase transformations like in previous researches [39]. Currently, the thermal expansion coefficients used for the clad and the substrate take into account phase transformation events through a multi linear curve depending on temperature. The latter is however not related to cooling, heating temperature rates and phase

distribution. Without a more accurate input, the measured displacement field could not be totally correctly predicted as shown below. However, a reference case was defined to allow a sensitivity analysis. The material model of the clad and the substrate is elasto-plastic based on von Mises yield locus and multilinear tangent modulus for isotropic hardening. Young's modulus, elastic limit and isotropic plastic hardening are temperature dependent. Note that the set of associated tangent plastic moduli is kept constant for each curve. Besides, as low viscosity effect is confirmed by the mechanical tests (Section 3), the strain hardening model is rate-insensitive.

The 8-node 3D brick (BWD3T) thermomechanical finite element implemented in the Lagamine code by Zhu et al. [43] is selected. The element is based on the non-linear three-field HU-WASHIZU variational principle of stress, strain and displacement [44–46], and uses a mixed formulation adapted to large strains and large displacements with a reduced integration scheme—only one integration point—and an hourglass control technique.

The FE solid model simplifies the physics of all the phenomena present in the melt pool. The effect of the latent heat of the fusion (L_f) is integrated in the definition of the thermal capacity (c_p), defining an apparent property. The effect of the fluid motion due to the thermo-capillary phenomenon (i.e. Marangoni flow) is not considered. Other solid studies just consider a multiplicative factor to enhance the conductivity value within the melt pool [42,47]. Such a factor varies according to the researches, for instance, Cao et al. [47] uses a value of 3 for Ti6Al4V alloy while Bi et al. [48] uses a value of 5 for iron-based martensitic stainless-steel METCO 42C, respectively. Initially for welding, Lampa et al. [49] suggested a value of 2.5 for an Austenitic stainless steel. Hereafter, following the arguments of Lindgren et al. [29], no multiplicative factor is applied as it counteracts the energy distribution defined in the heat source model. Clearly, such assumptions are not independent on the powder laser absorptivity factor β which is the current work numerically tuned within the simulations process to agree with the observed melt pool size and the measured thermal history.

A second simplification consists in the energy distribution of the heat flow of the laser. While the model developed by Goldak defines a double ellipsoidal power density distribution [26], a simple circular Gaussian is often considered [27,50]. The model considered in this present research is even simpler: the mesh size has been adapted to the laser spot radius. The clad finite cubic elements have a 0.75 mm width to model the laser top-hat energy distribution with a diameter of 1,5 mm. As only half of the process is simulated by symmetry, the final clad volume modelled is 40.5 (length) x 0.75 (width) x 4 (height) mm³. Indeed, the mean height of the layers has been measured and corresponds to 0.4 mm. The effect of the moving laser beam is taken into account by updating the laser input power within the affected nodes, based on the real velocity and the trajectory of the laser processing head.

The 3D mesh of the substrate presents a mesh refinement depending on the space position. Refined elements are defined near the clad in order to accurately model heat fluxes, while the substrate bottom is meshed coarsely. To generate an accurate mesh, transition refinement elements were used as shown in Figure 4. The thermal boundary conditions of the model consist in convection and radiation in all surfaces except the symmetry plane and the supports where heat is transferred by conduction. Figure 4 also shows the mechanical boundary conditions of fixed support and roller support at the end of the substrate bar.

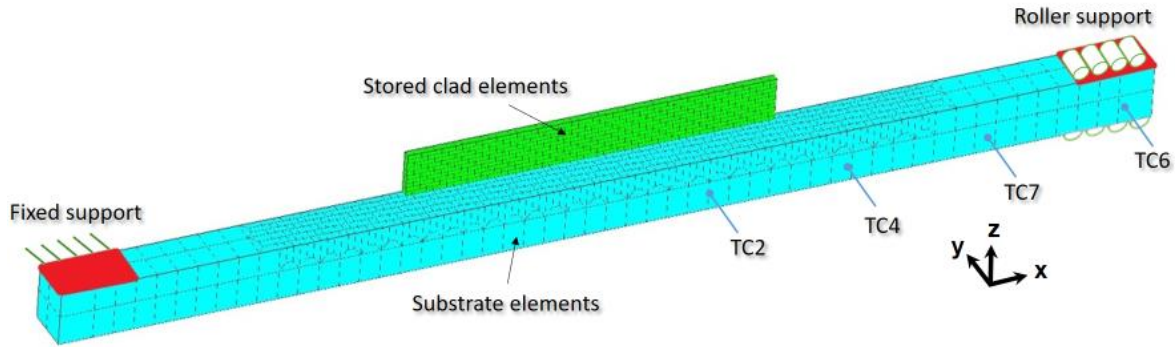


Figure 4. Initial symmetric mesh with the stored clad element (green) for future element activation, the mechanical boundary conditions in red (on the left, all the displacements x,y,z are fixed while on the right, only z displacements are prevented).

The principle of the element birth technique modeling the addition of material within the process is shown in Figure 5 on a simplified mesh. When a new layer is created during the material addition process, a group of four solid elements for the complete sample width (two elements, by symmetry here) is activated with their boundary conditions. LAGAMINE software applies convection and radiation by interface elements that rely on classical thermal equations as described in Tran et al. [28]. When the laser beam is ongoing, new solid elements are activated with their new convection and radiation surface elements around them while the convection and radiation elements under the new solid elements are de-activated. The laser power is directly applied at the top nodes of the activated elements.

The concept of numerical annealing temperature (T_{anneal}) [51,52] from welding models is applied here. It seems physically consistent to neglect any plastic strain performed at higher temperature than a well-chosen annealing temperature. In the finite element code, if the temperature of the material point (integration point within an element) is higher than T_{anneal} , the material will lose its hardening memory; this effect is taken into account by setting the equivalent plastic strain to zero. When the temperature of the material point falls lower than T_{anneal} , the material can work harden again. For instance, several authors [25,31,53–55] exploit this approach in order to compute the stress field and perform a sensitivity analysis to this annealing temperature value. However, the sensitivity of the predicted displacement field was lower than that of the stress and it seems not a key feature in the current validation. Three different annealing temperatures (527, 727, and 1027 °C) were investigated plus a case without annealing. It was observed that the annealing temperature had low impact on the thermomechanical model and thus a final temperature of 527 °C was used, as it led to faster convergence.

The thermal boundary conditions considered in the numerical simulations takes into account an absorption factor β which differs for the preheating step and the cladding one. Its values are respectively 0.65 and 0.4 and were adjusted to recover the thermal measurements. During the pre-heating the surface is flat compared to the clad deposition, implying a better absorption of the laser energy and a higher absorption factor.

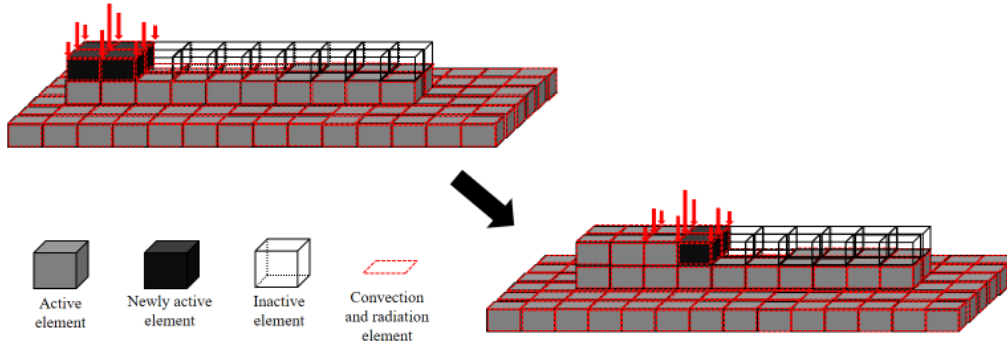


Figure 5. Schematic representation of the element birth technique.

3. Material parameters

3.1. Thermophysical properties

The thermo-physical properties of the clad samples (Figure 6) manufactured by DED and the substrate were measured by He pycnometry, dilatometry (density, ρ), differential scanning calorimetry (DSC) (thermal capacity, c_p), and laser flash analysis (LFA) (thermal diffusivity, α) within a range from 20 to 1100 °C (Appendix). LFA measurements were carried out by steps of 100 °C. For the clad material, latent heat was also measured by DSC up to 1410 °C and added to the thermal capacity c_p (J/kg.°C), defining an apparent heat capacity c_p^* (J/kg.°C):

$$c_p^* = \begin{cases} \frac{L_f}{TD-T_m} + c_p, & \text{if } TD \leq T \leq T_m \\ c_p, & \text{otherwise} \end{cases} \quad (1)$$

where L_f (J/kg) is the latent heat of fusion, T_m (°C) the starting melting point (solidus temperature) and TD (°C) the ending melting point (liquidus temperature). Finally, the thermal conductivity k was obtained using the following equation:

$$k(T) = \alpha(T) \cdot \rho(T) \cdot c_p(T) \quad (2)$$

The errors associated with the equipment (Accupyc 1340 Micromeritics, DIL 402C Netzsch, DSC 404C Netzsch, LFA 427 Netzsch) and measurements are 3% for c_p , 7% for k and 2% for ρ .

To measure the enthalpy of melting, sigmoidal baseline type was used to determine the area of the peak (Figure 7). The accuracy of enthalpy measurements is about $\pm 5\%$. The measured values were 1230 °C for T_m , 1404 °C for TD and 313 J/g for the area of enthalpy of melting, L_f . The thermo-physical data identified for M4 can be found as a function of temperature in the Appendix. It is worth noting that the measured values are within the range of partial results given in [59] for M4 HSS.

The substrate properties first relied on previous tests performed on 42CrMo4 grade in Bainitic-Martensitic state. The used values in simulations were similar to values found in [60]. However a closer look at the material certificate identifies a pearlitic state which justifies the final use of properties reported in [61], similar to what was finally measured on the substrate (Figure 8) where phase transformation occurs. This modification was a mandatory point to be able by simulations to recover the thermal field measured during substrate pre-heating, showing the high sensitivity to thermo-physical properties.

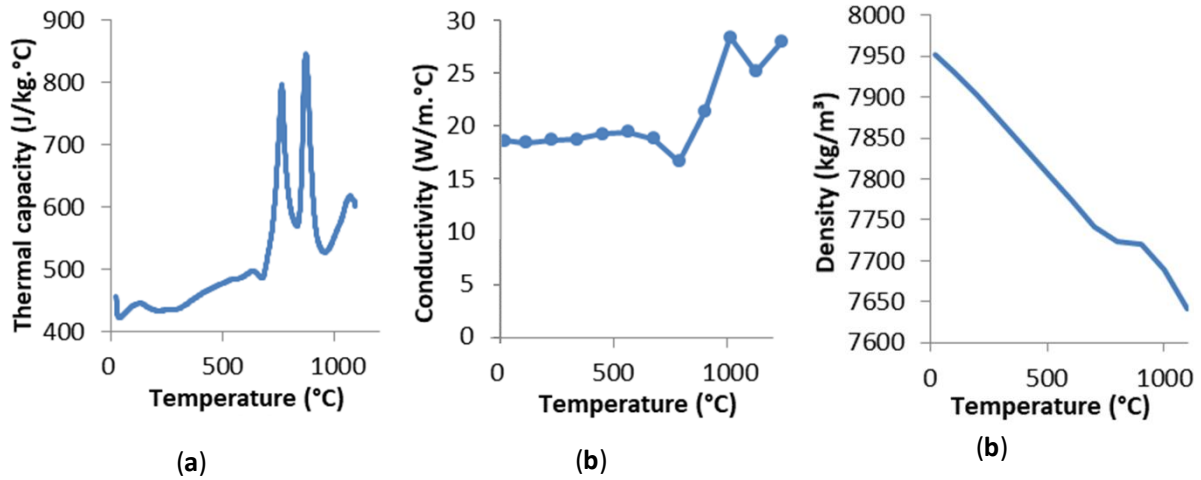


Figure 6. Thermo-physical properties of HSS M4: (a) thermal capacity, c_p ; (b) thermal conductivity, k and; (c) density, ρ .

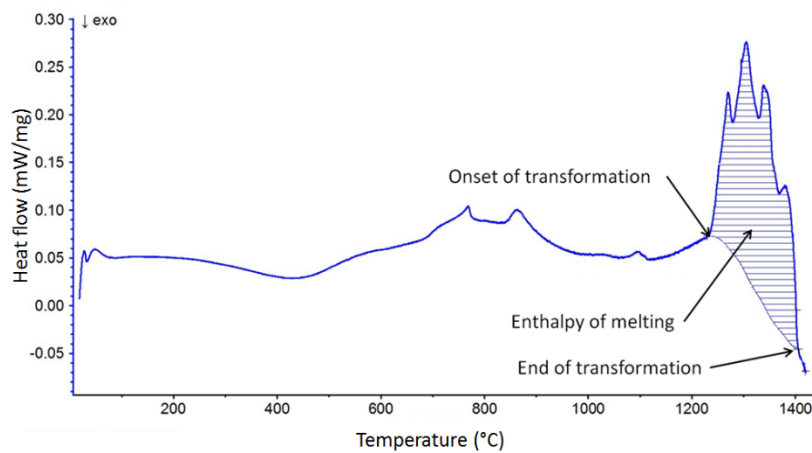


Figure 7. DSC measurement showing the latent heat of fusion of M4 (scanning rate of 3 °C/s).

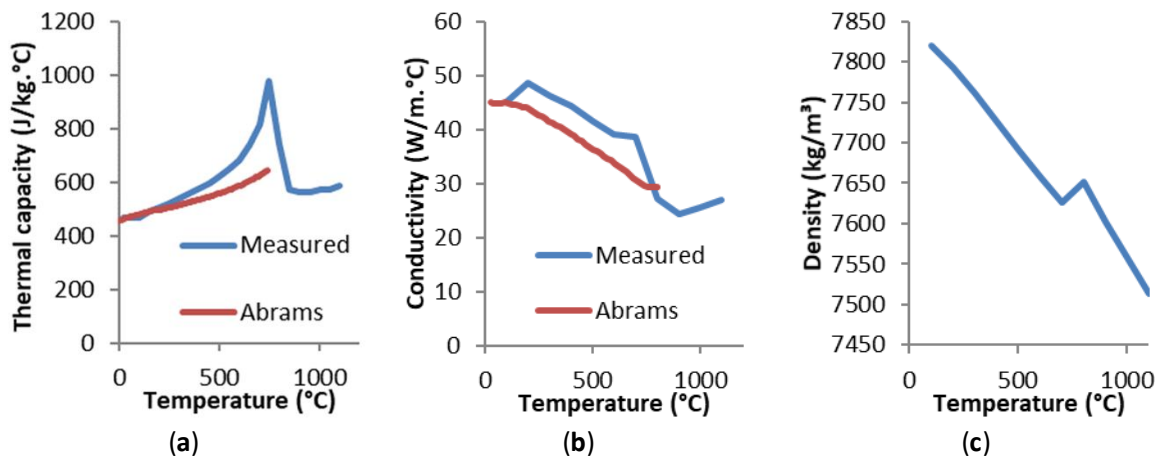


Figure 8. Thermo-physical properties of 42CrMo4: (a) thermal capacity, c_p ; (b) thermal conductivity, k ; (c) density, ρ . Measurements heating and cooling generating pearlite state at a rate of 3 °C/s.

Thermal expansion coefficients of the clad and the substrate are key issues for distortions and the stresses related to thermal gradients. However it should be measured in similar conditions as the ones happening in the process to provide correct values related to the real microstructure events. As non equilibrium and heterogeneous thermal histories and microstructures are known to be present within M4 clad samples [16], the applied temperature dependent coefficient should be not related only to temperature value. The transformations are affected by temperature heating and cooling rate and successive transformations vary the chemical composition of phases. Finally, the stress state is known to shift key temperature features. One should build the dilatation coefficients from knowledge related to the kinetics of transformations and representative experiments. Within the cladding process, the material is submitted to temperature rates up to 4750 °C/sec during cooling for instance, while the available measurements were limited to of 200 °C/s cooling rate. This cooling rate is enough to achieve phase transformation without diffusion. Last but not least the initial state of the sample affect the results. To be close to real values, samples were extracted from bulk samples manufactured by DED process (process parameters: Laser power of 1160 W; nozzle speed of 462 mm/min and powder flow of 86 mg/s). Dilatometry tests, for cooling down from 1200 °C to room temperature at 120 °C/sec provide Martensite start temperature M_s (260 °C) and, for a cooling rate of 0.5 °C/Sec, Bainite start temperature B_s (370 °C) is obtained. However the microstructures were different between the thin walls and the bulk samples as bainitic, martensite and residual austenite were not in the same proportions. So extracted data (Figure 9-10) are still not reliable as the tested samples were neither re-melted (maximum temperature in dilatometer is 1100 °C, far from 1404 °C Liquidus and superheating temperature experienced within the melt pool not reached) nor submitted to correct the cooling rate during the process. Note that the effect from the cooling ratio and stress state is actually not taken into account.

Finally, the thermal expansion measured on DED samples (Figure 9) and data found within the literature defined a basis to assume the curves plotted in Figure 10 used within the reference thermomechanical simulation.

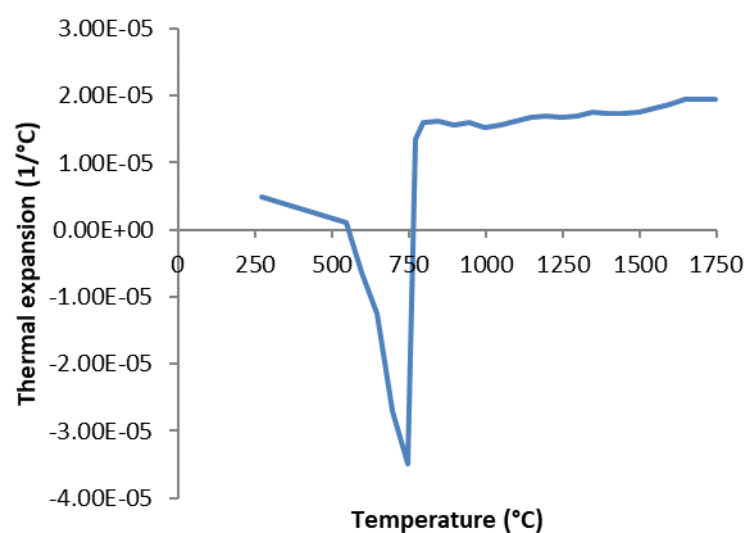


Figure 9. Thermal expansion coefficients for M4 from bulk sample (bainite/martensite) obtained with quenching cooling of 200 °C/s.

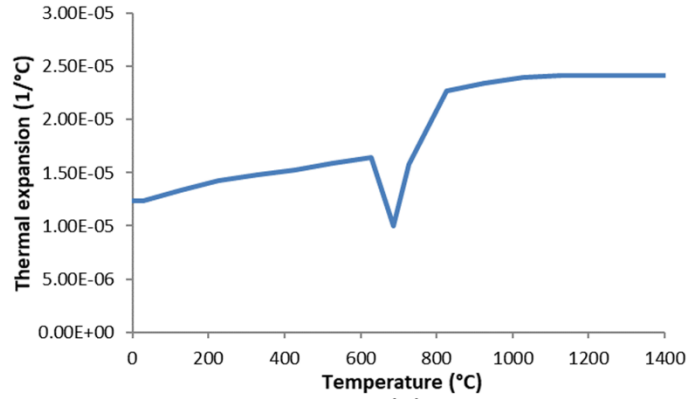


Figure 10. Thermal expansion coefficient used in reference simulations for 42CrMo4.

Note that those thermal dilatation coefficients follow the classical metallurgist definition of:

$$\alpha(T) = (1/L_0) (L_T - L_0)/(T - T_0) \quad (3)$$

where index 0 means room temperature and initial sample length $L_0 = L(T_0)$.

3.2. Stress strain curves

Compression tests of cylinders of 8 mm diameter and 10 mm height were carried on HSS grade M4 samples at different temperatures and different strain rates in order to determine the stress-strain curves. The tests were performed with a Schenck 400 kN machine and a quad elliptical radiant furnace 4x2000 W was used for high temperature tests. The compression samples were cut using wire electro discharge machine from a part of a bulk deposit produced by DED (see Figure 11a and manufacturing conditions defined in Section 3.1). Samples were tested at room, moderate and high temperatures (20, 300, 500, 950 °C) and at different constant strain rates (2×10^{-3} , 10×10^{-3} and $50 \times 10^{-3} \text{ s}^{-1}$). For each combination of temperatures and strain rate conditions a minimum of three samples were tested. Note that the very high elastic stiffness of the samples compared with the press stiffness at moderate and high temperatures often affects the axial displacement actually applied on the samples. This test feature must be taken into account to reach an accurate constant strain rate test. An approach based on a linear speed of the press plateau decreases the precision of the measured elastic limit. The methodology of Tuninetti et al. [62] is applied here to achieve a real constant strain rate and an accurate yield stress.

As shown in Figure 12, the effect of strain rate in the analysed range (2×10^{-3} to $50 \times 10^{-3} \text{ s}^{-1}$) is not very significant. The highest strain rates show the lowest hardening. This effect is more obvious at room temperature (Figure 11b). If the plastic range can be trusted, the Young's modulus is not reliable in those compression tests, it is more a trend than an accurate characterization and its identification is explained in next paragraph. For the case at 950 °C just one sample was successfully tested, however the stress-strain curve measured by Neira Torres et al. [39] on a similar composition and forged samples are in close agreement. Based on those results, the strain rate sensitivity can indeed be neglected in the DED simulations of this material. Within the Lagamine simulations, the mean curves for $2 \times 10^{-3} \text{ s}^{-1}$ strain rate

described by multilinear segments for each measured temperature define the hardening law. The intermediate values are interpolated for any strain and temperature.

The value of 216.3 GPa for the Young's modulus relies on grindosonic measurements at room temperature. At higher temperatures, the Young's moduli measured by Neira Torres et al. [39] on high chromium steel heat treated samples are used, the heat treatments provided different phase percentages. This input data base allows to correct non-reliable experimental Young's moduli of this research by a mixture law for the compressed samples. According to the observed microstructures of the bainitic bloc (Figure 11a) and of the martensitic thin wall (Figure 3), Figure 12d provides more an evolution trend than an accurate characterization of the Young's moduli with the temperature. For 42CrMo4 mechanical data, the simulations are based on the stress-strain curves provided by Habracken and Bouffiuox [63].

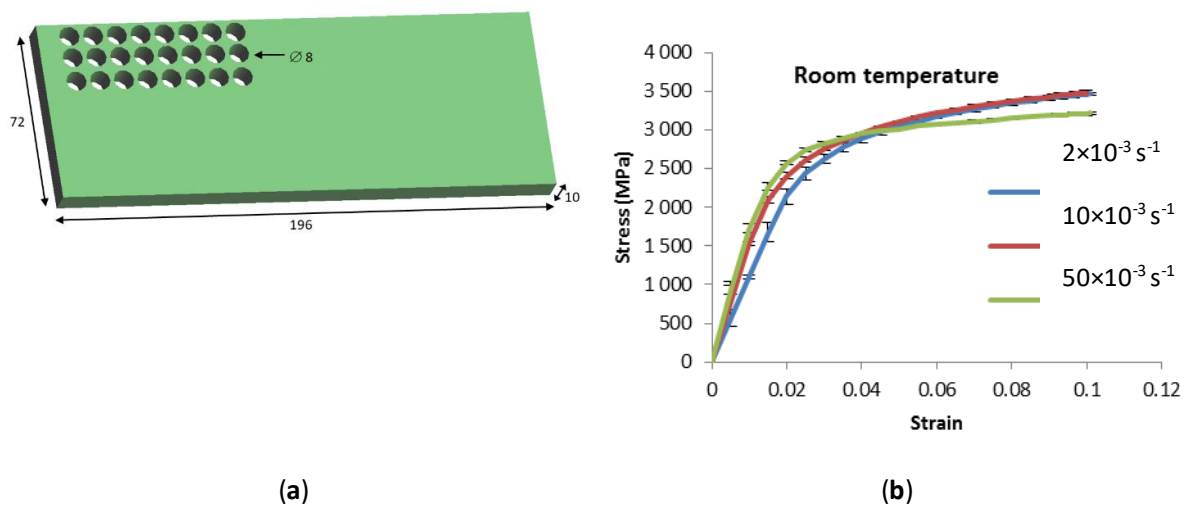
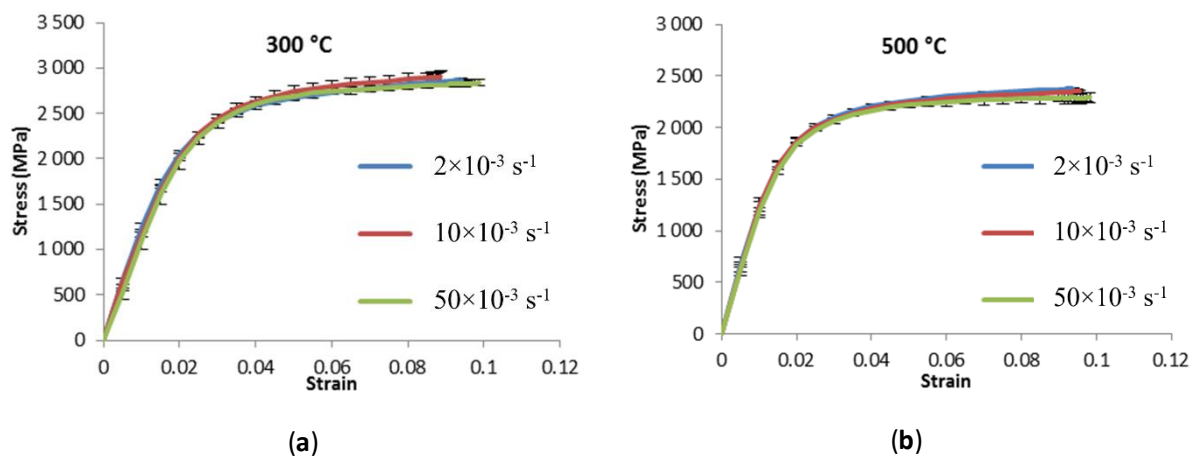


Figure 11. (a) Compression samples of $\varnothing 8$ mm cut from a LMD-P sample of 196x72x10 mm; (b) True stress strain curves for different strain rates at room temperature.



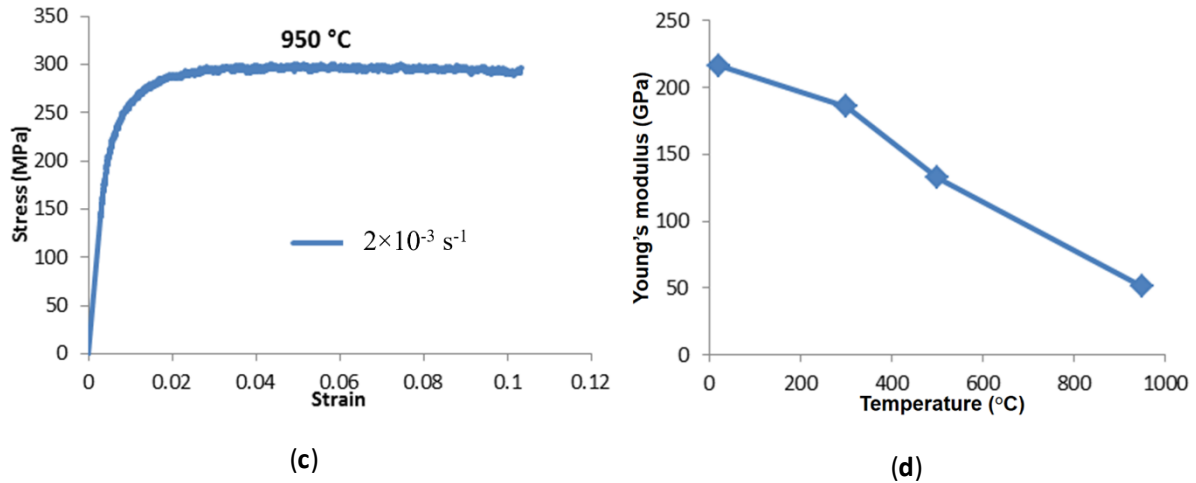


Figure 12. Stress strain curves at different temperatures and strain rates: (a) 300 °C; (b) 500 °C; (c) 950 °C; (d) Elastic modulus dependence on temperature for M4 DED material.

4. Results and discussion

4.1. Thermal history validation and potential effect on distortion

The laser absorption, convection and radiation coefficients were inversely identified by using the Levenberg Marquardt approach (Table 3). The simulation results of local temperature for preheating, cladding and cooling are compared to the measured values at the thermocouple points showing good accuracy predictions (Figure 13). The obtained local temperature values in the substrate near the cladding are more accurate than those at more distant substrate points especially during the cooling stage. These errors could affect the thermomechanical predictability of cladding distortion. However, by verifying the substrate mechanical boundary conditions (Figure 2 and Figure 4) and the low temperature values at TC6 and TC7 (less than 200 °C), the performed analysis indicates that the effect of this error on the measured z-displacement can be neglected. This affirmation was investigated through extreme fixations conditions and with high extraction of heat in the left fixation part.

Table 3. Coefficients of thermal boundary conditions for absorption factors (β) of 0.65 during pre-heating and 0.4 during deposition identified by inverse modeling.

Temperature (°C)	Convection coefficient for the clad		Convection coefficient for substrate (W/m ² .°C)	Radiation coefficient
	Pre-heating and deposition (W/m ² .°C)	Cooling (W/m ² .°C)		
20	1	1	1	0.59
500	32	5	5	
950	50	5	5	

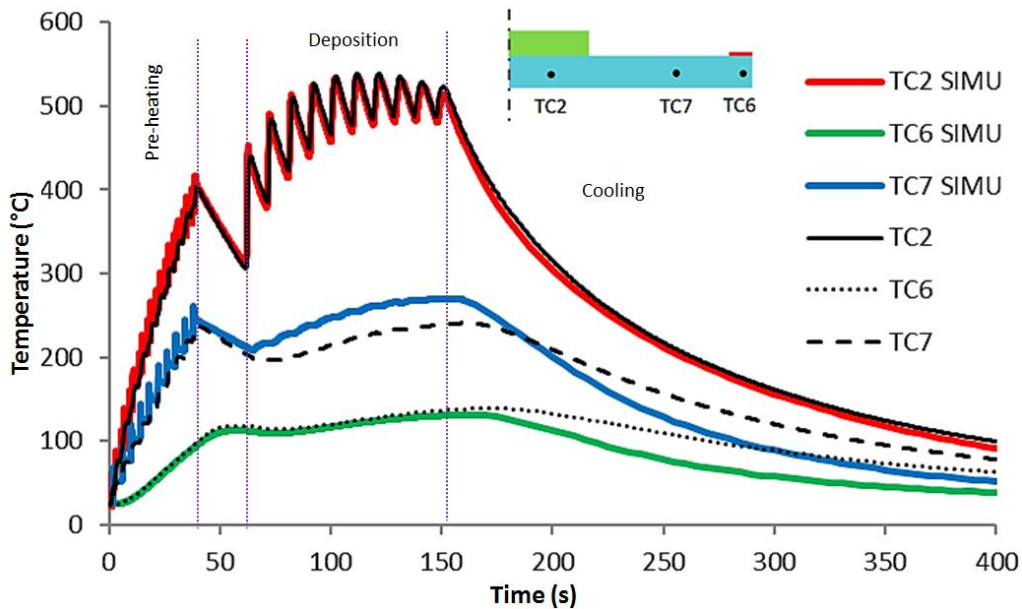


Figure 13. Validation of numerical results with thermal histories computed at the substrate thermocouple points TC2, TC6 and TC7.

4.2. Metallurgic validation

In Figure 14, red and blue shading zones give the range of temperature variations (maximum and minimum) after the last total remelting for material points belonging to the 1st and 5th layer respectively. The purple line (minimum temperature reached during the deposition process) increases until a maximum value of 527 °C. This curve confirms that neither bainitic nor martensitic transformations occur during the process time according to the Bs (370 °C) and Ms (260 °C) temperatures. When the laser processing is switched on, the matrix is austenitic. It is transformed totally or partially to martensite at the cooling stage when the laser is switched off.

As the solid matrix of a material point remains austenitic during the laser switch on period, once the temperature stays under the liquidus, a Pseudo Isothermal Annealing (PIA) period can be assumed. Such an approach is inspired from the work achieved on a Ti6Al4V alloy processed by DED [28]. For each material point, the PIA temperature is set as the average from all the temperature levels contained within the shading domain processing. This information helps to generate a simplified approach for microstructure predictions based on a similar way to what is achieved with TTT diagrams.

In Figure 14, the material point history of the central point of the 1st layer (blue curve) presents a first maximum peak (2081 °C), then the peak values gradually decrease with successive layer deposition. The situation is different for an intermediate layer such as the 5th one. The first peak (2161 °C), slightly higher than within the 1st layer, increases when the upper layer (the 6th) is added (2248 °C). These increases are due to the phenomenon of heat accumulation. This material point of the 5th layer is melted a third time when the 7th layer is deposited, but at a lower temperature. According to this thermal computed history, layer number 1 melts twice, while layer number 5 melts three times. However, none of the recorded points show more than one peak within the solidification interval (liquidus-solidus range). In Jardin et al. study [16] that focused on a bulk sample, it was established that

temperature fluctuations in this solidification interval strongly modify the solidification structure. In particular, it generates a microstructure with intra-granular pseudo-primary carbides. For the studied thin wall, the cell structure is such that carbides are present only in the cell junctions (inter-granular carbides), and not in the cell core for any layer.

The superheating temperatures of the last complete melting (1825 °C, 1456 °C, 1953 °C in layers 1, 5 and 10 respectively) and the cooling rates define the size of the primary grains and the cellular type solidification mode. The average size of the solidification cells shows a slight variation (see Figure 3), starting with a decrease between layers 1 and 5, and ending with an increase in the last deposit.

These observations are consistent with the solidification parameters experimentally observed: a cell refinement is favored by the very high cooling rate, the multiple remelting cycles and overheating of the liquid metal (Figure 3, 5th layer).

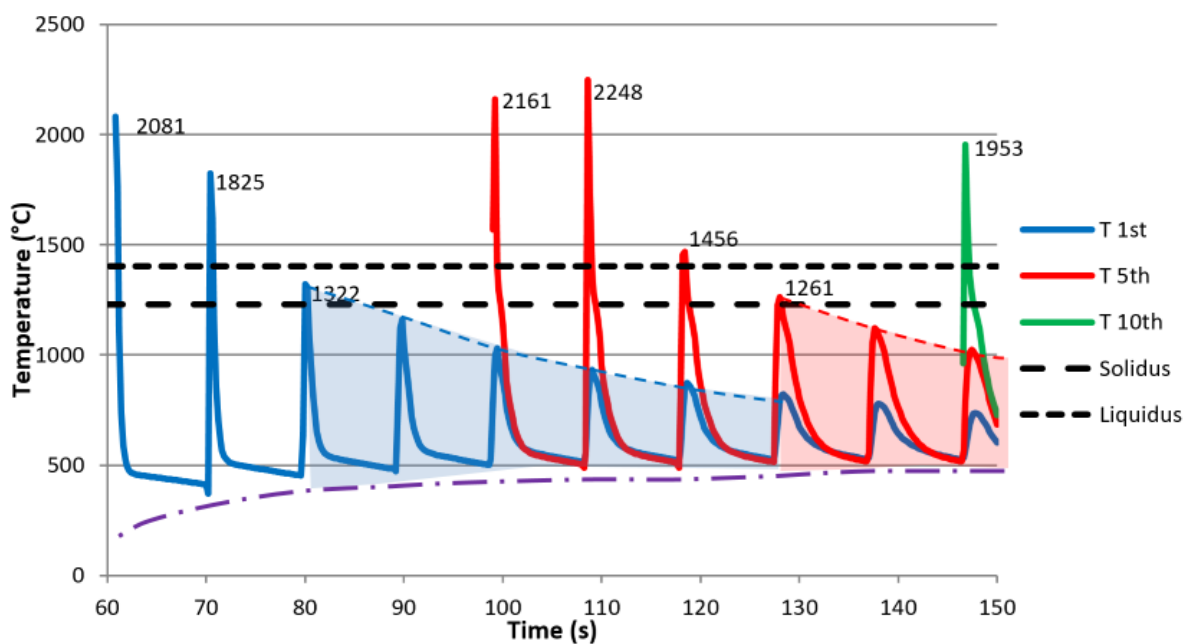


Figure 14. Thermal history of the 1st, 5th, and 10th deposits during the thin wall cladding process computed at a central point.

4.3 Sensitivity analysis of thermal response

This section evaluates the uncertainty of the model results caused by the effect of different error sources on input parameters such as power, thermal capacity and conductivity. The evolution of temperature over time at the measurement points T2, T7 and T6 are evaluated as a function of $\pm 20\%$ variations in the thermal capacity of the cladding and the substrate (Figure 15), the conductivity of the substrate (Figure 16) and the laser power (Figure 17) with respect to the values used in the validated reference simulation. Thermal histories computed for independent variations in either the conductivity or the heat capacity of the clad revealed an insignificant effect due primarily to the low mass of the thin wall cladding compared to the mass of the substrate. The negligible effect of such variations is not shown and becomes considerable when bulk deposits are analyzed as reported in [64].

Variations in the thermal capacity of the cladding and substrate significantly affect thermal history predictions (Figure 15). The largest temperature difference found with respect to the reference simulation is 16% at 27.4 s at the TC6 during the preheating stage. Increasing thermal capacity (c_p) by +20% produces a decrease in temperature by approximately 12% during pre-heating, followed by a linear increase of up to 5% difference at the end of the deposition. On the other hand, a negative variation of 20% of c_p generates a maximum temperature increase of 25% during substrate pre-heating stage, which then decreases linearly to 2% above the reference temperature at the end of the clad process. This asymmetric temperature behavior can be related to the interaction between conduction and heat accumulation, which makes the transient response non-linear with respect to thermal capacity. Finally, the results demonstrate that overall temperature is asymmetrically and inversely proportional to the thermal capacity.

The sensitivity analysis of thermal history to conductivity (Figure 16) shows different trends. Here, the effect of the variation is mainly visible closer to the clad. The phenomena observed are expected because with an increased conductivity, heat propagates more easily in the substrate. There is less heat concentration close to the deposit (hence lower temperature), and far from the deposit there is more heat transmission before being lost by convection and radiation. Conversely, lower conductivity increases the temperature near the cladding zone because more heat is transferred from the free surface of the substrate to the environment. This latter behavior is consistent with the lumped heat capacity of the substrate, where internal resistance to heat transfer becomes negligible in comparison to the external resistance of convection and radiation. This fact also explains the small effect of conductivity on temperature variations at TC7 and TC6 points located far from the clad. From figures 15 and 16 it can be concluded that the thermal history of the thin wall of HSS is more sensitive to thermal capacity than to conductivity.

Global sensitivity analysis of power (Figure 17) on thermal history is self-explicative. Results show that increase in power leads to an increase of temperature and vice-versa. Such high sensitivity helps to an easy identification of absorption coefficient.

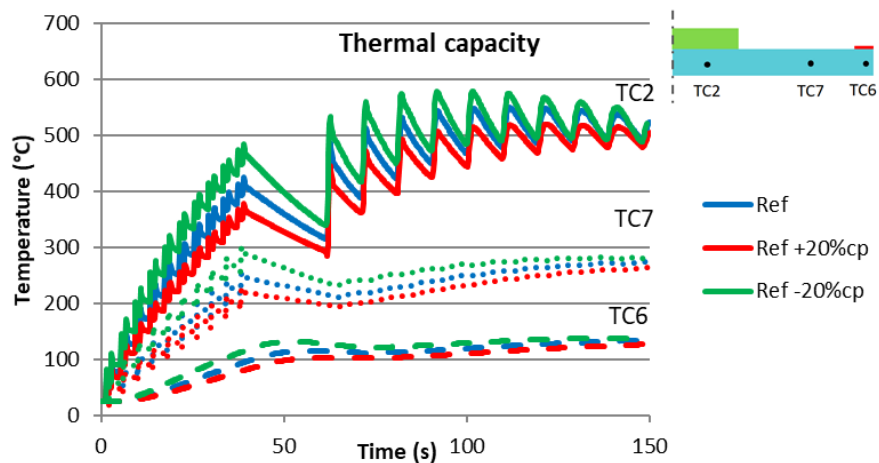


Figure 15. Sensitivity of thermal capacity variation of both clad and substrate on the thermal history.

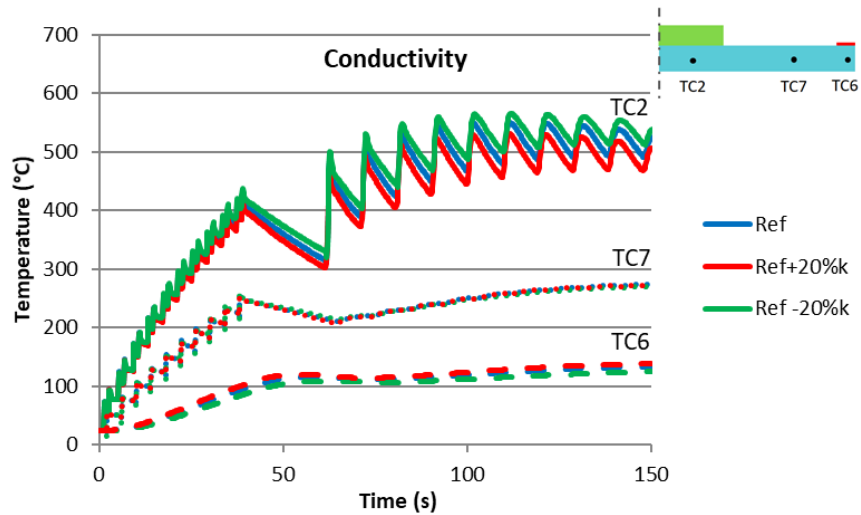


Figure 16. Sensitivity of substrate conductivity variation on the thermal history.

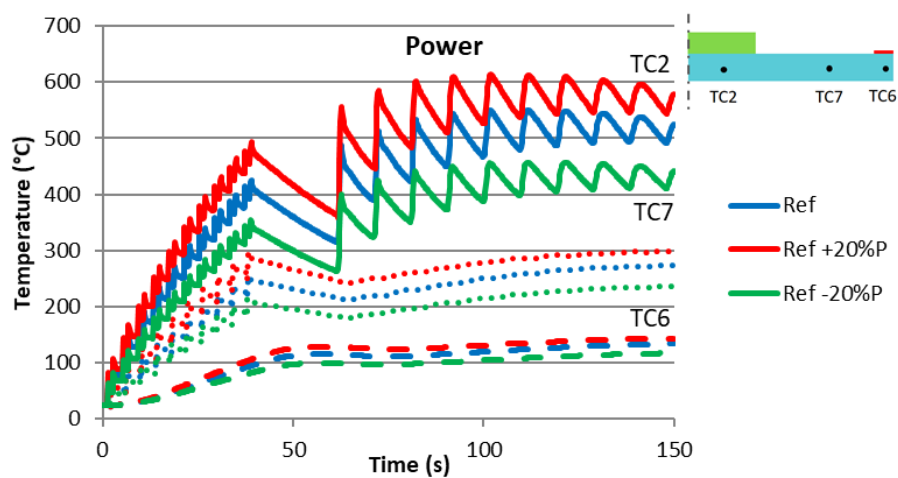


Figure 17. Effect of 20% positive and negative laser power variations on the computed thermal history at the local substrate measurement points T2, T6 and T7.

4.4 Sensitivity analysis of thermomechanical response

The identified evolution of thermal expansion coefficients of the clad and the substrate (Figure 9 and 10) are essential and highly influential for determining the behaviour of deformation and stress fields. However, these coefficient values strongly vary with the phase transformation kinetics of both materials. The impact of these phase transformations are not assessed in this article, as for that there would be the need to include a metallurgical model. Currently, metallurgical data and models for very high heating and cooling rates for high speed steel are lacking. Thus, in a pragmatic exploratory research, the assumed average thermal expansion curves of Figure 10 are kept the same and just the impacts of the Young's modulus and the yield stress accuracy are investigated.

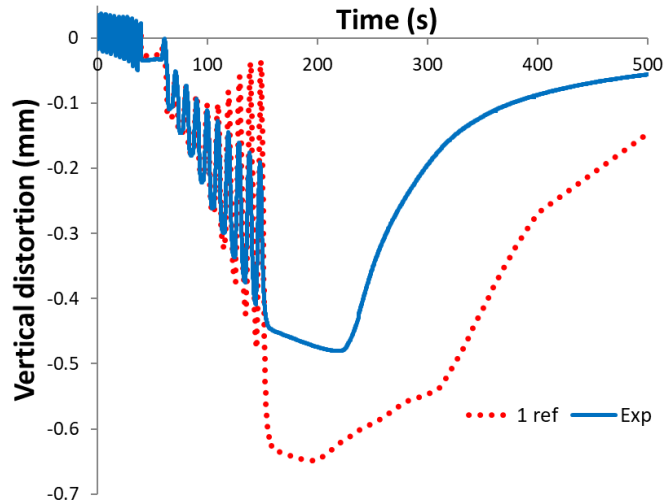
The predicted vertical displacements of the substrate bottom point at mid-length (ZZ sensor at Figure 2b) are compared with their measured values (Figure 18a) during the

preheating, deposition and cooling processes. Figure 18b shows the sensitivity analysis of the elastic modulus (E) and initial yield stress (S_y) on this displacement during the cooling stage. Note that the elastoplastic behavior of the material is based on a multilinear isotropic hardening law, taking into account both temperature dependence of the Young's modulus and the initial yield stress. The hardening shape defined for each temperature has not been modified. The FE predictions are in close agreement with the measured values denoted by Exp curve for both the preheating and the first five deposition stages (Figure 18a). Note that 3 similar experiments were performed with low scattering. The mismatch can be related to the microstructure transformations happening within the first layers as their temperature is low enough to reach solid-state transformation zones. A zoom on the process last stage, the cooling, is shown in Figure 18b.

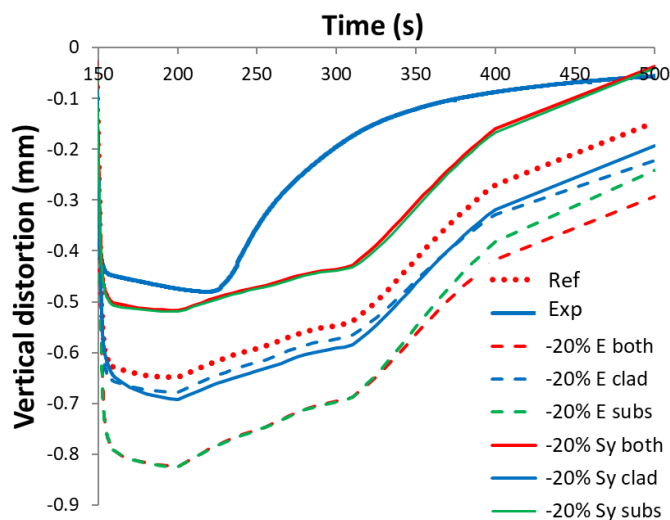
It has been numerically checked that within preheating and deposition stages, the effect of Young's modulus and yield stress variations are not significant. For this reason, the sensitivity analysis is limited to the cooling stage.

Decreasing Young's modulus (Figure 18b) of the substrate by 20% of its reference value gives a strong deviation of the predicted Z displacement. Note that decreasing the Young's modulus of both materials simultaneously produces similar effect than the variation of the substrate only. The latter result gives the conclusion that almost no sensitivity effect of the clad elastic property on the vertical displacement of the sample is found, which is expected due to the relative strength of the bar (volume of $8 \times 10 \times 120 \text{ mm}^3$) compared to the thin wall (volume of $4.0 \times 1.5 \times 40 \text{ mm}^3$ with similar Young's modulus). When decreasing the yield stress, it is observed that the substrate is the main contributor to the observed displacement, with the clad having, comparatively a small impact. In this case, a decrease of yield stress leads to a smaller elastic region which apparently has a major role on the displacements.

Figure 19 provides a summary of the sensitivity analysis. Thermal capacity, conductivity and power deviations affecting thermal history of substrate immediately close to cladding zone (TC2) are shown in a radar graph as an average value for the cladding stage (60 to 150 seconds). The values are the normalized difference between results computed with the $\pm 20\%$ variation of parameters and the results computed with the reference parameters. Average deviation values of the sensitivity analysis of Young's modulus and yield stress affecting deflexion (vertical displacement due to thermal history) are considering the clad and the substrate variation (curves called 'both' in Figure 18) in the range between 150 and 500 seconds. Figure 19 visually shows the main conclusions drawn from each sensitivity analysis: i) thermal history is more sensitive to positive and negative variations of power, thermal capacity and conductivity, with a decreasing influence in this order; ii) deflections are more sensitive to Young's modulus than yield stress.

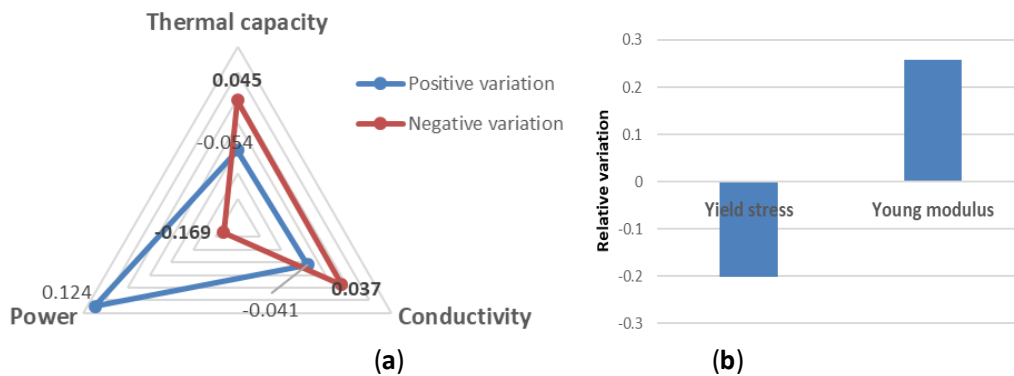


(a)



(b)

Figure 18. (a) Correlation between measured and predicted vertical displacements (- down, + up) during the cladding process, including the preheating and cooling stages. (b) Sensitivity analysis in the cooling stage to negative variations of Young's modulus (E) and the elastic limit (S_y) of the clad and the substrate.



(a)

(b)

Figure 19. Summary of sensitivity analysis, expressed as the relative variation with respect to the reference case. (a) Thermal history sensitivity of the cladded sample with $\pm 20\%$ variations of thermal capacity, conductivity, and power. (b) Deflection sensitivity with -20% variation of Young's modulus and -20% of yield stress.

5. Conclusions

The identification and the validation of a thermo-mechanical finite element model as well as the simulation analysis of a ten layer DED thin wall M4 steel part deposited on a 42CrMo4 steel substrate were presented. Distortion and temperature measurements of the substrate were used for model validation and sensitivity analysis. The result analysis emphasizes the following points:

- Predicted thermal history can successfully explain SEM and OM observations of solidified microstructure showing variation from the first to the tenth layer of the thin wall;
- From the thermal point of view, the most influential factor is laser power, followed by thermal capacity and finally thermal conductivity;
- Deflection of the substrate during the process is more sensitive to Young's modulus than to yield stress;

M4 steel needs pre-heating in DED process and presents solid phase transformations (bainite, martensite) sensitive to temperature rate, as well as carbide formations that modify austenite composition and martensite temperature start (variation can be higher than 80 °C). The accurate thermo-mechanical cladding simulation of this material is still a challenge as accurate data on transformation kinetics and associated thermal dilatation curves are still missing as well as accurate thermal and phase dependent Young's modulus.

Due to the multiple uncertainties, a deep learning approach is currently investigated in addition to complementary material characterizations to improve the FE model and its set of material parameters. The final research goal is to determine the optimal process conditions that generate samples with low residual stresses and a homogeneous material. This last feature can be expected through a constant size of the melt pool for each clad layer.

Author Contributions: Simulations, Validation, Formal Analysis, Investigation, Data Curation, Writing—Original Draft Preparation, Writing—Review & Editing, R.T.J and A.M.H.; Writing—review & editing, Formal Analysis, Writing—Original Draft Preparation V.T; Software Developments, H.S.T; Project Administration, AMH; Experiment, R.C.; Analysis of Experimental Results and Simulation Assumptions, N.H, A.M and J.T; Conceptualization and Methodology A.M.H and L.D., Thermo-Physical Properties, N.H.

Funding: by the FNRS F.R.S. [PDR T.0039.14] Grant, Lasercladding.

Acknowledgments: As Research Director of FRS-FNRS, AM Habraken acknowledges the support of this institution. CARE μ of ULiège is thanked for providing SEM/EDS facilities. Computational resources are provided by the Consortium des Équipements de Calcul Intensif (CÉCI) funded by the F.R.S.-FNRS. V. Tuninetti acknowledges the National Agency for Research and Development (ANID) Fondecyt project n° 11170002 for financial support. The authors also acknowledge Olivier Dedry for providing additional thermo-physical properties data and Héléne Morch for the improvement of the optimisation method.

Conflicts of Interest: The authors declare no conflict of interest.

Appendix. Measured thermo-physical properties

Table A1. Thermo-physical properties for M4 HSS material obtained by DED process.

T (°C)	ρ (kg/m ³) density	c_p (J/kg.°C) thermal capacity	α ($\times 10^{-6}$ m ² /s) diffusivity	k (W/m.°C) conductivity
20	7950	460	5.11	18.57
100	7930	440	5.26	18.42
200	7900	430	5.44	18.67
300	7870	440	5.45	18.72
400	7840	460	5.34	19.22
500	7810	480	5.20	19.40
600	7780	490	4.93	18.79
700	7740	520	4.15	16.63
800	7720	610	4.56	21.37
900	7720	640	5.79	28.45
1000	7690	550	6.00	25.22
1100	7640	600	6.09	27.99

Table A2. Thermal expansion coefficient for M4 HSS material obtained by DED process.

T (°C)	Thermal expansion coefficient (1/°C)
0	5.00E-06
50	1.00E-06
100	-6.31E-06
150	-1.26E-05
200	-2.71E-05
226	-3.48E-05
250	1.35E-05
300	1.61E-05
350	1.63E-05
400	1.57E-05
450	1.60E-05
500	1.53E-05
550	1.56E-05
600	1.62E-05

650	1.68E-05
700	1.70E-05
750	1.68E-05
800	1.69E-05
850	1.76E-05
900	1.73E-05
950	1.74E-05
1000	1.76E-05
1050	1.81E-05
1100	1.87E-05
1150	1.94E-05

Table A3. Thermo-physical properties for 42CrMo4 material measured on one substrate bar.

T (°C)	ρ (kg/m ³) density	c_p (J/kg·°C) thermal capacity	α ($\times 10^{-6}$ m ² /s) diffusivity	k (W/m·°C) conductivity
25	7837.35	466.98	1.31E-05	47.81
50	7831.67	466.98	1.31E-05	47.81
100	7820.21	466.98	1.31E-05	47.81
150	7807.06	492.06	1.21E-05	46.54
200	7792.57	506.23	1.15E-05	45.26
250	7776.97	521.35	1.09E-05	44.12
300	7760.52	536.19	1.03E-05	42.98
350	7743.46	555.36	9.68E-06	41.61
400	7726.21	575.08	9.06E-06	40.24
450	7709.08	595.65	8.48E-06	38.96
500	7691.97	618.84	7.91E-06	37.67
550	7674.64	647.56	7.05E-06	35.05
600	7657.67	683.13	6.20E-06	32.43
650	7641.01	738.98	4.91E-06	27.71
700	7625.51	813.04	3.71E-06	23.00
750	7613.34	977.68	3.22E-06	23.98
800	7651.66	741.52	4.40E-06	24.97
850	7626.32	573.87	5.63E-06	24.63
900	7602.27	562.42	5.68E-06	24.30

950	7579.89	560.42	5.81E-06	24.67
1000	7558.22	574.11	5.77E-06	25.05
1050	7536.83	571.96	6.01E-06	25.90
1100	7513.93	585.96	6.07E-06	26.74
1477	7513.93	585.96	6.07E-06	26.74
1480	7513.93	3557.1	1.00E-06	26.74
1500	7513.93	3557.1	1.00E-06	26.74
1503	7513.93	585.96	6.07E-06	26.74

Table A4. Thermal expansion coefficient for 42CrMo4 material measured on one substrate bar.

T (°C)	Thermal expansion coefficient (1/°C)
26.85	1.24E-05
126.85	1.34E-05
226.85	1.43E-05
326.85	1.48E-05
426.85	1.53E-05
526.85	1.59E-05
626.85	1.64E-05
686.85	1.00E-05
726.85	1.58E-05
826.85	2.27E-05
926.85	2.34E-05
1026.85	2.40E-05
1126.85	2.42E-05

References

1. Gibson, I.; Rosen, D.; Stucker, B. *Additive Manufacturing Technologies*; Springer New York: New York, 2015.
2. Graf, B.; Ammer, S.; Gumenyuk, A.; Rethmeier, M. Design of experiments for laser metal deposition in maintenance, repair and overhaul applications. *Procedia CIRP* **2013**, *11*, 245–248.
3. Pinkerton, A.J.; Wang, W.; Li, L. Component repair using laser direct metal deposition. *Proc. Inst. Mech. Eng. Part B J. Eng. Manuf.* **2008**, *222*, 827–836.
4. Hascoët, J.-Y.; Touzé, S.; Rauch, M. Automated identification of defect geometry for metallic part repair by an additive manufacturing process. *Weld. World* **2018**, *62*, 229–241.

5. Bonnard, R.; Hascoët, J.-Y.; Mognol, P. Data model for additive manufacturing digital thread: state of the art and perspectives. *Int. J. Comput. Integr. Manuf.* **2019**, *32*, 1170–1191.
6. Muller, P.; Mognol, P.; Hascoët, J.-Y. Modeling and control of a direct laser powder deposition process for Functionally Graded Materials (FGM) parts manufacturing. *J. Mater. Process. Technol.* **2013**, *213*, 685–692.
7. Graf, M.; Hälsig, A.; Höfer, K.; Awiszus, B.; Mayr, P. Thermo-Mechanical Modelling of Wire-Arc Additive Manufacturing (WAAM) of Semi-Finished Products. *Metals (Basel)*. **2018**, *8*, 1009.
8. Kiran, A.; Hodek, J.; Vavřík, J.; Urbánek, M.; Džugan, J. Numerical Simulation Development and Computational Optimization for Directed Energy Deposition Additive Manufacturing Process. *Materials* **2020**, *13*, 2666.
9. Wang, B.; Yang, G.; Zhou, S.; Cui, C.; Qin, L. Effects of On-Line Vortex Cooling on the Microstructure and Mechanical Properties of Wire Arc Additively Manufactured Al-Mg Alloy. *Metals (Basel)*. **2020**, *10*, 1004.
10. Aldalur, E.; Veiga, F.; Suárez, A.; Bilbao, J.; Lamikiz, A. Analysis of the wall geometry with different strategies for high deposition wire arc additive manufacturing of mild steel. *Metals (Basel)*. **2020**.
11. Pinkerton, A.J. Advances in the modeling of laser direct metal deposition. *J. Laser Appl.* **2015**, *27*, S15001.
12. Khairallah, S.A.; Anderson, A.T.; Rubenchik, A.; King, W.E. Laser powder-bed fusion additive manufacturing: Physics of complex melt flow and formation mechanisms of pores, spatter, and denudation zones. *Acta Mater.* **2016**, *108*, 36–45.
13. Heeling, T.; Cloots, M.; Wegener, K. Melt pool simulation for the evaluation of process parameters in selective laser melting. *Addit. Manuf.* **2017**, *14*, 116–125.
14. Pinomaa, T.; Provatas, N. Quantitative phase field modeling of solute trapping and continuous growth kinetics in quasi-rapid solidification. *Acta Mater.* **2019**, *168*, 167–177.
15. Touzé, S. Laser metal deposition of aluminum-copper alloys for repair applications. PhD Thesis, Centrale Nantes, France, 15th Sept. 2019.
16. Jardin, R.T.; Tchoufang Tchoundjang, J.; Duchêne, L.; Tran, H.-S.; Hashemi, N.; Carrus, R.; Mertens, A.; Habraken, A.M. Thermal histories and microstructures in Direct Energy Deposition of a High Speed Steel thick deposit. *Mater. Lett.* **2019**, *236*, 42–45.
17. Delahaye, J.; Tchoundjang, J.T.; Lecomte-Beckers, J.; Rigo, O.; Habraken, A.M.; Mertens, A. Influence of Si precipitates on fracture mechanisms of AlSi10Mg parts processed by Selective Laser Melting. *Acta Mater.* **2019**, *175*, 160–170.
18. Setien, I.; Chiumenti, M.; van der Veen, S.; San Sebastian, M.; Garciandía, F.; Echeverría, A. Empirical methodology to determine inherent strains in additive manufacturing. *Comput. Math. with Appl.* **2019**, *78*, 2282–2295.
19. Yang, Q.; Zhang, P.; Cheng, L.; Min, Z.; Chyu, M.; To, A.C. Finite element modeling and validation of thermomechanical behavior of Ti-6Al-4V in directed energy deposition additive manufacturing. *Addit. Manuf.* **2016**, *12*, 169–177.
20. Patil, R.B.; Yadava, V. Finite element analysis of temperature distribution in single metallic powder layer during metal laser sintering. *Int. J. Mach. Tools Manuf.* **2007**, *47*, 1069–1080.

21. Yin, J.; Zhu, H.; Ke, L.; Lei, W.; Dai, C.; Zuo, D. Simulation of temperature distribution in single metallic powder layer for laser micro-sintering. *Comput. Mater. Sci.* **2012**, *53*, 333–339.
22. Chiumenti, M.; Lin, X.; Cervera, M.; Lei, W.; Zheng, Y.; Huang, W. Numerical simulation and experimental calibration of additive manufacturing by blown powder technology. Part I: thermal analysis. *Rapid Prototyp. J.* **2017**, *23*, 448–463.
23. Ye, R.; Smugeresky, J.E.; Zheng, B.; Zhou, Y.; Lavernia, E.J. Numerical modeling of the thermal behavior during the LENS® process. *Mater. Sci. Eng. A* **2006**, *428*, 47–53.
24. He, X.; Yu, G.; Mazumder, J. Temperature and composition profile during double-track laser cladding of H13 tool steel. *J. Phys. D. Appl. Phys.* **2010**, *43*, 015502.
25. Heigel, J.C.; Michaleris, P.; Reutzel, E.W. Thermo-mechanical model development and validation of directed energy deposition additive manufacturing of Ti–6Al–4V. *Addit. Manuf.* **2015**, *5*, 9–19.
26. Goldak, J.; Chakravarti, A.; Bibby, M. A new finite element model for welding heat sources. *Metall. Trans. B* **1984**, *15*, 299–305.
27. Yang, J.; Sun, S.; Brandt, M.; Yan, W. Experimental investigation and 3D finite element prediction of the heat affected zone during laser assisted machining of Ti6Al4V alloy. *J. Mater. Process. Technol.* **2010**, *210*, 2215–2222.
28. Tran, H.-S.; Tchuindjang, J.T.; Paydas, H.; Mertens, A.; Jardin, R.T.; Duchêne, L.; Carrus, R.; Lecomte-Beckers, J.; Habraken, A.M. 3D thermal finite element analysis of laser cladding processed Ti-6Al-4V part with microstructural correlations. *Mater. Des.* **2017**, *128*, 130–142.
29. Lindgren, L.-E.; Lundbäck, A.; Fisk, M.; Pederson, R.; Andersson, J. Simulation of additive manufacturing using coupled constitutive and microstructure models. *Addit. Manuf.* **2016**, *12*, 144–158.
30. Caiazzo, F.; Alfieri, V. Simulation of Laser-assisted Directed Energy Deposition of Aluminum Powder: Prediction of Geometry and Temperature Evolution. *Materials (Basel)*. **2019**, *12*, 2100.
31. Lu, X.; Lin, X.; Chiumenti, M.; Cervera, M.; Li, J.; Ma, L.; Wei, L.; Hu, Y.; Huang, W. Finite element analysis and experimental validation of the thermomechanical behavior in laser solid forming of Ti-6Al-4V. *Addit. Manuf.* **2018**, *21*, 30–40.
32. Shim, D.-S.; Baek, G.-Y.; Lee, E.-M. Effect of substrate preheating by induction heater on direct energy deposition of AISI M4 powder. *Mater. Sci. Eng. A* **2017**, *682*, 550–562.
33. Hashemi, N.; Mertens, A.; Montrieux, H.-M.; Tchuindjang, J.T.; Dedry, O.; Carrus, R.; Lecomte-Beckers, J. Oxidative wear behaviour of laser clad High Speed Steel thick deposits: Influence of sliding speed, carbide type and morphology. *Surf. Coatings Technol.* **2017**, *315*, 519–529.
34. Pineda Huitron, R.M.; Ramirez Lopez, P.E.; Vuorinen, E.; Jentner, R.; Kärkkäinen, M.E. Converging criteria to characterize crack susceptibility in a micro-alloyed steel during continuous casting. *Mater. Sci. Eng. A* **2020**, *772*, 138691.
35. Wang, S.-H.; Chen, J.-Y.; Xue, L. A study of the abrasive wear behaviour of laser-clad tool steel coatings. *Surf. Coatings Technol.* **2006**, *200*, 3446–3458.
36. Leunda, J.; Soriano, C.; Sanz, C.; Navas, V.G. Laser Cladding of Vanadium-Carbide Tool Steels for Die Repair. *Phys. Procedia* **2011**, *12*, 345–352.

37. Rahman, N.Ur; Capuano, L.; Cabeza, S.; Feinaeugle, M.; Garcia-Junceda, A.; de Rooij, M.B.; Matthews, D.T.A.; Walmag, G.; Gibson, I.; Römer, G.R.B.E. Directed energy deposition and characterization of high-carbon high speed steels. *Addit. Manuf.* **2019**, *30*,100838.
38. Pascon, F.; Cescotto, S.; Habraken, A.M. A 2.5D finite element model for bending and straightening in continuous casting of steel slabs. *Int. J. Numer. Methods Eng.* **2006**, *68*, 125–149.
39. Neira Torres, I.; Gilles, G.; Tchoufang Tchuindjang, J.; Flores, P.; Lecomte-Beckers, J.; Habraken, A.M. FE modeling of the cooling and tempering steps of bimetallic rolling mill rolls. *Int. J. Mater. Form.* **2017**, *10*, 287–305.
40. Guzmán, C.F.; Gu, J.; Duflou, J.; Vanhove, H.; Flores, P.; Habraken, A.M. Study of the geometrical inaccuracy on a SPIF two-slope pyramid by finite element simulations. *Int. J. Solids Struct.* **2012**, *49*, 3594–3604.
41. Mukherjee, T.; Zhang, W.; DebRoy, T. An improved prediction of residual stresses and distortion in additive manufacturing. *Comput. Mater. Sci.* **2017**, *126*, 360–372.
42. Chew, Y.; Pang, J.H.L.; Bi, G.; Song, B. Thermo-mechanical model for simulating laser cladding induced residual stresses with single and multiple clad beads. *J. Mater. Process. Technol.* **2015**, *224*, 89–101.
43. Zhu, Y.Y.; Cescotto, S. Unified and mixed formulation of the 8-node hexahedral elements by assumed strain method. *Comput. Methods Appl. Mech. Eng.* **1996**, *129*, 177–209.
44. Belytschko, T.; Bindeman, L.P. Assumed strain stabilization of the 4-node quadrilateral with 1-point quadrature for nonlinear problems. *Comput. Methods Appl. Mech. Eng.* **1991**, *88*, 311–340.
45. Duchêne, L.; El Houdaigui, F.; Habraken, A.M. Length changes and texture prediction during free end torsion test of copper bars with FEM and remeshing techniques. *Int. J. Plast.* **2007**, *23*, 1417–1438.
46. Simo, J.C.; Hughes, T.J.R. On the Variational Foundations of Assumed Strain Methods. *J. Appl. Mech.* **1986**, *53*, 51–54.
47. Cao, J.; Gharghoury, M.A.; Nash, P. Finite-element analysis and experimental validation of thermal residual stress and distortion in electron beam additive manufactured Ti-6Al-4V build plates. *J. Mater. Process. Technol.* **2016**.
48. Bi, G.; Gasser, A.; Wissenbach, K.; Drenker, A.; Poprawe, R. Identification and qualification of temperature signal for monitoring and control in laser cladding. *Opt. Lasers Eng.* **2006**, *44*, 1348–1359.
49. Lampa, C.; Kaplan, A.F.H.; Powell, J.; Magnusson, C. An analytical thermodynamic model of laser welding. *J. Phys. D. Appl. Phys.* **1997**, *30*, 1293–1299.
50. Neela, V.; De, A. Three-dimensional heat transfer analysis of LENSTM process using finite element method. *Int. J. Adv. Manuf. Technol.* **2009**, *45*, 935–943.
51. Deng, D.; Kiyoshima, S. FEM prediction of welding residual stresses in a SUS304 girth-welded pipe with emphasis on stress distribution near weld start/end location. *Comput. Mater. Sci.* **2010**, *50*, 612–621.
52. Liang, W.; Murakawa, H.; Deng, D. Investigation of welding residual stress distribution in a thick-plate joint with an emphasis on the features near weld end-start. *Mater. Des.* **2015**, *67*, 303–312.
53. Denlinger, E.R.; Michaleris, P. Effect of stress relaxation on distortion in additive manufacturing process modeling. *Addit. Manuf.* **2016**, *12*, 51–59.

54. Lu, X.; Lin, X.; Chiumenti, M.; Cervera, M.; Hu, Y.; Ji, X.; Ma, L.; Huang, W. In situ measurements and thermo-mechanical simulation of Ti-6Al-4V laser solid forming processes. *Int. J. Mech. Sci.* **2019**, *153–154*, 119–130.
55. Lu, X.; Lin, X.; Chiumenti, M.; Cervera, M.; Hu, Y.; Ji, X.; Ma, L.; Yang, H.; Huang, W. Residual stress and distortion of rectangular and S-shaped Ti-6Al-4V parts by Directed Energy Deposition: Modelling and experimental calibration. *Addit. Manuf.* **2019**, *26*, 166–179.
56. Gockel, J.; Beuth, J.; Tamingier, K. Integrated control of solidification microstructure and melt pool dimensions in electron beam wire feed additive manufacturing of Ti-6Al-4V. *Addit. Manuf.* **2014**, *1–4*, 119–126.
57. Fachinotti, V.D.; Cardona, A.; Baufeld, B.; Van der Biest, O. Finite-element modelling of heat transfer in shaped metal deposition and experimental validation. *Acta Mater.* **2012**, *60*, 6621–6630.
58. Romano, J.; Ladani, L.; Razmi, J.; Sadowski, M. Temperature distribution and melt geometry in laser and electron-beam melting processes – A comparison among common materials. *Addit. Manuf.* **2015**, *8*, 1–11.
59. CTSPM, 2020. M4 PM catalogue, Cincinnati Tool Steel Company Inc., Illinois, USA. http://cintool.com/documents/Powdered_Metal/M4PM.pdf (last accessed Jun 9th, 2020).
60. Jiangyou, 2020. Data table for GS-42CrMo4. Jiangyou Longhai Special Steel Co., China. <http://www.steelgr.com/Steel-Grades/Mould-Steel/gs-42crmo4.html> (last accessed June 9th, 2020).
61. ABRAMS, 2020. Technical guide: AFNOR 42CD4, Abrams Engineering Services GmbH & Co. KG, Osnabrück, Germany. <http://www.aciers-premium.fr/images/filedownloads/fichestechniques/42CD4.pdf> (last accessed Jun 9th, 2020)
62. Tuninetti, V.; Flores, P.; Valenzuela, M.; Pincheira, G.; Medina, C.; Duchêne, L.; Habraken, A.-M. Experimental characterization of the compressive mechanical behaviour of Ti6Al4V alloy at constant strain rates over the full elastoplastic range. *Int. J. Mater. Form.* **2020**, *13*, 709–724.
63. Habraken, A.M.; Bouffioux, C. Simulation des changements de phases lors de la trempe d'un anneau Analyse thermique, mécanique, métallurgique CFR – Acier 42CD4. Technical report 57 Region Walloon project – Caractérisation rationnelle des propriétés à chaud des matériaux métalliques. Convention N° 981/3793, September **2003**.
64. Hashemi, N. Study of high speed steel deposits produced by laser cladding, microstructure – wear – thermal model, PhD Thesis, University of Liège, 8th Sept. 2017.



© 2020 by the authors. Submitted for possible open access publication under the terms and conditions of the Creative Commons Attribution (CC BY) license (<http://creativecommons.org/licenses/by/4.0/>).

Chapter 4

The current work⁴ seamlessly extends the research conducted in Chapter 2. Our earlier thermal model highlighted the direct influence of thermal history on microstructure. While a constant laser power strategy was shown to yield a non-uniform microstructure throughout the material depth, the focus of our current work shifts to exploring a variable laser power strategy capable of achieving specific, desired microstructures at varying depths within the bulk sample.

Throughout this study, we uncovered a crucial insight: the melt pool size exerts a profound influence on the number of remelting events, thereby directly affecting the resulting microstructure. To optimize laser power with the goal of attaining a desired melt pool size, we harnessed the Newton-Raphson iterative method, an old fashion but powerful tool in our research arsenal. Note that Pham (Pham 2023)⁵ has investigated the same problem with a robust optimization method (the word robust meaning for data science scientists taking into account uncertainties) based on the extensive use of a surrogate model developed by a Feed Forward Neural Network approach. Pham's numerical result demonstrates that the simple Newton Raphson and Pham's advanced optimization frame reach close optimal laser function curves. The functions of the present research were the ones implemented in real experiments (samples P767 and P768). As demonstrated in the following article, they enhance the sample homogeneity through the sample depth.

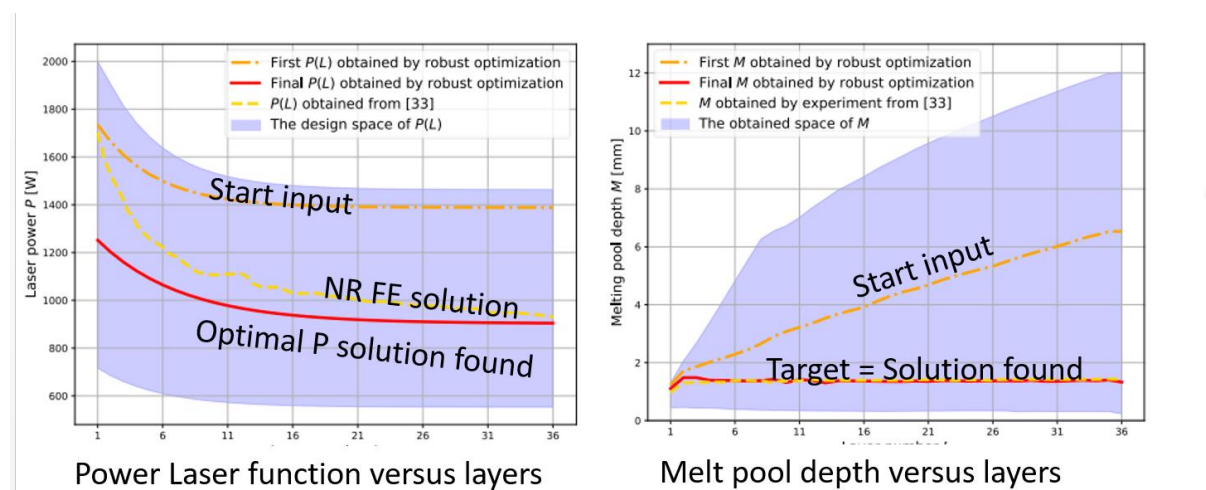


Figure 24 - Comparison of the laser power function LPF_2 found by Newton Raphson (NR) in this research and the result of the robust optimization where the constant melt pool and an energy minimization define the objective function (Pham 2023). The start input information is associated with Pham's work.

⁴ Published in Optics and Laser Technology, volume 163, 2023, 109426

⁵ T.Q.D. Pham, T.V. Hoang, X.V. Tran, Seifallah Fetni, L. Duchêne, H.S. Tran, A.M. Habraken, A framework for the robust optimization under uncertainty in additive manufacturing, Journal of Manufacturing Processes, Volume 103, 2023, Pages 53-63, ISSN 1526-6125, <https://doi.org/10.1016/j.jmapro.2023.08.009>.

Our investigation delved into the mechanical properties of the samples, employing both microhardness and nanoindentation techniques. Microhardness assessments revealed that samples produced using the optimized variable laser power strategy exhibited greater homogeneity in hardness throughout the material's depth when compared to those produced with a constant laser power approach. On the other hand, the nanoindentation hardness map yielded intriguing results that warrant further analysis. This includes conducting simulations with Computational Fluid Dynamics software at the melt pool level. Indeed within our solid FE element approach a finer mesh will not gain deeper insights into the accurate thermal history across the melt pool thickness. The events related to convection such as Marangoni effect within a liquid are out of range here. For this work, samples P766, P767 and P768 were used for CP (constant power), LPF1 (laser power function) and LPF2 configurations respectively.

Optimizing laser power of directed energy deposition process for homogeneous AISI M4 steel microstructure

Rúben Tome Jardin ¹, Víctor Tuninetti ^{2,*}, Jérôme Tchoufang Tchoundjang ³, Laurent Duchêne ¹, Neda Hashemi ³, Hoang Son Tran ¹, Raoul Carrus ⁴, Anne Mertens ³, Anne Marie Habraken ^{1,5,*}

¹ Department ArGEnCo-MSM, University of Liège, Liège 4000, Belgium

² Department of Mechanical Engineering, Universidad de La Frontera, Temuco 4780000, Chile

³ Department A&M-MMS, University of Liège, Liège 4000, Belgium

⁴ SIRRIS Research Centre (Liège), Seraing 4102, Belgium

⁵ Fonds de la Recherche Scientifique-F.R.S.-F.N.R.S., Brussels 1000, Belgium

* Corresponding authors: victor.tuninetti@ufrontera.cl (V.T.); anne.habraken@uliege.be (A.M.H.);

Tel.: +56452325984 (V.T.); +32496607945 (A.M.H.)

Abstract

A finite element model of directed energy deposition (DED) process predicts the thermal history during the manufacturing of high speed steel cuboid samples. The simulation result validation relies on comparisons between measured and predicted data such as temperature histories within the substrate and the melt pool depth of the last coating layer. Integrated within an optimization loop, these DED simulations identify two variable laser power functions able to generate a constant melt pool size. These functions are expected to provide a homogeneous microstructure over layers. The computed thermal fields and the microstructure generated by three AISI M4 experiments performed with the constant laser power case and the two optimized functions at three points of interest located at different depths within the deposit are correlated. The effect of the melt superheating temperature and the thermal cyclic history on micro and nanohardness measurements is observed. As a result, the optimized laser power functions provide samples with more homogeneous microhardness than the constant laser power function, however, the homogeneity of microstructure is not fully confirmed by the nanohardness map throughout the deposited M4 steel layers.

Keywords: Finite element modeling; Numerical optimization; Additive manufacturing; Directed energy deposition; Melt pool size; Nanohardness map.

1. Introduction

To overcome the challenges related to increasing carbon emissions, noise and energy consumption in air transportation product development and related manufacturing industry, additive manufacturing (AM) processes are considered one of the best emerging technologies contributing to the fourth industrial revolution. The different AM technologies produce components with special or complex metal alloys, flexible and functional designs, and consequently light weight [1–5]. In addition, the associated AM repair technology also contributes to increase service life by recovering damaged components [6].

The two main known groups of AM technologies are directed energy deposition (DED) [7–14] and powder bed fusion (PBF) processes [15–19]. Some advantages of DED process over PBF (laser (L-PBF) or electron beam (EB-PBF)) are their high versatility and controllability, increased build rates and volumes, and lower material powder required [20]. PBF processes generally allow building high resolution parts [21]; while DED processes are generally suitable for near net shape products, clad parts operating in extreme conditions, and repaired high-valued components [6,22]. The current study is focused on improving DED part quality by optimizing the laser power function thanks to 2D finite element (FE) simulations. The optimal laser power functions identified are expected to produce parts with improved homogeneity, which will be evaluated at the microscopic level by Vickers profiles and nanoindentation mapping.

AISI M4 high speed steel grade shows a high potential of wear properties (Fig. 1). The AISI M4 wear behavior of DED samples is strongly related to the size and the distribution of both vanadium-rich MC carbides and molybdenum-rich M₂C carbides present at cell boundaries. This statement is confirmed in Hashemi et al. [23], which compares the wear behavior of different high speed steel grades (DED cuboid deposits of 30-35 mm square and 20-25 mm high versus cast samples). DED ultrafine and cellular-type microstructures (Fig. 2(a) and 2(b)) containing rounded shape M₂C carbides lead to low wear rates (see Fig. 2) compared to coarser microstructures (note the different image scale) obtained under conventional casting route (Fig. 1(c)). This cast image contains both large MC carbides inside grains and acicular M₂C carbides at grain boundaries. In addition, the top layer within DED sample has a slightly finer microstructure than the core layer as mentioned in the previous work of Jardin et al. [24]. This fact could explain why the wear rate is also slightly lower close to the DED surface compared to the bulk for DED samples at low sliding speed but does not justify the higher wear rate for higher sliding speed. Nevertheless, the wear rate within DED samples is clearly less sensitive to sliding speed compared to conventional casting, regardless of the location within the thick deposit. This fact points a higher homogeneity within the structure at a macro scale for DED samples, while the non-constant wear properties with the height location still suggests a heterogeneity of the microstructure that could be improved.

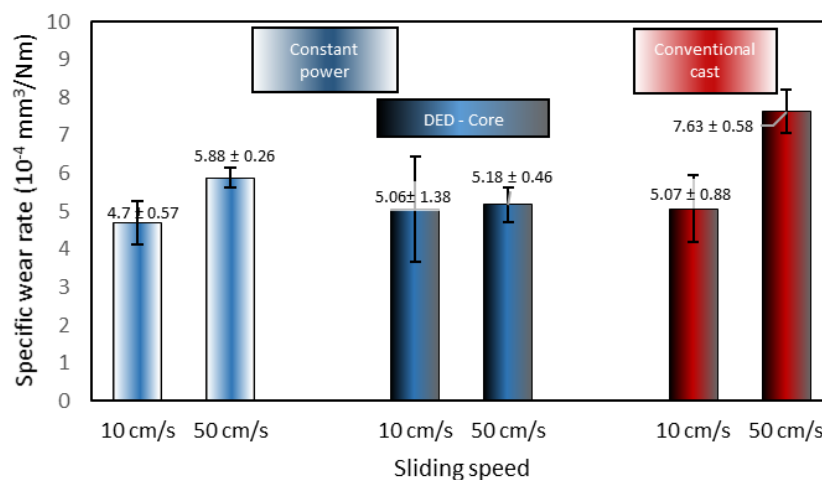


Fig. 1. Wear properties of AISI M4 DED and casted samples under two different sliding speeds and for DED, at the sample surface associated with the last deposit layer and in the core sample.

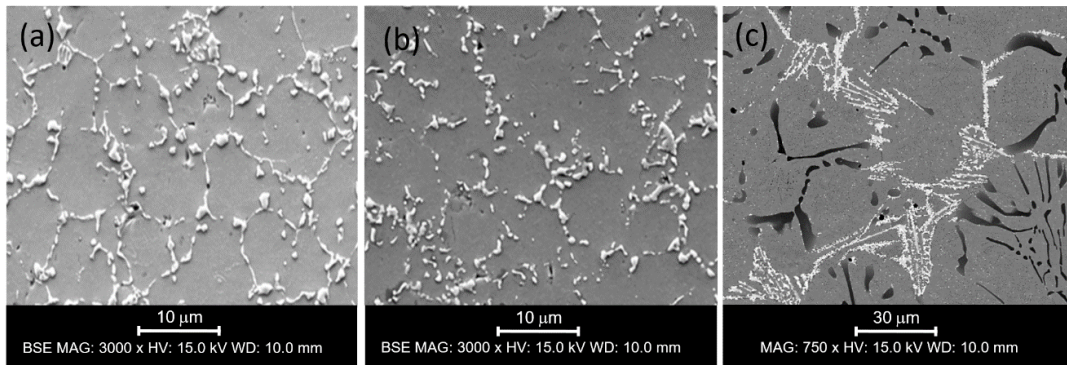


Fig. 2. SEM micrographs (BSE) show the ultrafine and cellular-type microstructures of DED AISI M4 sample manufactured with a constant laser power, (a) near the surface (within top layer), (b) at the sample mid height, and (c) BSE images of the coarse microstructure of a conventional cast sample (note the lower magnification of c image versus a and b ones).

The homogeneity issues within DED samples is not new. For instance, Shim et al. [7] developed a process diagram to relate the single-layer height to the specific energy density and the powder feed density in order to improve geometric accuracy and mechanical properties of the final part of high-speed-tool steel AISI M4. Their results concluded that a time-varying energy supplied to the melting zone affects the cooling rate and the solidification rate of the deposited layers, resulting in an inhomogeneous micro-hardness throughout the deposited region. The non-uniform micro-hardness was explained by variation in the grain size and the martensite fraction at each location of the deposited region, caused by the history of the energy input in the material. It indeed generates a non-uniform solidification rate of the AISI M4 steel. In addition, Shim et al. [25] studied the effect of substrate preheating by induction heater on DED AISI M4 powder. Their results indicated that the process parameters such as laser power, powder feed rate, and induction energy should be cautiously designed to limit the melting pool rise, which resulted in an over-deposition leading to a dimensional error.

Note that the microstructure heterogeneity is not the single peculiarity observed in DED samples. Within additive parts, there are also for instance uncontrolled voids, micro-cracks, part distortions and surface roughness [26–28] which are not present in wrought materials [26,29,30]. Among the numerous process parameters conditioning the feasibility of a DED part are the laser power and spot size, powder flow and composition, scanning speed, working distance, hatch spacing and overlap, scanning and slice strategy. To increase the part quality, online process monitoring and control have been applied to vary the temperature of the melt pool, its size, the deposition thickness and the powder flow. For instance, Su et al. [31] proposed a closed-loop control method based on the proportional integration algorithm (PID) to enhance the wear resistance by tuning and controlling in real time the laser power and molten pool size. Closed-loop melt pool size reduction control affects the cooling rate, promotes phase transformation and grain refinement, consequently increasing the deposited part strength [32]. Cong and Ning [33] proposed an ultrasonic vibration for the DED process to reduce voids and cracks, achieving improved geometrical and microstructural characteristics, and consequently higher mechanical resistance in stainless steel parts. Park et al. [34] developed a real-time Poisson's ratio and Young's modulus estimation technique for the DED process using femtosecond laser ultrasound. For process repeatability, quality measurement of the nozzle geometry variation during service life due to scouring erosion of the inner channel in contact with the high-speed powder particles must be considered as reported by Tan et al. [35]. The complexity of obtaining accurate geometry has been reported

by Peng et al. [36], while other researchers have been focused on the path strategies effecting the properties and the geometrical dimensions of the manufactured parts. Woo et al. [37] examined the through thickness microstructure, the thermal and mechanical properties, and the residual stresses of a DED functionally graded steel (FGM) specimens finding an equiaxed grain structure created by the epitaxial grain growth along the building direction with a maximum significant variation of 950 MPa of residual stresses. The stresses were released to about 430 MPa when the FGM were manufactured with orthogonal or island (chessboard) interlayers scanning strategies. In Biegler et al. [38], two different path-planning strategies for AISI 316L bulky parts such as the contour-parallel and the zig-zag were compared. The characteristic errors observed at curved and narrow areas for the zig-zag strategy and at sharp angles for the contour-parallel strategy demonstrated that the performance of path is highly geometry dependent.

In addition to the tools and techniques developed to improve the quality of DED process listed here above, numerous experimental and numerical researches have been specifically conducted on the links between thermomechanical properties, process parameters and microstructure features of the deposited material [26,39–42]. For Ti6Al4V material, in Lu et al. [43] the microhardness and tensile property of the specimens obtained by DED were significantly improved by the interlayer laser shot peening treatment, reaching properties equivalent to those found in raw Ti-6Al-4V [44]. Razavi et al. [26] pointed the higher cycle fatigue strength in DED versus forged samples, with differences attributed to grain size. In Tran et al. [40], a correlation between the microstructure and the temperature evolution was obtained from finite element thermal simulations of DED process of Ti6Al4V alloy. While for steels produced by DED process, Guan et al. [45] characterized the effect of the laser incident energy on the morphology of microstructures of 12CrNi2Y alloy steel. Bertsch et al. [46] found that thermal distortions during additively manufacturing of austenitic stainless steel 316L are the primary reason of the dislocation structures, which are dependent on the constraints surrounding the melt pool and the thermal cycling.

Finally, according to the state of the art presented in C. Wang et al. [20], additive manufacturing coupled with machine learning can improve the development of new high-performance materials, thanks to the optimization of topological designs or process parameters, as well as the analysis of on line process for defect monitoring. Zhang et al. [47] applied two machine learning algorithms to predict melting pool temperature in a DED process with high accuracy. However as pointed by Pham et al. [48,49] an accurate deep learning strategy requires significant experimental data or validated finite element simulation results of the process to generate accurate predictions. In Pham et al. [48], a simple FFNN architecture was applied to model DED manufacturing of AISI M4 samples. The developed surrogate model was 180 times quicker than a FE simulation and it allowed to perform an uncertainty quantification and sensitivity analysis of M4 DED sample manufacturing process. The results confirmed that convection, laser power, scanning speed, and conductivity induce the most uncertainties in melting pool sizes [49].

Based on previous literature review, it is clear that the most relevant process parameters concerning the heat input are laser power, powder flow rate, scanning speed and spot size. In the current research, the aforementioned parameters were first kept constant in the manufacturing of DED cuboid sample manufactured from M4 steel powder. It allowed validating the FE predicted thermal field history versus the temperature measured at the local points [24]. The fact that the melt pool size is highly sensitive to the laser power function

explains why the current article is focused on this process parameter. Indeed, the solidification process determines the microstructure which controls the material properties. A constant melt pool size should provide constant homogeneous material properties if no further external parameters disturb the system. Hereafter, an optimization loop varies the laser power to achieve a homogeneous microstructure thanks to a constant melt pool size. M4 bulk parts manufactured by DED with constant and optimized laser power functions are compared. To validate the proposed methodology to reach a homogeneous microstructure, nano indentation hardening mappings and images of optical and scanning electron microscopy are performed. They are corroborated by macro hardness profile throughout the sample.

The present article is organized as follows. Section 2 describes the manufacturing process, the fabricated parts, as well as the strategy of power optimization. Section 3 provides the numerical model of the DED process, while Section 4 presents the results related to the different laser power functions: molten pool sizes and temperature histories, as well as the experimental micro and nanohardness maps of the deposited materials with their respective analysis. The main conclusions and ongoing work are listed in the last Section 5.

2. Materials and Methods

2.1. Manufacturing process

The schematic depiction of the DED process applied to manufacture the M4 samples is shown in Fig. 3(a). The 5-axis 2kW Irep Nd-YAG laser DED machine of Sirris Research Center was used to manufacture three rectangular cuboids from M4 high speed steel powder of 50 to 150 μm particle size (Table 1). The top-hat intensity distribution laser beam spot diameter is 1.5 mm. Overlapping tracks of 1.4 mm were applied and Argon gas was utilized for the protection of the workpiece. The processing head of the machine is equipped with a coaxial supply of powder to the laser beam in order to apply the powder with 10 mm of standoff distance (substrate surface distance from the nozzle tip).

Three different laser power functions were considered for manufacturing the three types of samples, one constant power value (CP) and two time dependent functions: LPF1 and LPF2, which were identified by the method described in Section 2.3. The process parameters such as the nozzle scanning speed, powder feed rate, and the pre-heating temperature of the 42CrMo4 substrate (40 mm height, 100 mm diameter) were set constants with 6.87 mm/s, 76 mg/s, 300 °C, respectively. The dimensions of the manufactured samples and the locations of hardness measurements are given in Table 2. The temperature points recorded during the process by 4 thermocouples were located within the substrate at a depth of 5 mm from the top surface and at a distance of 20 mm from the substrate circumference. The clad sample geometry and axes are described in Fig. 3(b) while Table 2 provides the accurate dimensions.

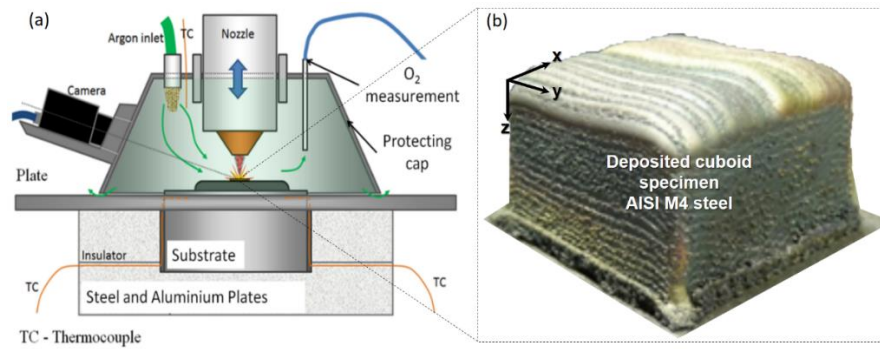


Fig. 3. (a) DED process used for the manufacturing of the bulk M4 samples, (b) Cuboid sample geometry and axes.

Table 1. Mass fraction of feedstock M4 powder steel used for the DED AM of cuboid samples.

W	Mo	Cr	V	C	Ni	Mn	Si	Fe
0.0560	0.0464	0.043	0.0410	0.0135	0.0090	0.0034	0.0033	Bal.

Table 2. Geometry of the M4 steel DED manufactured cuboid parts including Vickers hardness measurements locations.

Cuboid parts	Total height (Z direction, mm)	Width (X direction, mm)	Length (Y direction mm)	Vickers Hardness profile length*	Position of Vickers Hardness profile within deposit	
					X (mm)	Y (mm)
Constant power (CP)	27.3	41.5	42	15.5	17.6	21.5
Function 1 (LPF1)	20.8	41.9	43.4	20.5	22.4	22.1
Function 2 (LPF2)	23.6	41.6	43.1	20.5	20.8	19.2

* Starting 500 μm below the top clad surface.

2.2. Hardness measurement campaign

The mechanical properties such as yield limit can be related to Vickers hardness profiles. Table 2 gives the Vickers measurement locations and Figure 8(b) the hardness profiles. Vickers hardness measurements are performed on a universal EMCO MC10 machine equipped with an electronic cell force and a closed loop regulation, using a load of 100N. For each sample, a hardness profile is made along a line parallel to the building direction (Z axis) and close to the middle of the block (see Table 2). There is one Vickers indent every 500 μm starting from the top of the deposit down to the substrate. The Vickers hardness measurements (Fig. 8) help determining the evolution of the homogeneity of the structure at a macro scale in the core of the sample.

Nanoindentations tests are carried out using a Hysitron Ti 950 Triboindenter with a Berkovich tip. The nano indentation grid locations are provided in Fig. 8(a) and the measured nanoindentation hardness maps are reported in Fig. 9 for the three samples. Each 46x36 grid results in 1656 indents, with 3 μm between two consecutive indents. The tests are performed under displacement control mode; the penetration depth being set at 300 μm for each indent. The nanoindentation tests are intended to assess the homogeneity of the microstructure at a local scale.

2.3. Microstructure characterization

The microstructure of the manufactured sample with a constant laser power (CP) was characterized at the top and middle points located at 760 μm and 13.8 mm from the upper free surface of the DED sample respectively (Fig. 4). Two magnifications of 1000 x and 3000 x are used to observe a cellular-type microstructure with slightly varying size between the different layers. As established in Jardin et al. [9], the apparent scratches seen under high magnification should be related to residual austenite not transformed into martensite in this as built sample. Similar images were measured for samples generated by LPF1 and LPF2.

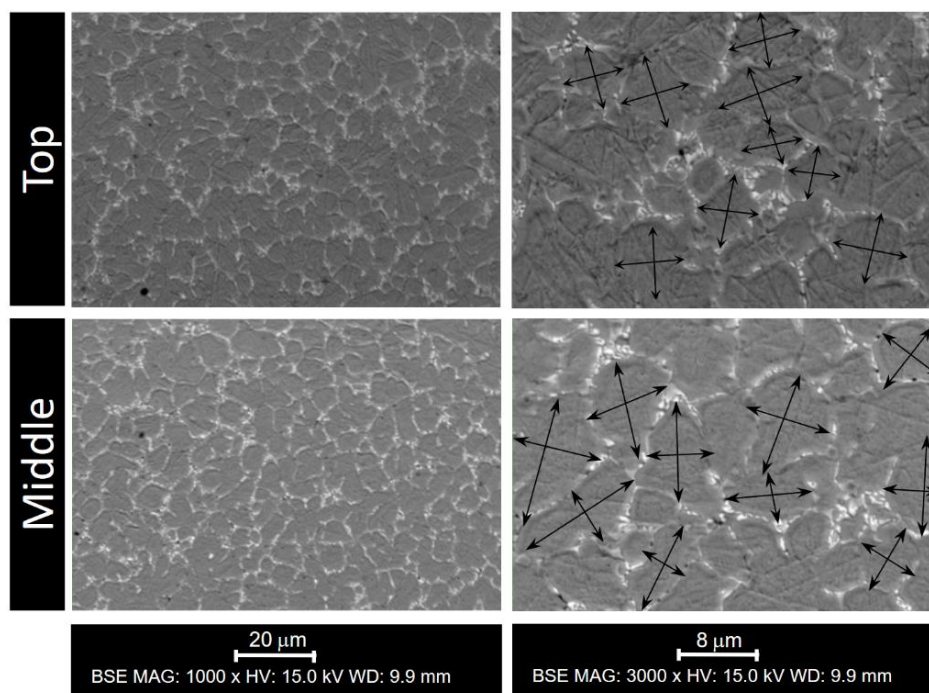


Fig. 4. Microstructure of cuboid sample manufactured with constant DED laser power observed at top and middle locations with two magnifications 1000 x and 3000 x.

3. Numerical model of the DED process

This section presents the finite element simulations of the DED process as well as the Python script computing the optimization of the laser power functions to achieve a melt pool of constant size within the deposit height.

3.1. FE simulation of DED process

The Lagamine FE code developed since 1984 [50–54] at the University of Liege is used to compute the thermal history of the deposit and the substrate. The Fourier's law of heat conduction, and the surface energy balance considering convection and radiation heat transfer equations are taken into account within the two dimensional FE simulations. The

model relies on the BLZ2T solid finite element and the CONRA interface elements (see Lagamine user guide for details [54]). The addition of material during the additive process is simulated by using the element birth technique [40]. Further information of the numerical modeling and previous simulations of the investigated AISI M4 DED process are given in Jardin et al. [24].

The FE model shown in Fig. 5(a) considers a vertical cut in the center of the deposit material. The horizontal and vertical mesh directions of the zoom picture in Fig. 5(a) are aligned with the horizontal trajectory of the laser and the building direction respectively. In order to reduce the computational time, the 36 deposited layers of an average size of 0.764 mm height are modeled with bidimensional elements assuming no transversal thermal flow outside the mesh plane. Such an assumption can be questionable but allows reasonable CPU time which is a mandatory constraint as an optimization loop is aimed. The implication of this 2D choice is a careful definition of the boundary conditions that are adjusted to recover both the measured thermocouple histories and the melt pool size measurements. Validations of this simplified approach for the studied sample geometry has been provided both for AISI M4 material [24] and for 316L + WC [55]. To generate an optimal 2D FE mesh, transition refinement element groups are used and the non-uniform mesh refinement given in Fig. 5(a) is applied. The substrate affected by the laser source is refined to accurately model heat fluxes, while the bottom of the substrate is coarsely meshed. The heat flux loading under the laser beam is applied to 2 solid elements by nodal power values and convection and radiation interface elements are placed on the boundaries of the substrate and the deposit to model the heat exchanges. Inside the deposit, the element width of 0.75 mm corresponds to half of the diameter of the laser spot. Applying the laser beam speed used in the experiment, the element birth technique of the 2D FE simulation models the movement of the heat source and material addition with an idle time taking into account the missing tracks not computed for each layer. For the simulations, the laser heat flux scale factor between the 2D model and the experiment with a constant laser power was adjusted based on the measured substrate temperature and the melt pool size of the last layer. Such a double check is mandatory to prevent any lack of representativeness of the simulations [56]. In the 2D FE model of DED process, the physical laser power value and the absorptivity factor can indeed not be directly used [57].

The variations of thermal conductivity, density and specific heat capacity with the temperature were measured from specimens extracted from the deposit and from substrate [9]. Regarding the emissivity factor for radiation and convection coefficient, values of 1 and 230 W/m²K, are respectively used. It is worth mentioning that thermodynamic simulations (Calphad) allowed obtaining the solidus and liquidus temperatures corresponding to 1503 K and 1677 K for AISI M4 materials. According to Morch et al. [58], for the numerical stability and physical accuracy of the predicted temperature fields, a continuous evolution of the thermo-physical material properties over the process temperature range is essential, a feature that was respected in the input material data set.

3.2. Optimization strategy to reach a constant melt pool size

Within a Python script, at each new layer, the value of the laser power assumed constant within the layer is adjusted to predict the constant melt pool size (depth and length) requested by the user. This optimization loop, based on a Newton-Rapson iterative method modifies the

input laser power value to minimize an objective function expressing the difference between the user constant values requested and the ones computed. The flowchart of this optimization scheme is shown in Fig. 5(b).

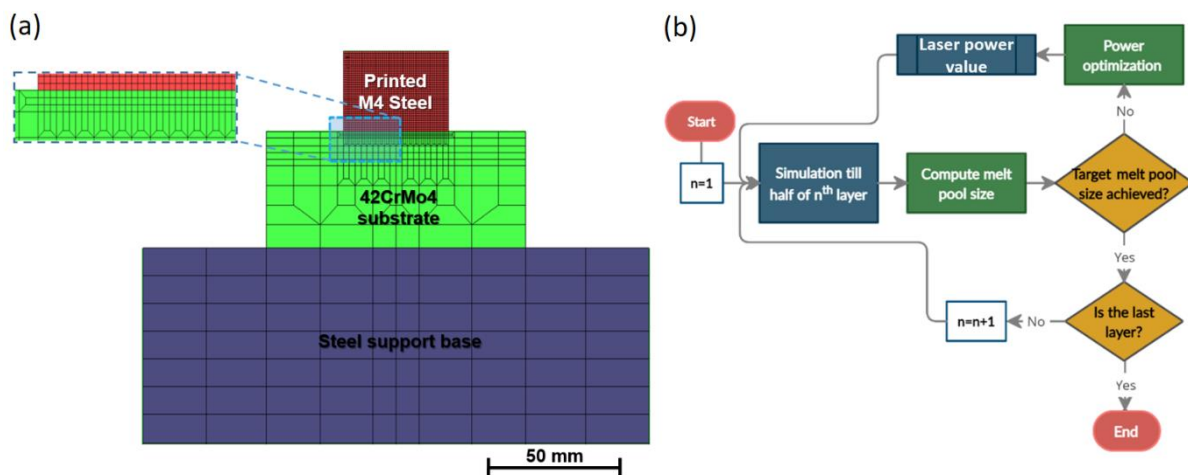


Fig. 5. (a) 2D FE Mesh used for DED process simulations and (b) flowchart of the laser power optimization process strategy for a constant melt pool size.

4. Results and discussion

The microstructure of metals and alloys are highly dependent on the thermal gradient, solidification temperature gradients and cooling rates. For the manufacturing of DED samples, the process parameters determine the thermal cycles and the number of re-melting of each layer which affects the homogeneity of the local material properties near the melt pool boundary. Based on two different runs with different targets, the optimization Python script strategy based on the 2D FE DED process model has determined two laser power functions (LPF1 and LPF2). The experimental results compare the microstructure homogeneity of the samples generated by these functions with the one manufactured with a constant laser function (CP).

4.1. Laser power functions, molten pool sizes and temperature histories

Iterative steps varying the laser power value associated to each layer of the simulated DED samples are run in order to reach a constant melt pool size (length and depth). Numerical results of the melt pool size by applying a constant power value and the identified optimized laser power functions are shown in Fig. 6. Homogeneous melt pool depth and length are indeed numerically computed in the sample manufactured with both laser power functions LPF1 and LPF2. Each power function provides a homogeneous melt pool of a different size: 1.4 and 1.8 mm for the depth and 5.7 and 4.4 for the length, respectively; which were the two different targets within the optimization process.

Regarding the computed thermal history, the peak values of three typical observed zones (Bottom, Middle, Top) in Fig. 7 are different for each power function (CP, LPBF1, LPBF2). As in Jardin et al. [24], the 2D finite element mesh (Fig. 5(a)) models the center track of each layer of the actual process and the FE simulations provide the thermal field at any point in this

middle plane. The temperature histories of the material points representative of the Bottom, Middle and Top of the samples (see Fig. 8(a)) and deposited in the middle plane of the sample are plotted in Fig.7 for each power function (CP, LPF1, LPF2). Each curve shows the temperature observed by a material point: a peak above the melting temperature while the material is deposited, followed by a cooling stage as the laser moves away. The first rapid local cooling is due to solidification energy, followed by a slower gradient due to heat loss to the workpiece by conduction and to the surroundings by radiation and convection, when the laser moves away. When the next layer is deposited, there is a warming as the laser approaches and the material point is melted a second time but its temperature level is lower and a cooling stage happens again as the laser moves away. This thermal cycle repeats itself being attenuated more and more (partial then no re-melting), as more and more layers separate the analyzed material point from the laser energy source. For the Bottom representative point, the effect of the last layers is not any more noticeable (no peak). The Top representative points are at the second last layer for the LPF1 and LPF2 power functions as only two peaks are observed (Fig. 7 (b) and (c)) and 2 layers deeper for the constant laser power case. Note that each sample has a different height as a different laser power values generates different layer heights which explains the different time and layer number associated to each zone in Fig. 7. The highest peaks are observed as expected in the manufactured part with the LPF2 manufacturing (highest power value), and the maximum peak values have average of 2660 K. In addition, the number of thermal cycles inducing a total remelting of a layer and the value of the temperature reached during total or partial remelting present considerable changes with the laser power energy function. This number of remelting phenomena increases with the laser power.

Both previous phenomena, superheating value and number of remeltings extracted from the simulations of the DED manufacturing process help to analyze the experimental microhardness profiles and the nanoindentation distribution maps of the samples, as well as the residual stresses state that justify post-mortem cracks discussed in the next subsection.

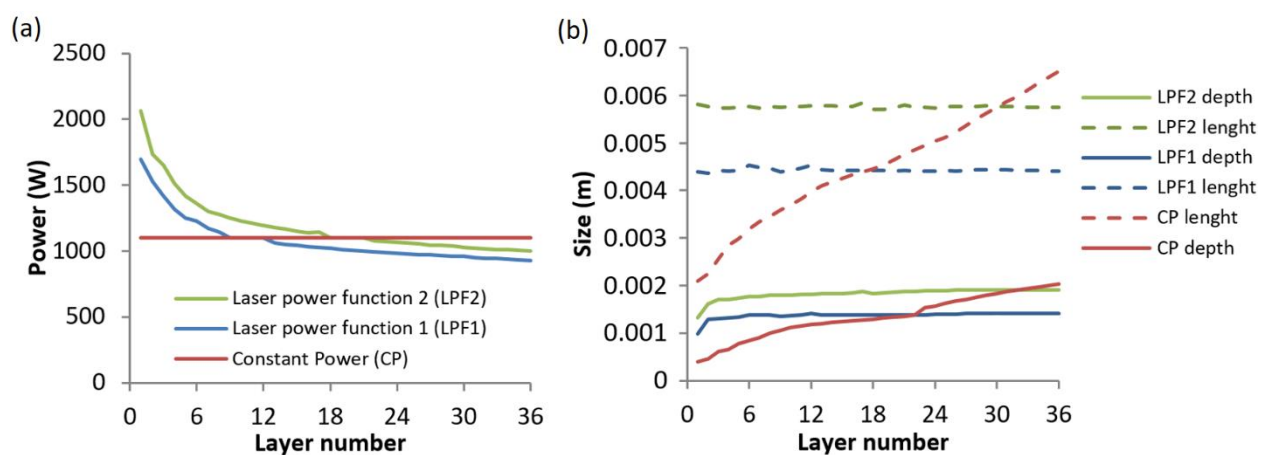


Fig. 6. (a) Laser power functions obtained from the proposed methodology. (b) Computed molten pool over the layers for LPF1, LPF2 and CP.

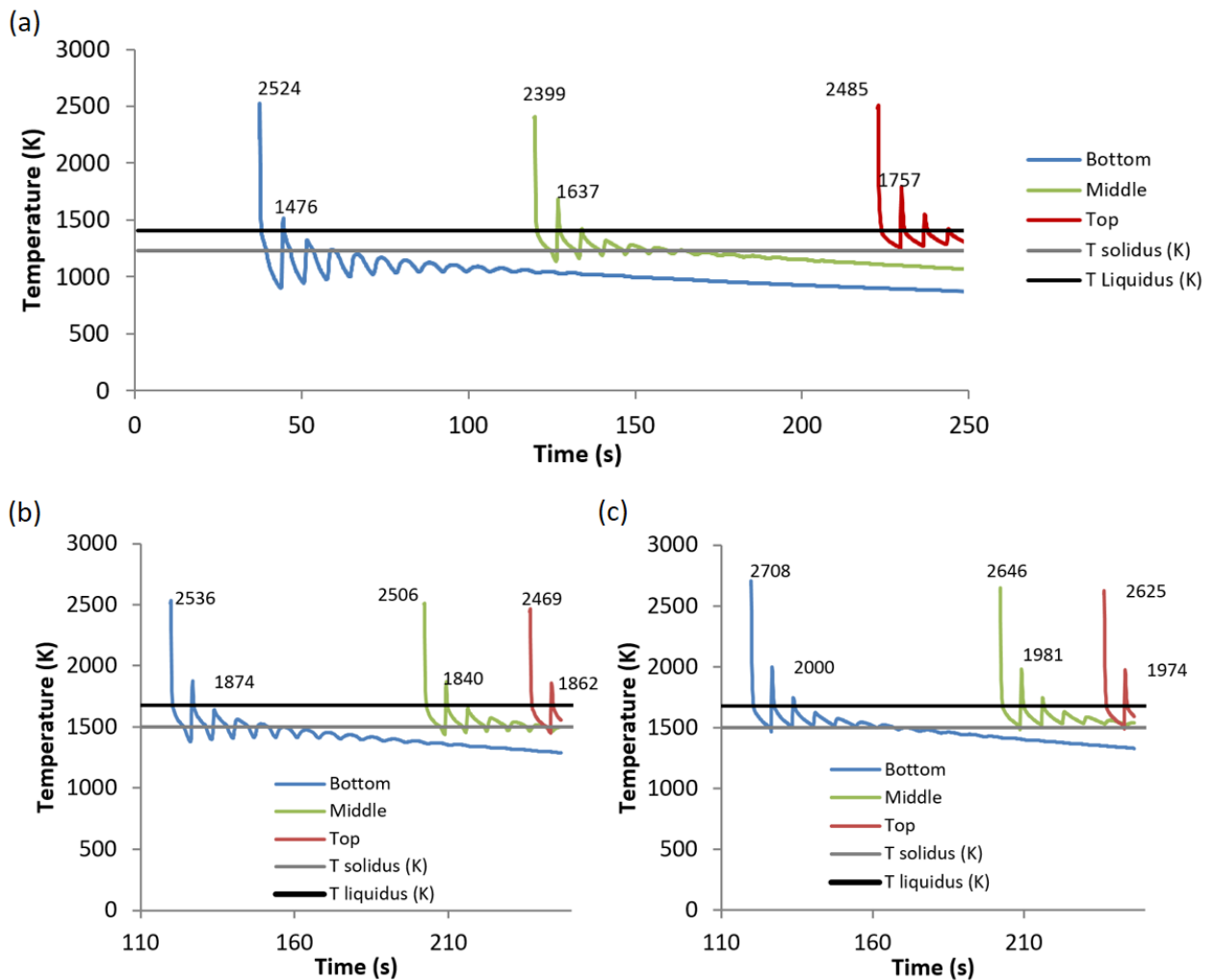


Fig. 7. Thermal history of the Top, Middle and Bottom layers obtained by applying the three laser power functions: (a) CP, (b) optimized LPF1, and (c) optimized LPF2.

4.2. Microhardness distribution of the samples

Fig. 8(a) shows the cross-section of the cut samples obtained with the different laser power functions. The cutting of the sample manufactured by CP and LPF1, required for hardness measurements, revealed cracks appearance. As proved by the observations of all the as-built samples, they do not present any crack (Fig. S.1). The lack of oxidation, confirmed by EDX mapping performed within the cracks present after cutting in CP and LPF1 samples tells that those cracks are post mortem (Figs. S.2 and Figs. S.3). They appeared when cutting the sample and not during the DED process. During the process, cracks would also have been noticed because of noise and of the fact that the laser DED machine is programmed with a security feature which stops the process if a minimum standoff distance (between the laser and the deposit) is reached. Indeed, a crack reduces this distance and in addition, the sample shape would have also been affected due to the lower conducted heat escape. So all these reasons confirm the post mortem crack assumption. The LPF2 sample exhibits reduced residual stresses inside the cubic part built according the absence of any cracking during cutting. This LPF2 case is interesting as it avoids further heat treatments [59] required to reduce the residual stresses generating cracks in both CP and LPF1 samples. The higher heat accumulation achieved within sample LPF2 (Fig. 7c) in comparison to samples CP and LPF1 (Fig. 7a and b),

and the higher homogeneity level within the same sample can justify a better stress relief that avoids a subsequent cold cracking phenomenon.

Both the level and the scattering of the microhardness profiles provide information on the microstructure state. More homogeneous profiles with the optimized laser power functions LPF1 and LPF2 are obtained, at a qualitative level, according the hardness scattering features of the curves Fig. 8(b) and the computed variance (Fig. 8(c)).

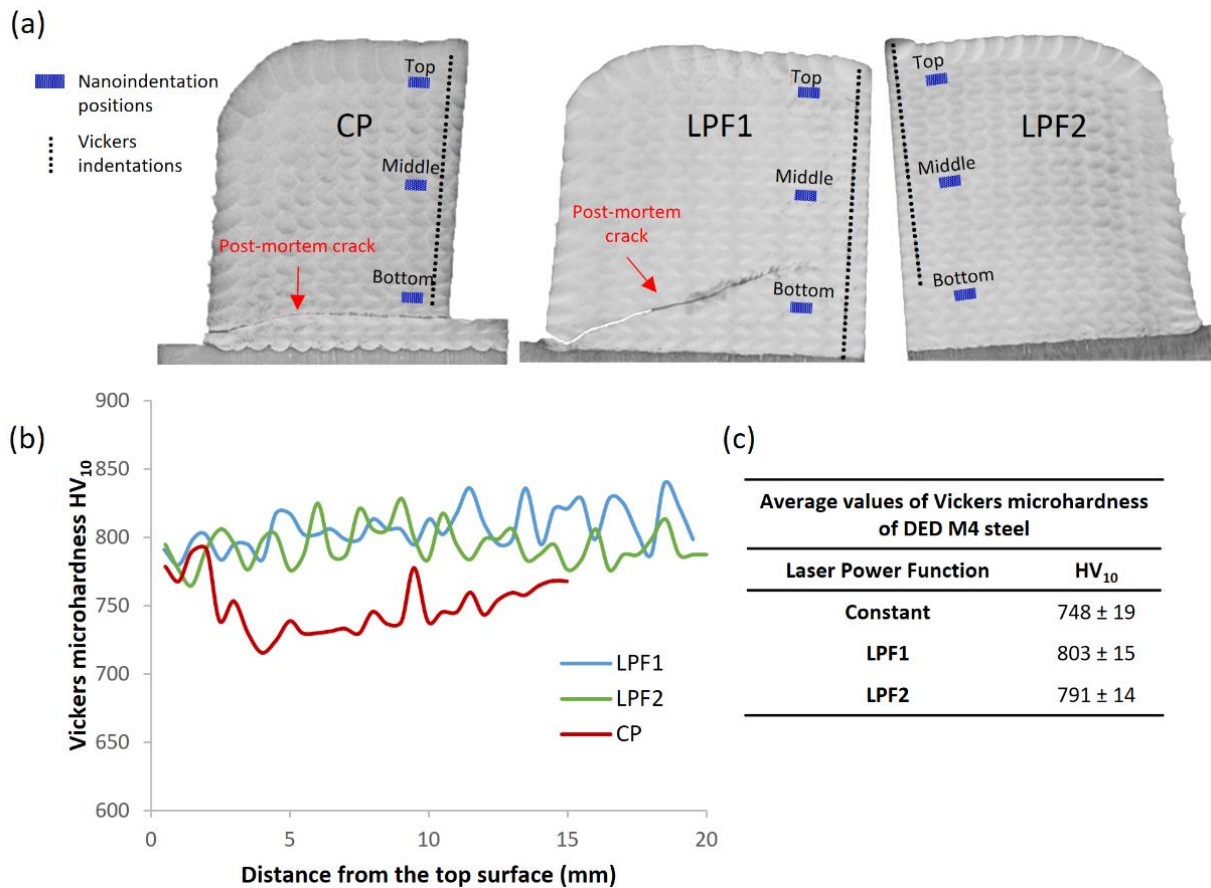


Fig. 8. (a) Overview of cross-sections with the location of the vertical hardness profiles close to the middle axis for the tree manufacturing strategies of laser power function (CP, LPF1 and LPF2); (b) Evolution of the hardness profile with the depth from the top surface of the samples; and the (c) computed average values of microhardness Vickers HV₁₀ measured at the cross-section.

4.3. Nanomechanical hardness map

The nanoindentation grids performed in the cut sections of the manufactured samples at the location points given in Fig. 8 allow building the nanohardness maps of Fig. 9. The part manufactured with constant power (CP) shows non-homogeneous nanohardness field with higher values in the middle zone of around 9.5 GPa. A more homogeneous hardness field is found with the laser power function 1 (LPF1) compared to CP. However, the local hardness in the middle zone show higher values and variation which is not the target aim of this work. This is clearly not seen in the Vickers hardness measurements (Fig. 8) and cannot be explained by the computed thermal histories since the measurement resolution here is higher than the element size. It would require a mesh refinement which is not justified since mass transfer

effects due to convection and Marangoni effect cannot be represented with the current implemented macroscopic solid finite element model. The targeted homogeneous nanohardness distribution in the Middle zone of the part are finally obtained by applying the optimized laser power function 2 (LPF2) defined by the developed optimization strategy. The reduced hardness in the top layer is actually not an issue, because the last deposited layer and free surfaces of the part are generally machined in order to obtain a good surface finish and accurate final shape of the manufactured part.

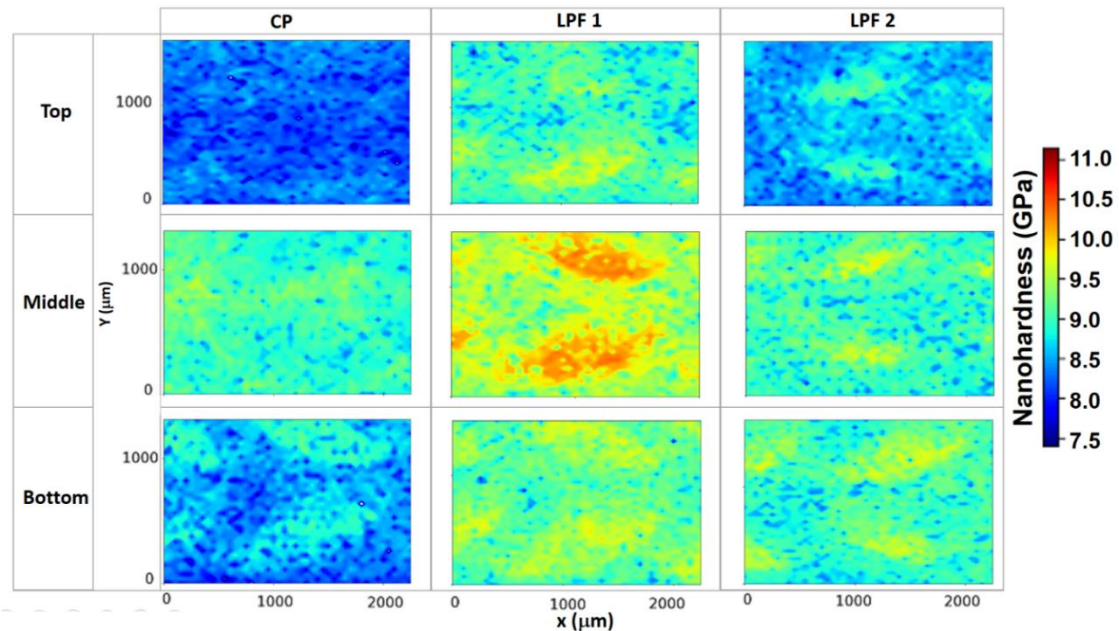


Fig. 9. Nanohardness maps of the cross-section of the samples at the top, bottom and middle location points.

4.4. Analysis of results

The thermal histories shown in Fig. 7 (the maximum temperatures of the melt pools, the peak temperatures of the liquid metal during the last solidifications, the numbers of total or partial remeltings) within the top, the middle and the bottom zones of the samples, obtained by applying constant CP, optimized LPF1 and LPF2 laser power functions are analyzed to identify any links with the melt pool sizes and the micro and nanohardness profiles.

The discrepancies between the thermal histories associated to each location are clearly higher for the CP case (Fig. 7(a)) than for LPF1 and LPF2 cases, which is consistent with the computed non-constant melt pool of CP case versus LPF1 and LPF2 cases (Fig. 6(b)). For the latter cases, the very small variations around the reached constant melt pool size are similar, however the discrepancies between the thermal histories of the different location points in LPF1 case (see the numbers of re-melting events between bottom and middle locations) are higher than the ones observed for LPF2. This ranking in variations within the local thermal histories of each sample is kept within the heterogeneity of their nano indentation maps (Fig. 9).

The higher homogeneity of the LPF2 part observed in nanohardness maps (Fig. 9) could be associated to the highest peak temperature values of the melt pools (the average value is 2569K for the maximum temperature) compared to CP (2469K) and LPBF1 (2505K) cases. It produces a higher accumulation of heat which generates slower cooling process (see Fig. 7(c)), allowing more homogenous temperature within the parts as well as lower residual stresses.

No crack appeared during the postmortem vertical cross-section inspection, provided in Fig.8, for LPF2 case compared to CP and LPF1 cases. These cracks are the result of the critical residual stresses in the as-built conditions. The in-situ annealing during LPF2 processing helps achieving stress relief unlike in CP and LFP1 configurations.

The CP sample shows heterogeneity both at the macro level (see Vickers profile Fig. 8) and at the nano scale (Fig. 9). The average nanohardness is low at the bottom of the deposit, and more importantly, it shows some heterogeneity within the melt pool areas. For the top of the deposit, the average hardness is globally lower, even if it is more homogeneous than at the bottom. On the other hand, in the middle of the deposit, there is a higher level of hardness (average of 9.5 GPa in nanohardness and 800 HV in Vickers). Considering the previous studies, it can be noted that such a hardness for the given alloy can lead to improved mechanical [9] and tribological properties [23]. In the case of wear resistance in particular, the wear loss was found homogeneous regardless of the sliding speed within this middle location (see Fig. 1). This zone of the CP sample can therefore be considered as the adequate homogeneous structure (AHS) to achieve.

The LFP1 sample exhibits the AHS only on the top position, the middle and the bottom position being different, with higher hardness and/or a more pronounced heterogeneity. Therefore, a local thermal post-treatment should be required to achieve the AHS in all the zones, which is not an easy task.

The LFP2 configuration, on the other hand, presents the AHS in both the bottom and the middle positions. The top of the deposit, on the other hand, shows a slightly lower average hardness, which is however not critical if machining is considered subsequently.

5. Conclusions

The main objective of this work was to develop a process strategy to reach homogeneous and optimal mechanical properties of the whole AISI M4 DED as built material part to avoid or reduce thermal post treatment. The numerical strategy presented here is a cost effective method for saving time and improving quality in the DED manufacturing and repair processes of machine tools and parts. Using validated 2D FE thermomechanical simulations of the DED process within a Newton-Rapson optimization method, an optimal laser power function was determined to generate bulk M4 steel samples with a constant melt pool along the built direction.

Regarding the link with the thermal history, the dimensional control of the melt pool reasonably allows reproducing at any point of the deposit, a similar complex thermal history. It considers the heat accumulation directly brought by the preheating, but also the one induced during the manufacturing process by layers overlapping. As pointed by LPBF1 and LPBF2 cases, constant melt pool increases the sample homogeneity. Achieving in addition close thermal histories along the sample depth yields the best hardness homogeneity as for sample LPBF2. It relies on high peak temperatures within the melt pool. The post mortem cracks phenomena in DED manufactured parts can also be avoided with these high temperatures as an in-situ annealing happens.

Adding within the cost function the need of a high average of peak temperature within the melt pool will be the next research step for this material. Ongoing work is being carried out to

optimize the process parameters using machine learning strategies. Note that the thermal history predicted by solid FE simulations will not be able to explain the nanohardness variation within the melt pool zones. To this end, Marangoni effect should be added within the modelling though computational fluid mechanics and a higher mesh density.

Acknowledgments

This work was funded by Walloon Region through the RW 11-1-7335 Recyclad project, FNRS F.R.S. [PDR T.0039.14], FEDER [IAWATHA], the cooperation agreement WBI/AGCID SUB2019/419031 (DIE19-0005) and Universidad de La Frontera (DI22-0067). As Research Director of FRS-FNRS, A.M.H. acknowledges the support of this institution. The Center for Applied Research and Education in Microscopy CAREM of ULiège is also thanked for providing SEM/EDS facilities. Computational resources were provided by the Consortium des Équipements de Calcul Intensif (CÉCI) funded by the F.R.S.-FNRS. The authors also acknowledge Olivier Dedry for providing additional thermophysical properties data and Hélène Morch for the improvement of the optimization method.

References

- [1] P. Alvarez, M.Á. Montealegre, F. Cordovilla, Á. García-Beltrán, I. Angulo, J.L. Ocaña, Direct Generation of High-Aspect-Ratio Structures of AISI 316L by Laser-Assisted Powder Deposition, *Materials (Basel)*. 13 (2020) 5670. <https://doi.org/10.3390/ma13245670>.
- [2] C. Tan, J. Zou, S. Li, P. Jamshidi, A. Abena, A. Forsey, R.J. Moat, K. Essa, M. Wang, K. Zhou, M.M. Attallah, Additive manufacturing of bio-inspired multi-scale hierarchically strengthened lattice structures, *Int. J. Mach. Tools Manuf.* 167 (2021) 103764. <https://doi.org/10.1016/j.ijmachtools.2021.103764>.
- [3] J. Huang, L. Qi, J. Luo, L. Zhao, H. Yi, Suppression of gravity effects on metal droplet deposition manufacturing by an anti-gravity electric field, *Int. J. Mach. Tools Manuf.* 148 (2020) 103474. <https://doi.org/10.1016/j.ijmachtools.2019.103474>.
- [4] A. Borovkov, L. Maslov, F. Tarasenko, M. Zhmaylo, I. Maslova, D. Solovev, Development of elastic-plastic model of additively produced titanium for personalised endoprosthetics, *Int. J. Adv. Manuf. Technol.* 117 (2021) 2117–2132. <https://doi.org/10.1007/s00170-021-07460-1>.
- [5] D. Gu, X. Shi, R. Poprawe, D.L. Bourell, R. Setchi, J. Zhu, Material-structure-performance integrated laser-metal additive manufacturing, *Science (80-.)*. 372 (2021). <https://doi.org/10.1126/science.abg1487>.
- [6] C. Tan, F. Weng, S. Sui, Y. Chew, G. Bi, Progress and perspectives in laser additive manufacturing of key aeroengine materials, *Int. J. Mach. Tools Manuf.* 170 (2021) 103804. <https://doi.org/10.1016/j.ijmachtools.2021.103804>.

- [7] D.-S. Shim, G.-Y. Baek, J.-S. Seo, G.-Y. Shin, K.-P. Kim, K.-Y. Lee, Effect of layer thickness setting on deposition characteristics in direct energy deposition (DED) process, *Opt. Laser Technol.* 86 (2016) 69–78. <https://doi.org/10.1016/j.optlastec.2016.07.001>.
- [8] N. Ur Rahman, L. Capuano, S. Cabeza, M. Feinaeugle, A. Garcia-Junceda, M.B. de Rooij, D.T.A. Matthews, G. Walmag, I. Gibson, G.R.B.E. Römer, Directed energy deposition and characterization of high-carbon high speed steels, *Addit. Manuf.* 30 (2019) 100838. <https://doi.org/10.1016/j.addma.2019.100838>.
- [9] R.T. Jardin, V. Tuninetti, J.T. Tchuindjang, N. Hashemi, R. Carrus, A. Mertens, L. Duchêne, H.S. Tran, A.M. Habraken, Sensitivity Analysis in the Modelling of a High Speed Steel Thin-Wall Produced by Directed Energy Deposition, *Metals (Basel)*. 10 (2020) 1554. <https://doi.org/10.3390/met10111554>.
- [10] S.J. Wolff, H. Wang, B. Gould, N. Parab, Z. Wu, C. Zhao, A. Greco, T. Sun, In situ X-ray imaging of pore formation mechanisms and dynamics in laser powder-blown directed energy deposition additive manufacturing, *Int. J. Mach. Tools Manuf.* (2021). <https://doi.org/10.1016/j.ijmachtools.2021.103743>.
- [11] J.W. Murray, A. Speidel, A. Jackson-Crisp, P.H. Smith, H. Constantin, A.T. Clare, Unprocessed machining chips as a practical feedstock in directed energy deposition, *Int. J. Mach. Tools Manuf.* 169 (2021) 103803. <https://doi.org/10.1016/j.ijmachtools.2021.103803>.
- [12] J.Y. Hascoët, S. Touzé, M. Rauch, Automated identification of defect geometry for metallic part repair by an additive manufacturing process, *Weld. World.* (2018). <https://doi.org/10.1007/s40194-017-0523-0>.
- [13] H. Siva Prasad, F. Brueckner, J. Volpp, A.F.H. Kaplan, Laser metal deposition of copper on diverse metals using green laser sources, *Int. J. Adv. Manuf. Technol.* 107 (2020) 1559–1568. <https://doi.org/10.1007/s00170-020-05117-z>.
- [14] G. Xu, C. Song, H. Zhang, H. Lu, D. Wu, K. Luo, J. Lu, Spatially heterogeneous microstructure in in-situ TiO-reinforced Ti6Al4V/316L functionally graded material fabricated via directed energy deposition, *Addit. Manuf.* 59 (2022) 103178. <https://doi.org/10.1016/j.addma.2022.103178>.
- [15] H. Chen, Y. Chen, Y. Liu, Q. Wei, Y. Shi, W. Yan, Packing quality of powder layer during counter-rolling-type powder spreading process in additive manufacturing, *Int. J. Mach. Tools Manuf.* 153 (2020) 103553. <https://doi.org/10.1016/j.ijmachtools.2020.103553>.
- [16] A. Malakizadi, T. Hajali, F. Schulz, S. Cedergren, J. Ålgårdh, R. M'Saoubi, E. Hryha, P. Krajnik, The role of microstructural characteristics of additively manufactured Alloy 718 on tool wear in machining, *Int. J. Mach. Tools Manuf.* 171 (2021) 103814. <https://doi.org/10.1016/j.ijmachtools.2021.103814>.
- [17] S.M.H. Hojjatzadeh, N.D. Parab, Q. Guo, M. Qu, L. Xiong, C. Zhao, L.I. Escano, K. Fezzaa, W. Everhart, T. Sun, L. Chen, Direct observation of pore formation mechanisms during LPBF additive manufacturing process and high energy density laser welding, *Int. J. Mach. Tools Manuf.* 153 (2020) 103555. <https://doi.org/10.1016/j.ijmachtools.2020.103555>.

- [18] T. Furumoto, S. Abe, M. Yamaguchi, A. Hosokawa, Improving surface quality using laser scanning and machining strategy combining powder bed fusion and machining processes, *Int. J. Adv. Manuf. Technol.* 117 (2021) 3405–3413. <https://doi.org/10.1007/s00170-021-07880-z>.
- [19] J. Lu, H. Lu, X. Xu, J. Yao, J. Cai, K. Luo, High-performance integrated additive manufacturing with laser shock peening –induced microstructural evolution and improvement in mechanical properties of Ti6Al4V alloy components, *Int. J. Mach. Tools Manuf.* 148 (2020) 103475. <https://doi.org/10.1016/j.ijmachtools.2019.103475>.
- [20] C. Wang, X.P. Tan, S.B. Tor, C.S. Lim, Machine learning in additive manufacturing: State-of-the-art and perspectives, *Addit. Manuf.* 36 (2020) 101538. <https://doi.org/https://doi.org/10.1016/j.addma.2020.101538>.
- [21] D. Carluccio, M. Bermingham, D. Kent, A.G. Demir, B. Previtali, M.S. Dargusch, Comparative Study of Pure Iron Manufactured by Selective Laser Melting, Laser Metal Deposition, and Casting Processes, *Adv. Eng. Mater.* 21 (2019) 1900049. <https://doi.org/10.1002/adem.201900049>.
- [22] F. Soffel, D. Eisenbarth, K. Wegener, Effect of clad height, substrate thickness and scanning pattern on cantilever distortion in direct metal deposition, *Int. J. Adv. Manuf. Technol.* 117 (2021) 2083–2091. <https://doi.org/10.1007/s00170-021-06925-7>.
- [23] N. Hashemi, A. Mertens, H.M. Montrieux, J.T. Tchuindjang, O. Dedry, R. Carrus, J. Lecomte-Beckers, Oxidative wear behaviour of laser clad High Speed Steel thick deposits: Influence of sliding speed, carbide type and morphology, *Surf. Coatings Technol.* 315 (2017) 519–529. <https://doi.org/10.1016/j.surfcoat.2017.02.071>.
- [24] R.T. Jardin, J. Tchoufang Tchuindjang, L. Duchêne, H.-S. Tran, N. Hashemi, R. Carrus, A. Mertens, A.M. Habraken, Thermal histories and microstructures in Direct Energy Deposition of a High Speed Steel thick deposit, *Mater. Lett.* 236 (2019) 42–45. <https://doi.org/10.1016/j.matlet.2018.09.157>.
- [25] D.-S. Shim, G.-Y. Baek, E.-M. Lee, Effect of substrate preheating by induction heater on direct energy deposition of AISI M4 powder, *Mater. Sci. Eng. A.* 682 (2017) 550–562. <https://doi.org/10.1016/j.msea.2016.11.029>.
- [26] S.M.J. Razavi, F. Berto, Directed Energy Deposition versus Wrought Ti-6Al-4V: A Comparison of Microstructure, Fatigue Behavior, and Notch Sensitivity, *Adv. Eng. Mater.* 21 (2019) 1900220. <https://doi.org/10.1002/adem.201900220>.
- [27] R.A. Rahman Rashid, M.A. Javed, C. Barr, S. Palanisamy, N. Matthews, M.S. Dargusch, Effect of in situ tempering on the mechanical, microstructural and corrosion properties of 316L stainless steel laser-cladded coating on mild steel, *Int. J. Adv. Manuf. Technol.* 117 (2021) 2949–2958. <https://doi.org/10.1007/s00170-021-07886-7>.
- [28] T. Deng, J. Li, Z. Zheng, Fundamental aspects and recent developments in metal surface polishing with energy beam irradiation, *Int. J. Mach. Tools Manuf.* 148 (2020) 103472. <https://doi.org/10.1016/j.ijmachtools.2019.103472>.
- [29] V. Tuninetti, G. Gilles, P. Flores, G. Pincheira, L. Duchêne, A.M. Habraken, Impact of distortional hardening and the strength differential effect on the prediction of large

- deformation behavior of the Ti6Al4V alloy, *Meccanica*. 54 (2019) 1823–1840. <https://doi.org/10.1007/s11012-019-01051-x>.
- [30] V. Tuninetti, P. Flores, M. Valenzuela, G. Pincheira, C. Medina, L. Duchêne, A.-M. Habraken, Experimental characterization of the compressive mechanical behaviour of Ti6Al4V alloy at constant strain rates over the full elastoplastic range, *Int. J. Mater. Form.* 13 (2020) 709–724. <https://doi.org/10.1007/s12289-020-01543-2>.
- [31] Y. Su, Z. Wang, H. Lu, K. Luo, J. Lu, Improved wear resistance of directed energy deposited Fe-Ni-Cr alloy via closed-loop controlling laser power, *J. Manuf. Process.* 75 (2022) 802–813. <https://doi.org/10.1016/j.jmapro.2022.01.047>.
- [32] Y. Su, Z. Wang, X. Xu, K. Luo, J. Lu, Effect of closed-loop controlled melt pool width on microstructure and tensile property for Fe-Ni-Cr alloy in directed energy deposition, *J. Manuf. Process.* 82 (2022) 708–721. <https://doi.org/10.1016/j.jmapro.2022.08.049>.
- [33] W. Cong, F. Ning, A fundamental investigation on ultrasonic vibration-assisted laser engineered net shaping of stainless steel, *Int. J. Mach. Tools Manuf.* 121 (2017) 61–69. <https://doi.org/10.1016/j.ijmactools.2017.04.008>.
- [34] S.-H. Park, P. Liu, K. Yi, G. Choi, K.-Y. Jhang, H. Sohn, Mechanical properties estimation of additively manufactured metal components using femtosecond laser ultrasonics and laser polishing, *Int. J. Mach. Tools Manuf.* 166 (2021) 103745. <https://doi.org/10.1016/j.ijmactools.2021.103745>.
- [35] H. Tan, C. Zhang, W. Fan, F. Zhang, X. Lin, J. Chen, W. Huang, Dynamic evolution of powder stream convergence with powder feeding durations in direct energy deposition, *Int. J. Mach. Tools Manuf.* 157 (2020) 103606. <https://doi.org/10.1016/j.ijmactools.2020.103606>.
- [36] L. Peng, J. Shengqin, Z. Xiaoyan, H. Qianwu, X. Weihao, Direct laser fabrication of thin-walled metal parts under open-loop control, *Int. J. Mach. Tools Manuf.* 47 (2007) 996–1002. <https://doi.org/10.1016/j.ijmactools.2006.06.017>.
- [37] W. Woo, D.-K. Kim, E.J. Kingston, V. Luzin, F. Salvemini, M.R. Hill, Effect of interlayers and scanning strategies on through-thickness residual stress distributions in additive manufactured ferritic-austenitic steel structure, *Mater. Sci. Eng. A*. 744 (2019) 618–629. <https://doi.org/10.1016/j.msea.2018.12.078>.
- [38] M. Biegler, J. Wang, L. Kaiser, M. Rethmeier, Automated Tool-Path Generation for Rapid Manufacturing of Additive Manufacturing Directed Energy Deposition Geometries, *Steel Res. Int.* 91 (2020). <https://doi.org/10.1002/srin.202000017>.
- [39] T. Maurizi Enrici, O. Dedry, F. Boschini, J.T. Tchuindjang, A. Mertens, Microstructural and Thermal Characterization of 316L + WC Composite Coatings Obtained by Laser Cladding, *Adv. Eng. Mater.* 22 (2020) 2000291. <https://doi.org/10.1002/adem.202000291>.
- [40] H.-S. Tran, J.T. Tchuindjang, H. Paydas, A. Mertens, R.T. Jardin, L. Duchêne, R. Carrus, J. Lecomte-Beckers, A.M. Habraken, 3D thermal finite element analysis of laser cladding processed Ti-6Al-4V part with microstructural correlations, *Mater. Des.* 128 (2017) 130–142. <https://doi.org/10.1016/j.matdes.2017.04.092>.

- [41] J.I. Arrizubieta, A. Lamikiz, M. Cortina, E. Ukar, A. Alberdi, Hardness, grain size and porosity formation prediction on the Laser Metal Deposition of AISI 304 stainless steel, *Int. J. Mach. Tools Manuf.* 135 (2018) 53–64. <https://doi.org/10.1016/j.ijmachtools.2018.08.004>.
- [42] J. Zhang, L. Yang, Z. Li, Q. Zhang, M. Yu, C. Fang, H. Xiao, Transport phenomenon, flow field, and deposition forming of metal powder in the laser direct deposition with designed nozzle, *Int. J. Adv. Manuf. Technol.* 114 (2021) 1373–1383. <https://doi.org/10.1007/s00170-021-06913-x>.
- [43] H. Lu, L. Wu, H. Wei, J. Cai, K. Luo, X. Xu, J. Lu, Microstructural evolution and tensile property enhancement of remanufactured Ti6Al4V using hybrid manufacturing of laser directed energy deposition with laser shock peening, *Addit. Manuf.* 55 (2022) 102877. <https://doi.org/10.1016/j.addma.2022.102877>.
- [44] C. Rojas-Ulloa, C. Bouffieux, A.F. Jaramillo, C.M. García-Herrera, T. Hussain, L. Duchêne, G. Riu, J. Josep Roa, P. Flores, A. Marie Habraken, V. Tuninetti, Nanomechanical Characterization of the Deformation Response of Orthotropic Ti–6Al–4V, *Adv. Eng. Mater.* (2021). <https://doi.org/10.1002/adem.202001341>.
- [45] T. Guan, S. Chen, X. Chen, J. Liang, C. Liu, M. Wang, Effect of laser incident energy on microstructures and mechanical properties of 12CrNi2Y alloy steel by direct laser deposition, *J. Mater. Sci. Technol.* 35 (2019) 395–402. <https://doi.org/10.1016/j.jmst.2018.10.024>.
- [46] K.M. Bertsch, G. Meric de Bellefon, B. Kuehl, D.J. Thoma, Origin of dislocation structures in an additively manufactured austenitic stainless steel 316L, *Acta Mater.* 199 (2020) 19–33. <https://doi.org/10.1016/j.actamat.2020.07.063>.
- [47] Z. Zhang, Z. Liu, D. Wu, Prediction of melt pool temperature in directed energy deposition using machine learning, *Addit. Manuf.* 37 (2021) 101692. <https://doi.org/10.1016/j.addma.2020.101692>.
- [48] T.Q.D. Pham, T.V. Hoang, X. Van Tran, Q.T. Pham, S. Fetni, L. Duchêne, H.S. Tran, A.-M. Habraken, Fast and accurate prediction of temperature evolutions in additive manufacturing process using deep learning, *J. Intell. Manuf.* (2022). <https://doi.org/10.1007/s10845-021-01896-8>.
- [49] T.Q.D. Pham, T.V. Hoang, X.V. Tran, S. Fetni, L. Duchêne, H.S. Tran, A.M. Habraken, Characterization, propagation, and sensitivity analysis of uncertainties in the directed energy deposition process using a deep learning-based surrogate model, *Probabilistic Eng. Mech.* 69 (2022) 103297. <https://doi.org/10.1016/j.probengmech.2022.103297>.
- [50] S. Cescotto, R. Charlier, Frictional contact finite elements based on mixed variational principles, *Int. J. Numer. Methods Eng.* 36 (1993) 1681–1701. <https://doi.org/10.1002/nme.1620361005>.
- [51] A.M. Habraken, S. Cescotto, Contact between deformable solids: The fully coupled approach, *Math. Comput. Model.* 28 (1998) 153–169. [https://doi.org/10.1016/S0895-7177\(98\)00115-0](https://doi.org/10.1016/S0895-7177(98)00115-0).

- [52] S. Yuan, L. Duchêne, C. Keller, E. Hug, C. Folton, E. Betaieb, O. Milis, A.-M. Habraken, Mechanical response of nickel multigrains for shear and tensile conditions at room temperature and 573 K, *Mater. Sci. Eng. A.* 809 (2021) 140987. <https://doi.org/10.1016/j.msea.2021.140987>.
- [53] S. Yuan, L. Duchêne, C. Keller, E. Hug, A.-M. Habraken, Tunable surface boundary conditions in strain gradient crystal plasticity model, *Mech. Mater.* 145 (2020) 103393. <https://doi.org/10.1016/j.mechmat.2020.103393>.
- [54] MSM & GEG (ULiege), Lagamine software, Univ. Liege. (2022). <http://www.lagamine.uliege.be/dokuwiki/doku.php> (accessed April 12, 2022).
- [55] S. Fetni, T.M. Enrici, T. Niccolini, H.S. Tran, O. Dedry, L. Duchêne, A. Mertens, A.M. Habraken, Thermal model for the directed energy deposition of composite coatings of 316L stainless steel enriched with tungsten carbides, *Mater. Des.* 204 (2021) 109661. <https://doi.org/10.1016/j.matdes.2021.109661>.
- [56] B.A. Khamidullin, I.V. Tsvil'skiy, A.I. Gorunov, A.K. Gilmutdinov, Modeling of the effect of powder parameters on laser cladding using coaxial nozzle, *Surf. Coatings Technol.* 364 (2019) 430–443. <https://doi.org/10.1016/j.surfcoat.2018.12.002>.
- [57] H. Yin, L. Wang, S.D. Felicelli, Comparison of two-dimensional and three-dimensional thermal models of the LENS® process, *J. Heat Transfer.* 130 (2008) 1–7. <https://doi.org/10.1115/1.2953236>.
- [58] H. Morch, L. Duchêne, R. Harzallah, V. Tuninetti, A.M. Habraken, Efficient temperature dependence of parameters for thermo-mechanical finite element modeling of alloy 230, *Eur. J. Mech. - A/Solids.* 85 (2021) 104116. <https://doi.org/10.1016/j.euromechsol.2020.104116>.
- [59] S. Qu, Y. Gong, Effect of heat treatment on microstructure and mechanical characteristics of 316L stainless steel parts fabricated by hybrid additive and subtractive process, *Int. J. Adv. Manuf. Technol.* 117 (2021) 3465–3475. <https://doi.org/10.1007/s00170-021-07786-w>.

Chapter 5 – Conclusions and Perspectives

Conclusions

This PhD thesis explores the topic of metal additive manufacturing, specifically focusing on the DED process of complex high speed steel alloys. This research represents the fruit of extensive investigations, both in terms of modeling efforts, and of experimentation, all aimed at shedding light on the intricate interplay of variables that define the DED process and its profound impact on microstructure and material properties.

Chapter 2 served as a foundational pillar, where we initially developed a 2D thermal model to gain insights into the thermal history of a 36-layer bulk deposit of M4 HSS. This model provided us with valuable glimpses into the intricate thermal dynamics within the manufacturing process. Moreover, it allowed us to calibrate and validate the model by carefully measuring key thermal histories and melt pool sizes, enhancing our understanding of the process.

Chapter 3 marked a significant progression, as we transitioned to a 3D thermomechanical model. However, this transition was not without its challenges. The thermophysical properties we measured during the manufacturing process turned out to be significantly different from those reported in the literature based on cast or forged samples. Also, a rigorous compression test campaign was conducted to elucidate the stress-strain behavior of M4 across a range of temperatures and strain rates.

The culmination of our research in Chapter 4 underscored the crucial role played by the thermal history in dictating the microstructure. We recognized that a constant laser power strategy often resulted in a non-uniform microstructure throughout the material depth. As a response, we embarked on an investigation into a variable laser power strategy aimed at achieving specific, desired microstructures at varying depths within the bulk sample. Our findings emphasized the direct correlation between melt pool size and the number of remelting events, ultimately influencing the resulting microstructure. To optimize laser power for precise control over melt pool size, we harnessed the Newton-Raphson iterative method.

In our quest to comprehensively evaluate the mechanical properties, we employed a combination of microhardness and nanoindentation techniques. Microhardness assessments underscored the benefits of the optimized variable laser power strategy, revealing enhanced homogeneity in hardness throughout the material depth. Meanwhile, nanoindentation results offered intriguing insights warranting further investigation and refined simulations, particularly concerning thermal history across the melt pool thickness.

The journey presented in this thesis reflects not only the progress and achievements but also the challenges and complexities inherent in the field of metal additive manufacturing, especially within the DED process. It underscores the crucial importance of a holistic understanding of thermal dynamics, microstructure evolution, and material properties. This research has provided valuable contributions to the knowledge base and opens doors to

further exploration and advancements in the fascinating world of additive manufacturing. We anticipate that the knowledge and insights gained herein will serve as a stepping stone for future innovations and breakthroughs in the ever-evolving landscape of metal additive manufacturing.

Perspectives

The research conducted in this thesis has contributed to a deeper understanding of the DED process, particularly in its application to HSS. However, as with any comprehensive study, this exploration has also uncovered areas that are ripe for further investigation. The nature of scientific inquiry is such that answering one set of questions often leads to the emergence of new, sometimes more complex questions. In this spirit, the following is a non-exhaustive list of topics that promise to enrich our knowledge and understanding of the DED process and its implications for HSS. These topics not only represent the next logical steps in our ongoing quest for understanding but also open doors to new possibilities and advancements in this exciting area of research.

Advanced Material Characterization: Future research can investigate in depth the characterization of materials used in DED processes. Investigate a broader range of thermophysical properties under varying conditions to build a more comprehensive database. This can include properties like thermal conductivity, density, and specific heat capacity.

Multi-Physics Modeling: Expand the modeling efforts to encompass multi-physics simulations. Incorporate not only thermal and mechanical aspects but also fluid dynamics and phase changes within the DED process. This can lead to more accurate predictive models.

In Situ Monitoring: Develop in situ monitoring techniques to observe the manufacturing process in real-time. Implement advanced sensors and imaging technologies to capture thermal histories, microstructure evolution, and defects as they occur. This real-time feedback can enable process control and optimization.

Machine Learning Integration: Explore the integration of machine learning algorithms to optimize process parameters dynamically. Utilize data collected during the manufacturing process to make real-time adjustments for achieving desired microstructures and properties.

Advanced Cooling Strategies: Investigate innovative cooling strategies to control the thermal gradients and solidification rates. Develop strategies such as directed energy cooling or local heat treatment to tailor microstructures with precision.

Microstructure-Property Relationships: Deepen the understanding of the relationship between microstructure and mechanical properties. Conduct extensive mechanical testing under various conditions to establish comprehensive databases linking microstructural features to material behavior.

Hybrid Manufacturing: Explore hybrid manufacturing techniques that combine DED with other additive or subtractive processes. Investigate how such hybrid approaches can enhance material properties, accuracy, and production efficiency.

Process Optimization Algorithms: Develop advanced optimization algorithms to automatically determine optimal process parameters based on desired material properties and microstructures. Consider genetic algorithms, neural networks, or other optimization techniques.

Industrial Applications: Extend research into practical industrial applications of DED. Collaborate with industry partners to implement findings in real-world manufacturing scenarios, ensuring the scalability and feasibility of proposed solutions.

Standardization and Quality Control: Contribute to the establishment of standardized procedures and quality control measures for DED processes. Work towards ensuring consistency, reliability, and repeatability in metal additive manufacturing.

Simulation Software Development: Collaborate with software developers to create user-friendly simulation tools tailored for DED processes. These tools can assist engineers and manufacturers in optimizing their designs and processes

Annex

Compression Test report

Compression tests were carried out on high speed steel (HSS) grade M4 samples at different temperatures and different strain rates. The tests were performed in a Schenck 400 kN machine (Figure 25a) and a quad elliptical radiant furnace 4x2000 W was used for high-temperature tests. The compression samples were cut using a wire electro-discharge machine from a part of a as-built bulk deposit (Figure 25b) produced by laser cladding for the RECYCLAD project (Sample P136, process parameters are: Laser power of 1160 W; nozzle speed of 462 mm/min and powder flow of 86 mg/s). The compression sample dimensions were 8 mm in diameter and 10 mm in height.



a)



b)

Figure 25 – a) Schenck 400 kN machine; b) Deposit from where the samples were removed.

Samples were tested at room temperature as well as high temperature (300, 500, 950 °C) at different strain rates (2×10^{-3} , 10×10^{-3} , and $50 \times 10^{-3} \text{ s}^{-1}$). For each combination of temperatures and strain rate conditions, a minimum of three samples were tested.

Correction procedure

As validated in V. Tuninetti Ph.D. thesis ([1]) and already applied in I. Neira's Ph.D. thesis ([2]) for a similar grade material, a methodology to reach a constant strain rate was implemented.

The displacement measured by the press electronic system is the global displacement that accounts for the machine and the sample displacement. For each combination of conditions, a compression test was carried out without a sample, where the tools were pressed against each other to obtain the machine rigidity. Later, the recorded data was converted to machine flexibility. The obtained set of points was interpolated by a sixth order polynomial that showed an error $R^2 > 0.98$ for the worst fitting. An example of room temperature and strain rate of $50 \times 10^{-3} \text{ s}^{-1}$ is presented in Figure 26.

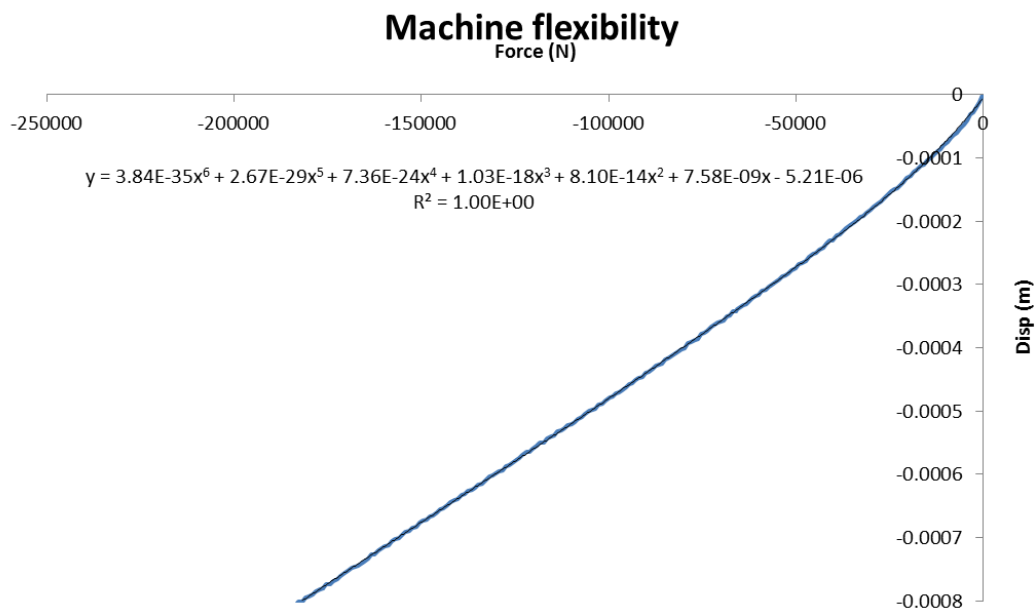


Figure 26 – Machine flexibility at room temperature for a strain rate of $50E-3 \text{ s}^{-1}$

Later the machine displacement was removed from the global displacement to obtain the sample displacement. An example of this application for room temperature and strain rate of $50E-3 \text{ s}^{-1}$ is presented in Figure 27.

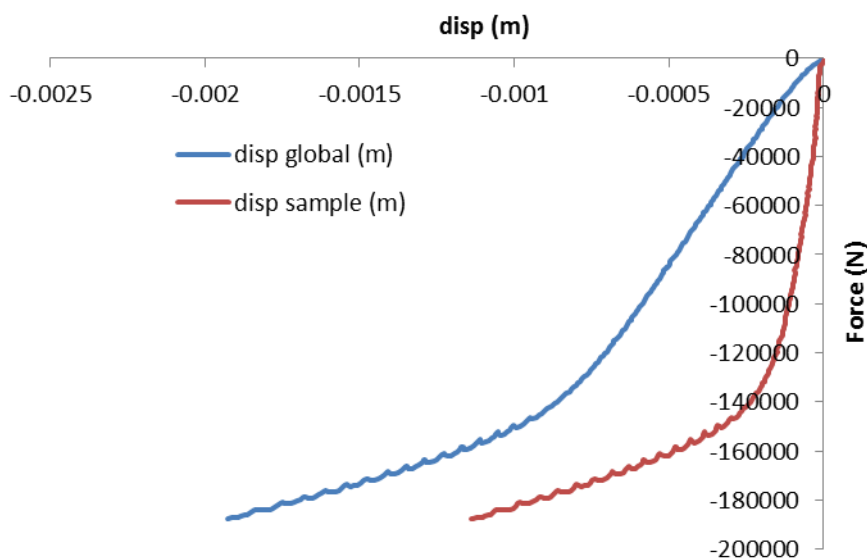


Figure 27 – Subtraction of the machine displacement over the global displacement at room temperature and $50E-3 \text{ s}^{-1}$

Finally, logarithmic strain based on the sample displacement was computed.

The calculated real stress took into consideration the barrelling effect through a deduced formula developed by Orowan (V:\Projets\Lingopti et suite\LINGOPTI\Rapports\rapport intermédiaire n°7) - Essais de compression à chaud); meaning that the stress calculated takes in consideration the real section of the sample. In Eq.1, σ is the real stress, F is the force and r_{real} is the value of radius considering barrelling and d is the displacement. For Eq.2, r_H is the value of radius assuming no barrelling (just normal volume conservation $\rightarrow v=0.5$), d_{final} is the last measured displacement, $r_{real,final}$ is the last radius computed assuming barrelling and $r_{H,final}$ is the last radius assuming volume conservation. Finally, for Eq.3 $r_{initial}$, $h_{initial}$ and h_{final} are, respectively, the initial radius, initial height, and final height of the sample.

$$\sigma = \frac{F}{\pi \cdot r_{real}^2(d)} \quad \text{Eq.1}$$

$$r_{real}(d) = r_H(d) + \frac{d}{d_{final}} (r_{real,final} - r_{H,final}) \quad \text{Eq.2}$$

$$r_H = r_{initial} \sqrt{\frac{h_{initial}}{h_{final}}} \quad \text{Eq.3}$$

For each test, the stress-strain curve was generated (Figure 28a) then an average curve was calculated from the valid samples. As an example, it is shown in Figure 28a the applied process, consisting in removing any outlier, which in this case was sample 38, and after the average curve was calculated with the error bars (Figure 28b).

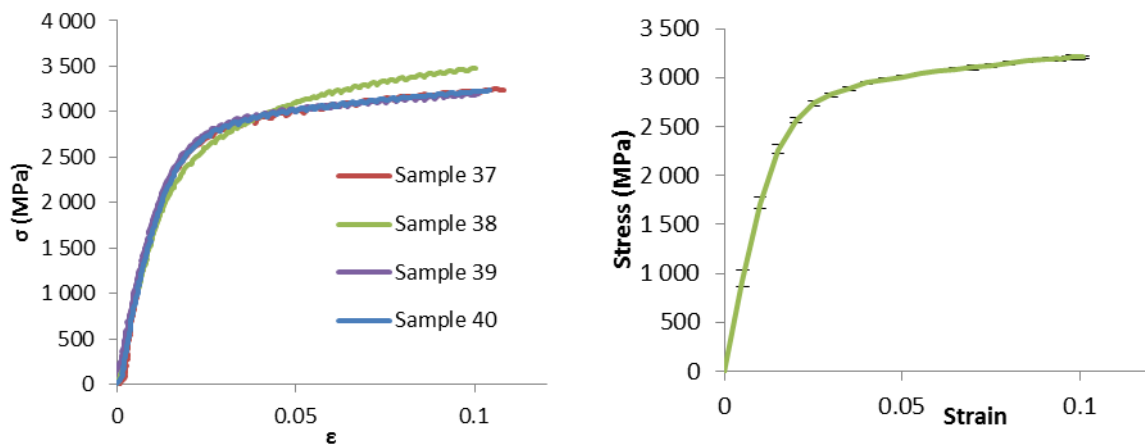


Figure 28 – a) True stress true strain curves of all the tested samples at room temperature and a strain rate of $50 \times 10^{-3} \text{ s}^{-1}$; b) average cure with error bars from the samples 37, 39, and 40.

Finally, the elastic part was corrected by replacing the computed one with the value measured by Grindosonic (measurements done by the MMS team) (V:\Projets\PDR Lasercladding\Reports) for the room temperature case, with a value of 216.3 GPa. At high

temperatures, the value measured by I. Neira for her Ph.D. thesis on high chromium steel was considered (Table 2).

Table 2 – Young moduli value obtained by compression tests

Temperature (°C)	Samples Microstructure	E in compression test (GPa)
300	Annealed samples cooled (100%Au)	186.14±14.31
700		78.74±6.2
950		50.98±9.48
20	Martensite Quenched samples heated (100%Ma)	190.24±5.80
80		167.6±1.80
150		187.5±5.80

Discussion of the results

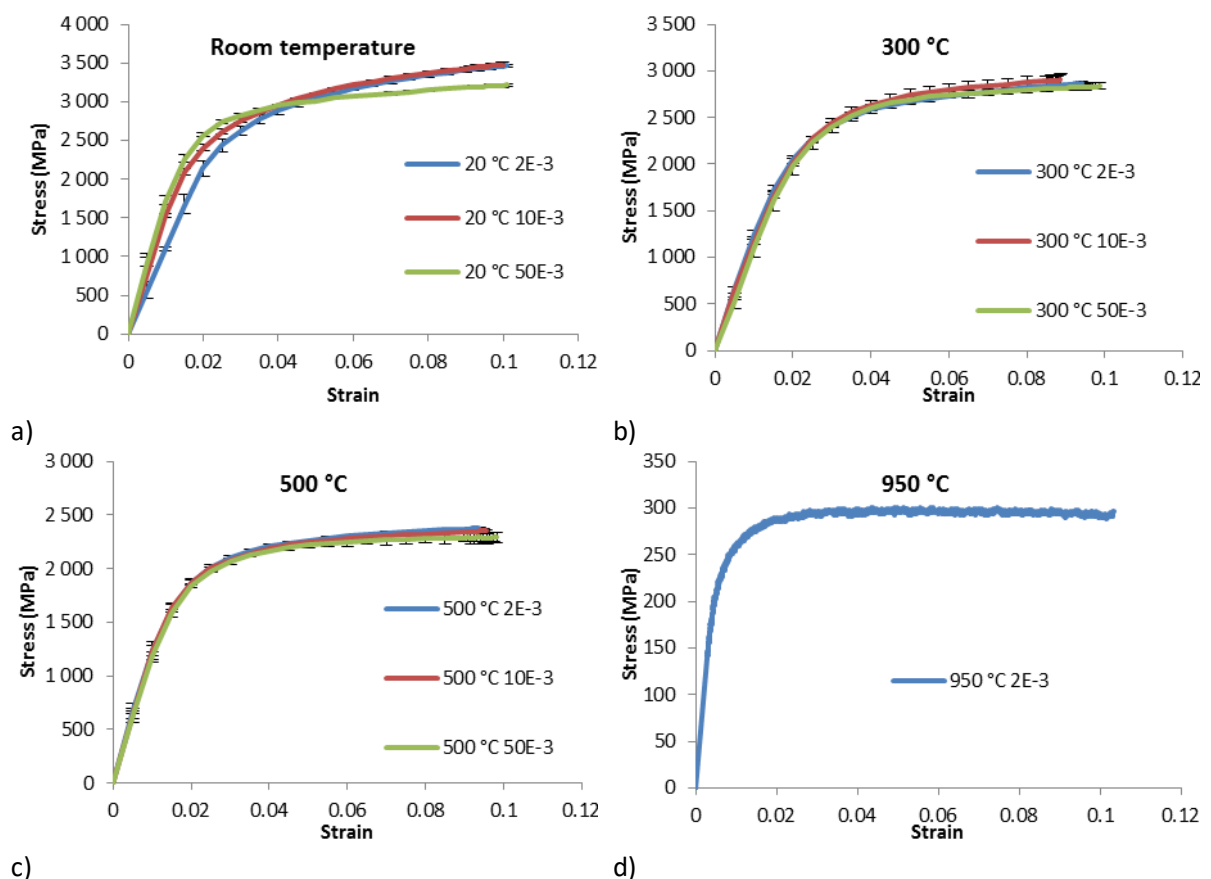


Figure 29 – Stress-strain curves at different temperatures and strain rates. a) room temperature; b) 300 °C; c) 500 °C; d) 950 °C.

As shown in Figure 29, the effect of strain rate, in the analysed range (2×10^{-3} to $50 \times 10^{-3} \text{ s}^{-1}$), is not very significant. Overall, it is shown that the higher the strain rate, the lower the hardening. This effect is more obvious at room temperature. The curves here depicted didn't have their elastic modulus adjusted from the values of Grindosonic and literature from I. Neira PhD thesis.

For the case at 950 °C just one sample was successfully tested. The problem is that at 950 °C, the furnace started to lose performance and could barely reach the targeted temperature, for the next trials, it couldn't maintain the 950 °C. Also, the compression tools (made of tungsten carbide) started to decarburize, deteriorating their mechanical properties. So, only one sample is available and it was used as representative behavior at 950 °C. When compared with the stress-strain curve at 950 °C from Neira Ph.D. a close agreement is reached.

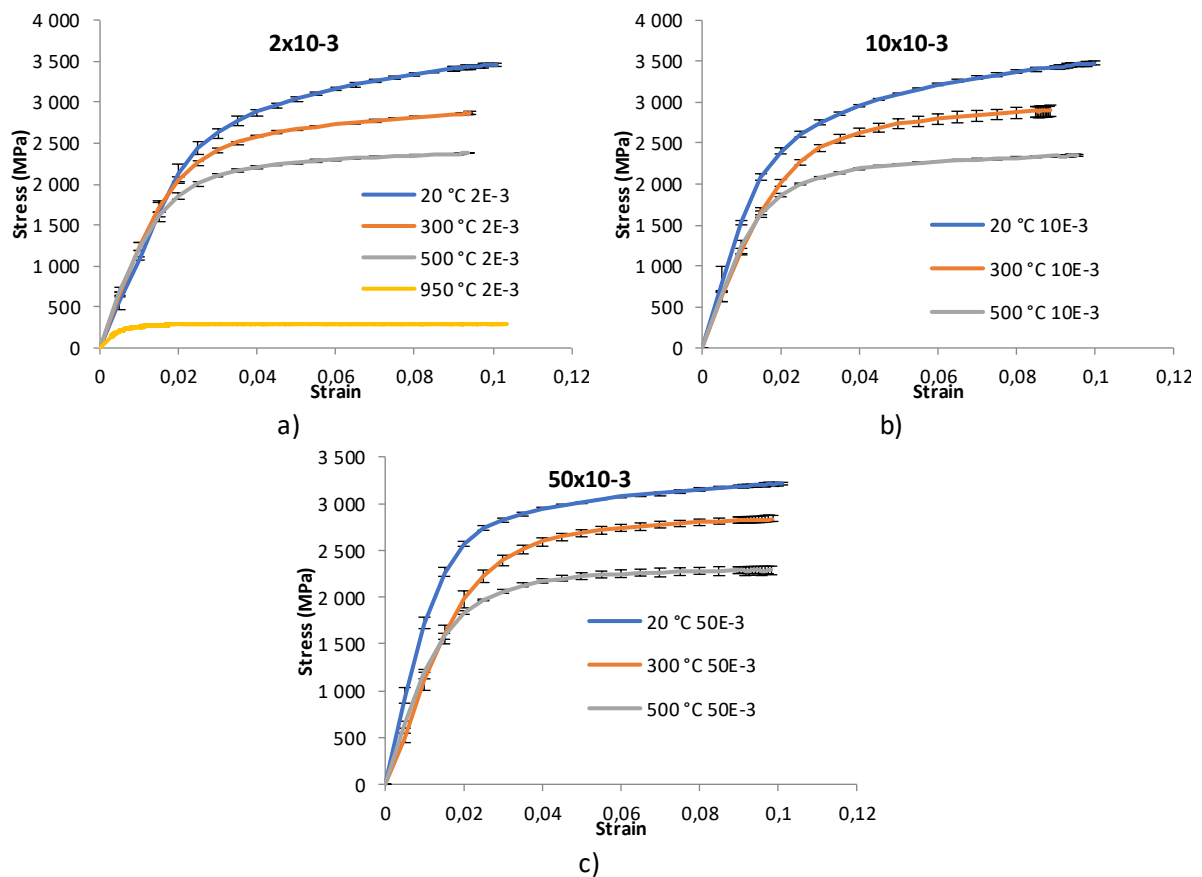


Figure 30- Stress-strain curves at different strain rates. a) 2×10^{-3} ; b) 10×10^{-3} ; c) 50×10^{-3} .

Fitting for Numerical model

The elastoplastic law currently used allows the input of several points to define the plastic strain range behavior. A systematic fitting was done for the plastic part in the stress-strain curves obtained (Figure 31). Also, Table 3 gives the value of the tangent moduli for plasticity, and Table 4 the values of Young moduli and yield stress at different temperatures.

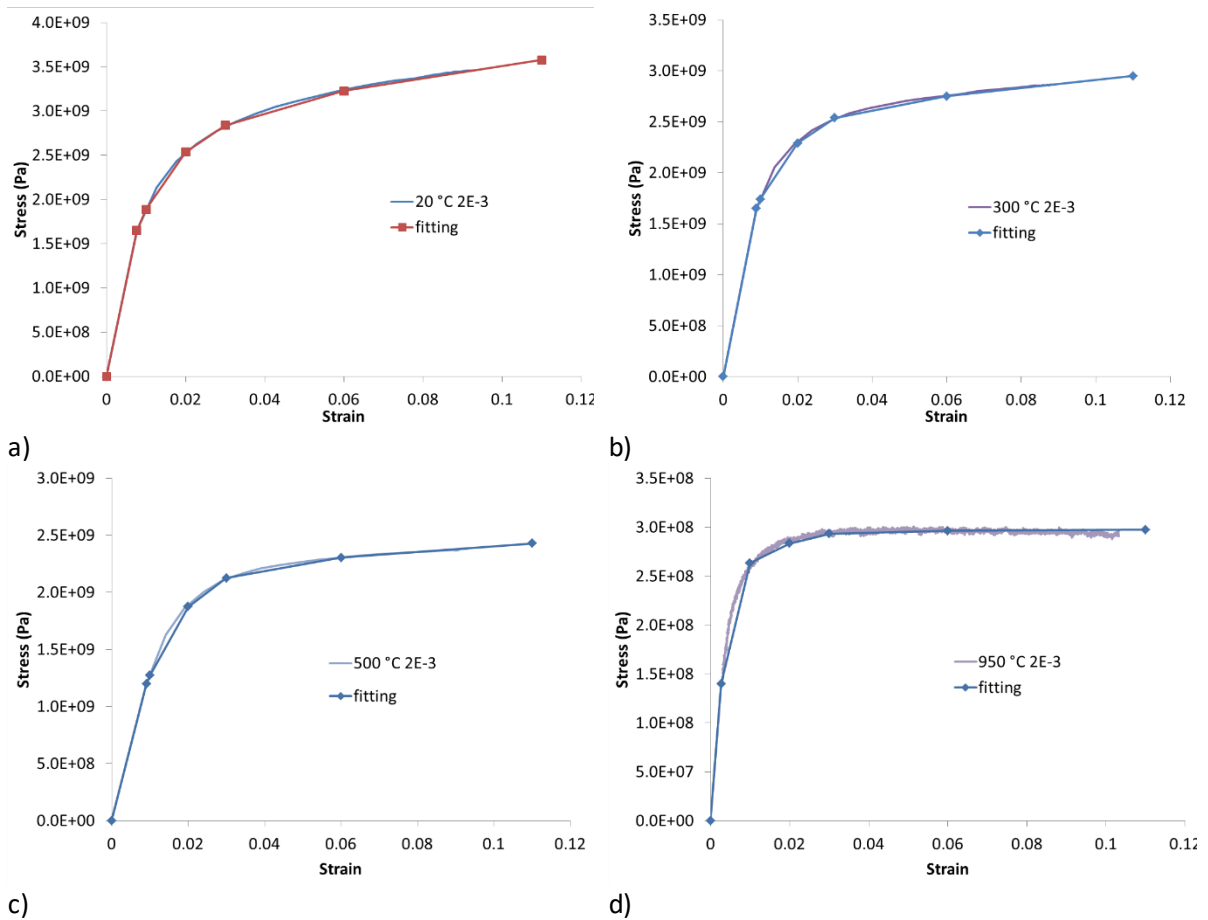


Figure 31 – Fitting of the stress strain curves at a) room temperature; b) 300 °C; c) 500 °C; d) 950 °C.

Table 3 – Tangent moduli in plasticity (in Pa) at different temperatures.

	Strain levels				
	0.01	0.02	0.03	0.06	0.11
20 °C	1.00E+11	6.50E+10	3.00E+10	1.30E+10	7.00E+09
300 °C	8.00E+10	5.50E+10	2.50E+10	7.00E+09	4.00E+09
500 °C	8.00E+10	6.00E+10	2.50E+10	6.00E+09	2.50E+09
950 °C	1.70E+10	2.00E+09	1.00E+09	1.00E+08	5.00E+07

Table 4 – Yield stress and Young moduli at different temperatures.

	Yield stress (Pa)	Young moduli (Pa)
20 °C	1.65E+09	2.16E+11
300 °C	1.65E+09	1.86E+11
500 °C	1.20E+09	1.32E+11
950 °C	1.4E+08	5.10E+10

References

- [1] V. Tuninetti, "EXPERIMENTAL AND NUMERICAL STUDY OF THE QUASI-STATIC BEHAVIOR OF Ti-6Al-4V," *Ph.D. Thesis*, 2014.

- [2] I. N. Torres, "Modelling of the cooling and thermal treatment of bimetallic rolling mill rolls," *Ph.D. Thesis*, 2015.

